# ELECTROSTATIC FIELDS IN HYBRID HETEROJUNCTIONS:

## FIELD-EFFECT TRANSISTOR, TOPOLOGICAL INSULATOR, & THERMOELECTRONIC APPLICATION

by

Robert Matthew Ireland

A dissertation submitted to Johns Hopkins University in conformity with the requirements for the degree of Doctor of Philosophy

Baltimore, Maryland

March, 2016

# Abstract

Organic semiconductors (OSC) are still surging in popularity for sustainable electronic devices, especially since they can perform as well as amorphous and polycrystalline silicon materials. Although OSCs have processing advantages that give rise to novel opportunities compared to inorganic semiconductors (ISCs), devices usually require inorganic materials for highly conductive connections or other functionality. Significantly, OSCs can be used to tune or modify the behavior of inorganic semiconductors (ISCs) by exploiting the junction between two semiconductors (a heterojunction).

The possible creation of stable interfaces between ISCs and OSCs provides a practically limitless range of functionalities. Broadly, my goal is to study interfaces between OSCs and ISCs (hybrid heterojunctions) by testing devices of different configurations and altering the internal fields systematically, as well as with the aid of electron- and force-microscopy, and photoelectron spectroscopy. This thesis contains three major sections based around nascent, relevant applications: field-effect transistors, topological insulators, and thermoelectrics.

First I study the effects of combining tellurium thin-films with OSC layers in field-effect transistors, where the organic acts both as a substrate modification layer and electrostatic gate. Secondly, I use electron withdrawing OSCs as gating materials for modifying $Bi_2Se_3$ in order to realize fundamental topological insulator behavior. Thirdly, I develop polymer-particle composites, including doping of the polymers and stabilization of inorganic particles with an electronic density of states that supports good thermoelectric behavior. We show that OSCs can undeniably be used to significantly

modify properties of ISCs, namely tellurium, bismuth selenide, and organometallic compounds.

I will first discuss the interfacial fields intrinsic to each heterojunction or device structure. Then I implement an additional electrostatic gate as part of the overall structure in order to further interrogate and modify device behavior. The additional gate is provided by introducing a polymer dielectric layer and embedding charges in this dielectric by corona charging method. This work will lead to improved design of hybrid devices because we can obtain benefits of both materials to achieve new performance records ($ZT>0.1$ in thermoelectric polymer-particle composites) and capabilities (topological insulator behavior), and also use heterojunctions as a basis to study and design materials or systems (tellurium/OSC transistors).

## Dedication

Dedicated to my family & friends.

## Acknowledgement

Infinite thanks to all my mentors, advisors, and colleagues.

# Table of Contents

**Abstract** …….…....ii

**Dedication** …….…....iv

**Acknowledgement** …….…...iv

**Table of Contents** …….……v

**List of Tables** …...……....vii

**List of Figures** …...…….…viii

## Chapters:

**I. Introduction**

Organic-Inorganic Semiconductor Hybrid Materials ..…….……1

References …….…….……..…7

**II. Field-Effect Transistor Application**

Introduction ……...……...…....12

References …….…….…..…..…24

Interfacial Fields in P-type Tellurium-Organic Hybrids …….….26

References …….…….....…40

Self-Assembled Monolayers on Gate Dielectric ……..…41

References …….……..……..…47

Picosecond Laser Direct-Write Patterning of FET Arrays ……..…49

References …….…….……...53

Electrostatic Gating by Corona Charging of Electret Polymer ……....…54

References …….…….....…61

**III. Topological Insulator Application**

Introduction ……..62

References ……64

Interfacial Fields in N-type Bismuth Selenide-Organic Hybrids ……..…68

References ……..…….77

Electrostatic Gating by Corona Charging of Electret Polymer ……..……..78

References ……..……..…85

**IV. Thermoelectric Application**

Introduction ……..……68

References ……94

Interfacial Fields in Polymer-Particle Composites ……..…96

N-type Composite Hybrids ……...…96

P-type Composite Hybrids ……..…109

References ……..……...…127

Electrostatic Gating by Corona Charging of Electret Polymer ……..…128

References ……..……..…142

**V. Conclusion**

Summary & Future Work ……..……..…145

References ……..……..…148

## Appendix:

**Bibliography** ……..…….149

**Curriculum Vitae** ……..….151

# List of Tables

**Table 1.** FET Parameters and Performance under Static or Pulsed Bias, and Heated Substrates. (page 23)

**Table 2.** Thermoelectric Performance of Te, 6PTTP6, and Te/OSC Bilayers. (page 40)

**Table 3.** Hybrid OFET Parameters and Performance with Charged Polystyrene. (page 59)

**Table 4.** 60wt% Co(acac)3 in PQT12 – TE Parameters as a Function of Solution Concentration and Volume of Solution Drop-Cast per Substrate Area, utilizing Chlorobenzene. (page 118)

**Table 5.** Comparing TE Parameters of PQT12 Composites – 10 mg/ml solutions, 0.18 ml/cm$^2$. (page 126)

# List of Figures

**Figure 1.** General schematic for trilayer OFET structure; three thin-films deposited onto 100 nm thick bare silicon dioxide are represented as materials number 1 and 2; material 1 is generally the OSC and material 2 is Te, and each semiconductor is nominally deposited to 10 nm. Gold source and drain electrodes were deposited (50 nm thick) with four different W/L ratios of 80, 53, 40, and 32. (page 17)

**Figure 2.** Chemical structures for a) Te unit cell (a=0.445 nm, c=0.591 nm) b) 5,5'-bis(4-hexylphenyl)-2,2'bithiophene (6PTTP6) c) pentacene d) N,N'-bis(3-perfluorooctylpropyl) naphthalenetetracarboxylic diimide (8-3NTCDI) e) tetratetracontane f) N,N'-diphenyl-N,N'-bis(1-Naphthyl)-1,1'-biphenyl-4,4"-diamine (NPD) g) atactic polystyrene h) (3-aminopropyl)trimethoxysilane i) 1H,1H,2H,2H-perfluorooctyltriethoxysilane j) Disperse Red 19 with triethoxysilane groups (DR19). (page 17)

**Figure 3.** Capacitance of hybrid gate stacks using bare oxide for a) bare $SiO_2$, b) 6PTTP6/$SiO_2$, c) Te/6PTTP6/$SiO_2$, d) 6PTTP6/Te/6PTTP6/$SiO_2$. (page 21)

**Figure 4.** Output curves for a) tellurium, b) Te/6PTTP6 bilayer, and c) 6PTTP6/Te/6PTTP6 trilayer field-effect transistors. Bare $SiO_2$, substrates held at 55 °C during deposition. (page 22)

**Figure 5.** X-ray diffraction of tellurium films deposited onto a) glass, b) 6PTTP6 on glass, and tetratetracontane ($C_{44}H_{90}$) on glass. (page 23)

**Figure 6.** Scanning electron micrographs of Te morphology when deposited at 0.3 Å $s^{-1}$ onto various organic thin-films, including a) $SiO_2$, b) 6PTTP6, c) pentacene, d)

tetratetracontane ($C_{44}H_{90}$), e) SiO2 while substrate held at 55 ˚C, f) 6PTTP6 while substrate held at 55 ˚C, g) DR19 monolayer while substrate held at 55 ˚C, and h) NPD. (page 29)

**Figure 7.** a) SEM micrograph of Te deposited on $SiO_2$ at 3.0 Å $s^{-1}$. b) Te deposited on 6PTTP6/$SiO_2$ at 3.0 Å $s^{-1}$. c) Te deposited on pentacene/$SiO_2$ at 3.0 Å $s^{-1}$. d) Te deposited on $SiO_2$ at 10.0 Å $s^{-1}$. (page 30)

**Figure 8.** a-b) SEM micrograph of 4 nm Te on 8-3 NTCDI, located away from the source-drain electrodes c-d) 4 nm Te on 8-3 NTCDI, located inbetween source-drain electrodes. (page 33)

**Figure 9.** a-b) $I_D$ vs. $V_D$ plot for 8-3NTCDI/Te on $SiO_2$ at room temperature with top contact Te electrodes. W/L is 80. b) $I_D^{1/2}$ vs. $V_G$ plot. (page 35)

**Figure 10.** 2D SKPM surface potential scans across interfaces of OSC and Te deposited on top of the OSC for 6PTTP6 vs. Te/6PTTP6 (top, from left to right), and pentacene vs. Te/pentacene (bottom, from left to right). (page 37)

**Figure 11.** Energy band diagram of isolated intrinsic materials. (page 38)

**Figure 12.** Plots used to calculate resistance (left) and Seebeck (right) for typical Te on 6PTTP6 sample. (page 39)

**Figure 13.** X-ray Photoelectron Spectra of substrates modified with SAMs. a) Carbon 1s spectra. APTS samples show the peak at 284.5, corresponding to the $CH_2$ bond. FOTS samples show a peak at 291 eV with shoulder at 293 eV, corresponding to $CF_2$ and $CF_3$ bonds. b) Nitrogen 1s spectra. APTS shows peak for $NH_2$ bond and DR19 with some $NO_2$ bonds. (page 44)

**Figure 14.** a) SEM micrograph of Te morphology on APTS/$SiO_2$ substrates b) Te/6PTTP6 on APTS/$SiO_2$ substrates c) Te on FOTS/$SiO_2$ d) Te/6PTTP6 on FOTS/$SiO_2$ e) Te on DR19/$SiO_2$ substrates and f) Te/6PTTP6 on DR19/$SiO_2$ substrates, all done at room temperature. (page 45)

**Figure 15.** a) $I_D$ vs. $V_D$ (static $V_G$) plot for Te deposited on DR19/$SiO_2$ at room temperature with top contact Au electrodes; W/L is 80 b) $I_D^{1/2}$ vs. $V_G$ plot. (page 47)

**Figure 16.** a) SEM micrograph of Te morphology on uncharged polystyrene at room temperature b) Te on polystyrene charged +50 V c) Te/6PTTP6 on uncharged polystyrene d) Te/6PTTP6 on polystyrene charged +50 V. (page 55)

**Figure 17.** 6PTTP6 morphology on $SiO_2$/polystyrene dielectric. a) AFM image of 6PTTP6 morphology on uncharged polystyrene dielectric. b) 6PTTP6 morphology on polystyrene charged +50 V. (page 56)

**Figure 18.** Schematic charge distributions for the two Te/OSC bilayers, and for Te/6PTTP6 on polystyrene charged with positive 50 V, before application of $V_g$. (page 57)

**Figure 19.** $I_d$ vs. $V_d$ plot for a) 6PTTP6 on PS/$SiO_2$ and b) PS+50/$SiO_2$. c) Te on PS/$SiO_2$ and d) PS+50/$SiO_2$. e) Te/6PTTP6 on PS/$SiO_2$ and f) PS+50/$SiO_2$. (page 58)

**Figure 20.** a) $I_D$ vs. $V_D$ plot for tellurium on pentacene/$SiO_2$ (collapse at 20$V_G$). b) $I_D$ vs. $V_D$ plot for Te/6PTTP6 on PS+50/$SiO_2$ (collapse at -20$V_G$). W/L is 80. (page 61)

**Figure 21.** Real conductance plots for $Bi_2Se_3$ covered with F4TCNQ (left) and tetracene (right). (page 69)

**Figure 22.** (a) Real and (b) imaginary conductance for bare 16QL $Bi_2Se_3$ (sample 1) at day 1, with 50 nm F4TCNQ doping layer at day 2 and with F4TCNQ at day 120 at 5 K.

(c) Real and (d) imaginary conductance for bare 16QL $Bi_2Se_3$ (sample 2) at day 1, with 50 nm $Co(acac)_3$ doping layer at day 2 and with $Co(acac)_3$ at day 120 at 5 K. (e) Real and (f) imaginary conductance for bare 16QL $Bi_2Se_3$ (sample 3) at day 1, with 50 nm $MoO_3$ doping layer at day 2 at 5 K. (page 71)

**Figure 23.** Hall resistance for 16QL bare $Bi_2Se_3$, with 50 nm F4TCNQ, with 50 nm $Co(acac)_3$ and with 50 nm $MoO_3$ at 5 K. (page 73)

**Figure 24.** (a) Drude spectral weight (b) Drude scattering rate (c) carrier density and (d) mobility as a function of time for 16QL bare $Bi_2Se_3$, with 50 nm F4TCNQ, with 50 nm $Co(acac)_3$ and with 50 nm $MoO_3$ at 5 K. The data points marked with open squares are from DC transport. (e) Energy level diagram indicates the Fermi level of TI/OSC devices have chemical potential 80-100 meV below conduction band minimum. (page 74)

**Figure 25**. Energy level diagram with energy band edges for $Bi_2Se_3$, ZnO, 7,7,8,8-tetracyanoquinodimethane (TCNQ), F4TCNQ, $MoO_3$, and redox potentials of $Co(acac)_3$. Blue and red lines stand for highest occupied molecular orbital (HOMO) and lowest unoccupied molecular orbital (LUMO) bands. (page 77)

**Figure 26.** Photographs (top, left to right) of a sample and copper tape on the copper stage, the grid screen in place, and the external connection to the needle corona source. Schematics (bottom) of the corona charging setup with and without copper tape grounding of the $Bi_2Se_3$ layer. (page 81)

**Figure 27.** Surface charge measured as a result of corona charging for various times with -1500 V applied to the grid over spincoated polymer films (thickness of ~1 μm). PS, polystyrene. C60 and Cl refer to $C_{60}$-methyl and chloromethyl styrenes at 3% monomer fraction. None, C paste, and Cu Tape refer to connections between gold and the

grounded copper stage. 80 C refers to final surface voltages after heating the samples to 80 °C during the charging. (page 82)

**Figure 28.** Plots shows the resulting potential stored in Novec after a) charging at constant grid voltage as a function of time, b) charging for a fixed time (5 minutes) at incremental grid voltages, and c) charging at single high grid voltage and then monitoring the stability of stored charge as a function of time (samples left in air). (page 84)

**Figure 29.** Frequency-dependent conductance of $Bi_2Se_3$ affected by charging of overlying a) cross-linkable PS or b) Novec. (page 85)

**Figure 30**. Chemical structure of a) poly(PyDI-ethynylene)-5FPE, b) P(NDI2OD-T2), c) P3HT, and d) PQT12. (page 93)

**Figure 31** a) Chemical structure of poly(PyDI-ethynylene)-5FPE, P(NDI2OD-T2) (known as N2200), and tin(II) chloride. b) Thermal conductivity and heat capacity vs weight % $SnCl_2$ in P1 films. c) The Seebeck coefficient, electrical conductivity, and power factor are plotted versus concentration of initial tin(II) chloride precursor within PYDI-5FPE (left) and P(NDI2OD-T2) (right) polymer matrices. Values are the average of at least 10 samples. Error bars are standard deviations. (page 98)

**Figure 32.** Optical microscope images of 60wt% $SnCl_2$ (top) and 70wt% $SnCl_2$ (bottom) in PyDI-5FPE polymer, captured as microwires by drop-casting (left), clusters by drop-casting (middle), and submicron clusters by spin-casting (right). (page 101)

**Figure 33.** Optical micrographs of $SnCl_2$ microstrostructure captured in PyDI-5FPE polymer matrix by drop-casting from starting concentrations ranging 20-90 wt%, and of pure $SnCl_2$ drop-cast from solution on glass alone. Scale bars are all 100 μm. (page 102)

**Figure 34.** Elemental maps obtained by EDS using an SEM backscatter detector show the coverage of Sn, Cl, Si, O, and C atoms for 60wt% $SnCl_2$ in PYDI-5FPE polymer obtained by drop-casting. Bottom right is the original SEM image. (page 103)

**Figure 35.** Scanning Kelvin probe microscopy measurement of tin chloride microwire captured in PyDI-5FPE polymer, left is the height measurement and right is the surface potential, showing that the electronic states in the wire are more positive, or pushed away from the vacuum level, so electron depletion occurs in the inorganic at their interface, and electron accumulation in the polymer. (page 104)

**Figure 36.** Ultraviolet photoelectron spectra of leading edge of valence band for PYDI-5FPE polymer, tin(II) chloride, and polymer composite with 60wt% $SnCl_2$. (page 105)

**Figure 37.** XPS of 60 and 80 wt% tin(II) chloride blended in PYDI-5FPE polymer matrix, and for pure tin(II) chloride film. (page 106)

**Figure 38.** a) Chemical structures (top) and illustration for processing TE films on glass substrates with patterned gold electrodes (bottom), b) schematic for Seebeck measurement (top) and for four-probe resistance measurements (bottom). (page 110)

**Figure 39.** Optical microscope images of a) PQT12 blended with 10, 20, 40, 60, and 80 wt% cobalt(III) acetylacetonate, and of b) 60wt% $Co(acac)_3$ in PQT12 samples drop-cast using increasing amounts of solution volume per area when solution is diluted to 10mg/ml (top) or 5mg/ml (bottom). Scale bars are all 100 μm. (page 111)

**Figure 40.** XRD for pristine PQT12 (green), pure $Co(acac)_3$ (red), and 60wt% $Co(acac)_3$ in PQT12 (blue). (page 112)

**Figure 41.** SEM images of $Co(acac)_3$ composite surface (left) and EDS compositional maps of close-up on edge of $Co(acac)_3$ particle in PQT12. (page 113)

**Figure 42.** Profile images of composite surfaces were measured by laser optical microscopy for PQT12 loaded with 0wt%, 20wt%, 40wt%, and 60wt% $Co(acac)_3$ (from left to right). (page 113)

**Figure 43.** The results of S, σ, and PF plotted for PQT12 blended with $Co(acac)_3$ as a function of dopant concentration for randomly oriented particles (solutions diluted to10 mg/ml and drop-cast using 0.18 ml/cm$^2$). Results of pure $Co(acac)_3$ are also shown (having similar results for thin-films prepared by drop-casting under vibration or by thermal evaporation). The star represents PF of 50wt% $Co(acac)_3$ samples with additional 10wt% F4TCNQ. The = and ≠ symbol represents 60wt% $Co(acac)_3$ samples with particles oriented either parallel or perpendicular to the gold electrodes, respectively. (page 114)

**Figure 44.** Height potential scan in 2D (top left) and 3D (top right), and the following surface potential scans also in 2D (bottom left) and 3D (bottom right). (page xx)

**Figure 45.** Energy levels of isolated materials. (page 116)

**Figure 46.** Optical micrographs of PQT12 composites containg 60wt% $Co(acac)_3$ processed via spin-casting, drop-casting of a solution aged more than one week, drop-cast utilizing dichlorobenzene, and drop-casting under vibration (from left to right). Scale bars are all 100 μm. (page 119)

**Figure 47.** Optical micrographs showing morphologies of pure $Co(acac)_3$ obtained by drop-casting with vibration using dilute solution (left), b) drop-casting with vibration using more concentrated solution (middle), and c) thermally evaporating $Co(acac)_3$ (right). Scale bars are all 100 μm. (page 121)

**Figure 48.** Illustrations for using an a) sloped gravitational gradient or b) a temperature gradient, and c) an image of a representative sample using both gradients constructively. (page 122)

**Figure 49.** Optical micrographs taken along the length of a representative samples using sloped gradient (top row) and temperature gradient (bottom row). (page 123)

**Figure 50.** Optical micrographs for particles oriented both perpendicular (left) and parallel (right) with the gold electrodes, and schematic of their orientation during testing (middle). (page 125)

**Figure 51**. a) Corona charging utilizing high voltage power supply (HV) and a grid voltage ($V_G$) and b) measurement of Seebeck coefficient; c) micrograph and laser microscope height profile of glass, PQT12, and Novec layers. (page 131)

**Figure 52.** Evolution of surface potential (stored charge) in Novec as a function of charging time at single applied grid voltage of positive or negative 500 V. Spin refers to samples with Novec spin-cast on top, and drop refers to samples with Novec drop-cast on top. (page 134)

**Figure 53.** Evolution of surface potential (stored charge) in Novec film deposited over PQT12 as a function of time (days) in air (petri dish) at room temperature (about 20 ˚C). The samples were charged once using grid voltage of 1000 V applied for 5 minutes, and then all surface potential measurements were made over time, and each point is an average of two devices. (page 135)

**Figure 54**. Seebeck coefficient (left y-axis, red squares), conductivity (right y-axis, blue diamonds), and power factor (right y-axis, green triangles) for composites comprising of

a) PQT12 capped with Novec and b) PQT12-$Co(acac)_3$ capped with Novec, all as functions of the stored surface potential in Novec (x-axis). (page 137)

**Figure 55.** Seebck coefficient (left y-axis, red squares), conductivity (right y-axis, blue diamonds), and power factor (right y-axis, green triangles) for composites comprising of PQT12 having 10 wt% F4TCNQ and then capped with Novec, all as functions of the stored surface potential in Novec (x-axis). (page 137)

**Figure 56.** a) Schematic image of side view for device structure using cross-linked polystyrene (XLPS) and b) evolution of surface potential (stored charge) in XLPS film without PQT12 deposited on top, as a function of time (days) in air (petri dish) at room temperature (about 20 ˚C). The samples were charged once using grid voltage of 1000 V applied for 5 minutes, and then all surface potential measurements were made over time, and each point is an average of two devices. Plots are shown for Seebeck coefficient (left y-axis, red squares), conductivity (right y-axis, blue diamonds), and power factor (right y-axis, green triangles) for bilayers comprising of c) PQT12 over XLPS and d) PQT12-$Co(acac)_3$ over XLPS, all as functions of the stored surface potential in Novec (x-axis) as an average of four devices each. Each surface potential value used for each data point is what was measured immediately after charging and before drop-casting PQT12, which may help to further stabilize the static charge in air. (page 141)

# CHAPTER 1

# Introduction

## Organic-Inorganic Semiconductor Hybrid Materials

This work focuses on interactions between low bandgap inorganic and organic semiconductors. Although inorganic semiconductors (ISCs) have outstanding performance characteristics due to their crystal structure and high carrier densities, organic materials demonstrate versatile processing capabilities, leading to rapid large-area manufacturing and greater tailorability at lower cost. These attributes make organic hybrids economically competitive alternatives to conventional crystalline and amorphous silicon devices. Not replacing silicon, advances in the field of organic semiconductors will allow completely new avenues of science and technology to be realized, such as disposable electronics, transparent and flexible displays, or associative memory devices.

In general, devices are not made completely with organic components, mainly because inorganic materials are still required for highly conductive contacts or connections. However, hybrid organic/inorganic heterostructures were investigated early in the development of organic semiconductors (OSCs). Heterostructures are junctions between semiconductors of dissimilar band gaps, which are found in applications as diverse as light-emitting diodes, lasing structures, and high electron-mobility transistors. The first organic-on-inorganic devices were demonstrated in 1980 at Bell Laboratories with the intention of characterizing electronic and dielectric behavior of undeveloped OSCs.[1] In the same vein, elemental tellurium was used as semiconductor material for field-effect transistors in order to study a polytetrafluoroethylene gate dielectric.[2]

Solution-deposited sodium beta-alumina was demonstrated as a transparent high-k gate dielectric in organic field-effect transistors.[3]

In addition to modifying or studying dielectric-metal interfaces, shifting energy levels at organic/organic[19-22] and organic/metal[22-24] junctions has been extensively investigated. The tuning of the energy-level match between OSCs and metal electrodes has been achieved using both metal oxides[43,44] and organic materials as interfacial layers.[36,45] At junctions between weakly-interacting OSCs, vacuum level alignment is expected. Between interfaces with greatly differing ionization energies or electron affinities, charge transfer tends to cause the formation of a "built-in" electrical potential (interface dipole) on the order of several tenths of an eV. Fermi energy pinning often results from alignment of OSC energy levels with the work functions of metals or inorganic semiconductors, specifically at their interfaces. The barrier height to charge transfer may be altered by surface modifications that shift the material work functions.

Wang and Yan extensively reviewed the theory of organic heterojunctions, which involves band alignment and Fermi pinning based on work function differences between semiconductors.[38] Compared to inorganic heterojunctions (IHJ), little is known about the electronic structure and charge transport of OSC junctions due to sensitive dependence on structure and overlap of molecular orbitals. While conventional IHJs are explained by depletion layers brought about by diffusion of majority carriers through a crystalline lattice, OSC charge transport is governed by many more factors. Unlike diffusion processes, electrons can transfer from CuPc (p-type) to preferred states in $F_{16}$CuPC (n-type), accumulating in regions of high concentration. The equilibrium established by their

chemical potential difference results in $F_{16}$CuPc OFETs which turn on at lower power because many traps to electrons have already been filled.

Although great progress has been made towards modeling and understanding of organic-organic and organic-metal interfaces, much less is certain about organic-inorganic heterojunctions (OIHJ). The behavior of OIHJs can be less predictable and requires detailed case-by-case investigation. A general model for these interfaces has not yet been accepted due to the wide variety of organic molecules and their ranges of impurity concentrations, carrier mobilities, dielectric constants, densities of states at particular energies, ionization energies, and electron affinities, and wide range in properties depending sensitively on processing. OIHJ systems are especially interesting however, as mentioned previously, because hybrids provide a test bed for exploring the physics of both OSCs and their composites with inorganic semiconductors. The combination of inorganic and organic semiconductors will allow for new models of studying and designing materials. Organic materials can be used to systematically tune or modify the behavior or properties of inorganic materials. Functionalizing or passivating the inorganic surface with molecules can also alter the electronic behavior by shifting chemical potentials. Surface charge doping (SCD) is a method for modifying one semiconductor by passivating or capping it with another semiconductor.[29-30] The method relies on charge separation and energy level alignment mechanisms at interfaces. SCD represents a valuable tool for the controlled and nondestructive doping of inorganic or organic semiconductors at their interfaces, especially when it cannot be easily achieved by the conventional implantation process with energetic ions. SCD can effectively

dedope semiconductors at the nanoscale at relatively low cost, thereby facilitating the development of hybrid electronics.

Significantly, heterojunctions can be implemented to create interfacial dipoles or space charge regions which can significantly affect device behavior. The creation of well-defined stable interfaces between inorganic electronic materials and organic electronic systems provides a new range of functionalities. Photovoltaic charge separation or current injection at electrodes can be promoted, transistor threshold voltages can be shifted, chemical potentials and carrier densities can be altered, density of states profiles for thermoelectric applications can be tuned, and memory effects can be obtained. High carrier mobility and transparency in the inorganics can be combined with photosensitivity at desired wavelengths from the organics. Organic/inorganic semiconductor junctions have been used for applications such as solar cells, [5,10-13], field-effect transistors, [14,-16 30,34,35] diodes, [17,18, 36] thermoelectrics,[37] and for investigating the fundamental properties of novel electronic materials.[38-42]

OIHJs benefit from increased electrical conductivity, lowered thermal conductivity, or absorption over a wider range of electromagnetic radiation. Recently, Wang et al. studied heterojunction effects between bilayers of evaporated OSCs and molybdenum trioxide.[38] They observed significant energy level bending and space charge regions of high conductivity near the junction, which is reasonable since previous studies report the reduced injection barrier for holes from $MoO_3$ into p-type OSCs.[4,43] Pal et al. reported the fabrication of pentacene-zinc oxide bilayers by solution processes, and then characterized the junction as diodes and as high mobility n-channel, ambipolar, and nonvolatile memory transistors.[3]

Jouane et al. use rf magnetron sputtering to grow ZnO films on top of organic polymers at room temperature for photovoltaic application.[11] Dietmueller et al. investigated the band alignment between undoped P3HT, an organic p-type polymer, and n-type 6H-SiC in order to explain their potential for hybrid heterojunction solar cells.[12] Ehrler et al. define the energy diagram for pentacene and PbS nanocrystals in bulk-heterojunction solar cells, where the band diagram built from experimental evidence explains the electro-optical behavior observed, namely singlet exciton fission.[13] Similarly, by constructing the energy diagrams from current-voltage measurements we can identify and explain the observed phenomena between OSC and tellurium thin films. Their large differences in carrier densities, charge transport, and band gap energies, lead to mobile charge transfer and a "built-in" electric potential at the junction. Significantly, energy band alignment causes a significant "spike" between the conduction band of tellurium and the HOMO of 6PTTP6, resulting in electrical behavior previously reserved for inorganic high electron mobility transistors (HEMTs), which are devices that typically require precise doping, outstanding purity, and exceptional lattice matching between crystalline materials.

Kevin See utilizes tellurium nanorods blended with a conductive organic polymer (PEDOT:PSS) to combine the electronic and thermal transport properties into an organic-inorganic bulk-heterojunction with record breaking thermoelectric figure of merit for solution-processed films.[46] The dispersion of Te nanostructures in an aqueous solution of PEDOT was obtained and cast to form composites with ZT of about 0.1 at room temperature.[46-48] Due to the S coefficient being positive and significantly higher than pristine polymer, it is thought that the holes were solely responsible for charge transport

and that the transport did not occur exclusively through the polymer. The use of Te nanostructures in thermoelectrics was suggested earlier, and the fundamental thermoelectric properties of elemental Te have appeared in literature extending decades back.[49,50] Polymer-assisted growth of particles *in situ* of thin film fabrication has been shown to improve interfacial interactions, including electronically driven interactions between polymer and as-grown particles. *In situ* growth of the metal-based particles within the polymer matrix is also expected to enhance the interactions between constituents and can lead to a charge-complex at the interface. One example is the interaction between Te nanowires grown in PEDOT.[47,48] Urban  suggest that carrier transport occurs predominantly through a more conductive volume of PEDOT that exists at the interface with tellurium nanocrystals, which may be due to good morphological structure accomplished by *in situ* fabrication.[51] Similarly, cadmium telluride nanocrystals were synthesized in P3HT without use of surfactants.[52]

Broadly, the aim of this thesis is to study interfaces between low bandgap OSCs and ISCs by testing devices of different configurations and altering the internal fields systematically, as well as with the aid of electron- and force-microscopy, and photoelectron spectroscopy. The dissertation contains three major sections based around nascent, relevant applications: field-effect transistors, topological insulators, and thermoelectronics. First I study the effects of combining tellurium thin-films with OSC layers in field-effect transistors, where the organic acts both as a substrate or electrode modification layer and electrostatic gate (Chapter 2). Secondly, I use electron withdrawing organic semiconductors as gating materials for modifying $Bi_2Se_3$ in order to allow topological insulator behavior to be observable and studied (Chapter 3). Thirdly, I

develop polymer-particle composites with intentionally designed interfaces (Chapter 4). This includes doping of the polymers, or stabilization of inorganic particles, with an electronic density of states that supports good thermoelectric behavior. We show that OSCs can undeniably be used to significantly modify properties of the ISCs, namely tellurium, bismuth selenide, and various organometallic compounds.

In each chapter I will first discuss the interfacial fields that are intrinsic to each heterojunction system or device structure. Then I will also implement an additional electrostatic gate as part of the overall device structure in order to further interrogate and modify the device behavior. The additional gate will be provided in each case by introducing a polymer dielectric layer and embedding charges in this dielectric by corona charging method. This work will lead to improved design of hybrid devices because we can obtain benefits of both materials to achieve new performance records (ZT>0.1 in thermoelectric polymer-particle composites), new capabilities (topological insulator behavior), and also use heterojunctions as a basis to study and design materials or systems (tellurium/OSC transistors). Ultimately we show that OSCs can undeniably be used to significantly modify properties of ISCs, namely tellurium, bismuth selenide, and organometallic compounds.

**References**

1. S. R. Forrest, M. L. Kaplan, P. H. Shmidt, W. L. Feldmann, E. Yanowski, *Appl. Phys. Letters.* **1982**, 41.

2. A. De Vos, B. Hindryckx, *IEEE.* **1980**, 127, 42-44.

3. B. N. Pal, B. M. Dhar, K. C. See, H. E. Katz, *Nature Mater.* **2010**, 8, 898-903.

4. C.W. Chu, S.H. Li, C.W. Chen, V. Shrotriya, Y. Yang, *Appl. Phys. Letters.* **2005**, 87, 193508.

5. M. T. Greiner, M. G. Helander, W.M. Tang, Z.B. Wang, J. Qui, Z.H. Lu, *Nature Mater.* **2012**, 11, 76-81.

6. J. Wang, H. Wang, J. Zhang, X. Yan, D. Yan, *J. Appl. Phys.* **2005**, 97, 026106.

7. X. Yan, J. Wang, H. Wang, H. Wang, D. Yan, *Appl. Phys. Lett.* **2006**, 89, 053510.

8. X. Yu, J. Yu, J. Zhou, J. Huang, Y. Jiang, *Appl. Phys.Lett.* **2011**, 99, 063306.

9. Y. Zhou, C. Fuentes-Hernandez, J. Shim, J. Meyer, A. J. Giordano, H. Li, P. Winget, T. Papadopoulos, H. Cheun, J. Kim, M. Fenoll, A. Dindar, W. Haske, E. Najafabadi, T. M. Khan, H. Sojoudi, S. Barlow, S. Graham, J. L. Bredas, S. R. Marder, A. Kahn, B. Kippelen, *Science.* **2012**, 336, 327-332.

10. B. O'Regan, M. Gratzel, *Nature.* **1991**, 353, 737-739.

11. Y. Jouane, S. Colis, G. Shmerber, P. Kern, A. Dinia, T. Heiser, Y.A. Chapuis, *J. Mater. Chem.* **2011**, 21, 1953-1958.

12. R. Dietmueller, H. Nesswetter, S. J. Schoell, I. D. Sharp, M. Stutzmann, *ACS Appl. Mater. Interf.* **2011**, 3, 4286-4291.

13. B. Ehrler, M. W. B. Wilson, A. Rao, R. H. Friend, N. C. Greenham, *Nano Lett.* **2012**, 12, 1053-1057.

14. C. R. Kagan, D. B. Mitzi, C. D. Dimitrakopoulos, *Science.* **1999**, 286, 945-947.

15. H. Wang, Z. Liu, M. F. Lo, T. W. Ng, C.S. Lee, D. Yan, S.T. Lee, *J. Appl Phys.* **2010**, 107, 024510.

16. S. P. Singh, Z.E. Ooi, S. N. L. Geok, G. K. L. Goh, A. Dodabalapur, *Appl. Phys. Lett.* **2011**, 98, 073302.

17. S. Braun, W. Osikowicz, Y. Wang, W. R. Salaneck, *Org. Elec.* **2007**, 8, 14-20.

18. B. N. Pal, J. Sun, B. J. Jung, E. Choi, A. G. Andreou, H. E. Katz, *Adv. Mater.* **2008**, 20, 1023-1028.

19. M. Janda, A. Kubovy *Phys. Stat. Sol.* **1976**, 35, 391-402.

20. S.Chaudhuri, B. Chakrabarati, G. L. Malhotra, A. K. Pal, *J. Appl. Phys.* **1980**, 51, 4111-4114.

21. T. Hoffmann, B. Fideler, T. Kluck, J. Petermann, J. Martinez-Salazar, *Thin Solid Films.* **1994**, 245, 272-276.

22. T. Hoffmann, J. Martinez-Salazar, P. Herrero, J. Peterman, *Phys. Rev. B* **1997**, 55, 1858-1863.

23. H. Torii, M. Tsuji, Kawaguchi, *J. Mater. Research* **1996**, 11, 970-980.

24. Z.Q. Gao, W.Y. Lai, T.C. Wong, C.S. Lee, I. Bello, S.T. Lee, *Appl. Phys. Lett.* **1999**, 74, 3269.

25. B. M. Dhar, R. Ozgun, T. J. Dawidcyk, A. G. Andreou, H. E. Katz, *Mater. Science Eng. R* **2011**, 72, 49-80.

26. I. H. Campbell, *Phys. Rev. B* **1996**, 54, 14321-14324.

27. H. Sugimura, K. Hayashi, N. Saito, N. Nakagiri, O. Takai, *Appl. Surf. Science* **2002**, 188, 403-410.

28. P. Paoprasert, B. Park, H. Kim, P. Colavita, R. J. Hamers, P. G. Evans, P. Gopalan, *Adv. Mater*. **2008**, 20, 4180-4184.

29. W. Chen, D. Qi, X. Gao, A. T. S. Wee, *Prog. Surf. Science* **2009**, 84, 279-321.

30. J. H. Kim, S. W. Yun, B.-K. An, Y. D. Han, S.-J. Yoon, J. Joo, S. Y. Park, *Adv. Mater.* **2013**, 25, 719-724.

31. J. X. Tang, C. S. Lee, S. T. Lee, *J. Appl. Phys.* **2007**, 101, 064504.

32. S. Braun, W. R. Salaneck, M. Fahlman, *Adv. Mater.* **2009**, 21, 1450-1472.

33. L. He, C. Jiang, D. Lai, H. Wang, *Appl. Phys. Lett.* 99, 021104.

34. H. Wang, Z. Liu, M. F. Lo, T. W. Ng, C.S. Lee, D. Yan, S.T. Lee, *J. Appl. Phys.* **2010**, 107, 024510.

35. R. M. Ireland, T. J. Dawidcyk, P. Cottingham, T. McQueen, G. Johns, N. Markovic, L. Zhang, P. Gopalan, H. E. Katz, *ACS Appl. Mater. Interf.* **2013**, 5, 1604-1611.

36. B. N. Pal, J. Sun, B. J. Jung, E. Choi, A. G. Andreou, H. E. Katz, *Adv. Mater.* **2008**, 20, 1023-1028.

37. J. Sinha, R. M. Ireland, S. Lee, H. E. Katz, *MRS Communications* **2013**, 3, 97-100.

38. Y. Tanabe, K. K. Huynuh, R. Nouchi, S. Heguri, G. Mu, J. Xu, H. Shimotani, K. Tanigaki, *J. Phys. Chem. C* **2014**, 118, 3533-3538.

39. B. He, T.-W. Ng, M.-F. Lo, C.-S. Lee, W. Zhang, *ACS Appl. Mater. Interf.* **2015**, 7, 9851-9857.

40. S. S. Hong, J. J. Cha, D. Kong, Y. Cui, *Nature Communications* **2012**, 3, 757.

41. M. T. Edmonds, J. T. Hellerstedt, A. Tadich, A. Schenk, K. M. O'Donnell, J. Tosado, N. P. Butch, P. Syers, J. Paglione, M. S. Fuher, *ACS Nano* **2014**, 8, 6400-6406.

42. G. D. Yuan, T. W. Ng, Y. B. Zhou, F. Wang, W. J. Zhang, Y. B. Tang, H. B. Wang, L. B. Luo, P. F. Wang, I. Bello, C. S. Lee, S. T. Lee, *Appl. Pys. Lett.* **2010**, 97, 153126.

43. M. Kroger, S. Hamwi, J. Meyer, T. Riedl, W. Kowalsky A. Kahn, *Appl. Phys. Lett.* **2009**, 95, 123301.

44. J. Meyer, S. Hamwi, M. Kroger, W. Kowalsky, T. Riedl, A. Kahn, *Adv. Mater.* **2012**, 24, 5408-5427.

45. Y. Zhou, C. Fuentes-Hernandez, J. Shim, J. Meyer, A. J. Giordano, H. Li, P. Winget, T. Papadopoulos, H. Cheun, J. Kim, M. Fenoll, A. Dindar, W. Haske, E. Najafabadi, T. M. Khan, H. Sojoudi, S. Barlow, S. Graham, J.L. Bredas, S. R. Marder, A. Kahn, B. Kippelen, *Science.* **2012**, 336, 327-332.

46. K. C. See, J. P. Feser, C. E. Chen, A. Majumdar, J. J. Urban, and R. A. Segalman, *Nano Lett.* **2010**, 10, 4664.

47. S. K. Yee, N. E. Coates, A. Majumdar, J. J. Urban, R. A. Segalman. *Physical Chemistry Chemical Physics* **2013**, 15, 4024.

48. N. E. Coates, S. K. Yee, B. McCulloch, K. C. See, A. Majumdar, R. A. Segalman, and J. J. Urban. *Adv. Mater.* **2013**, 25, 1629.

49. C. H. Cartwright. *Annalen Der Physik.* **1933**, 18, 656.

50. S. K. Ramasesha, A. K. Singh. *Philosophical Magazine B-Physics of Condensed Matter Statistical Mechanics Electronic Optical and Magnetic Properties* **1991**, 64, 559.

51. S. R. Hostler, P. Kaul, K. Day, V. Qu, C. Cullen, A. R. Abramson, X. F. Qiu, and C. Burda. for *Thermoelectrics ITHERM '06 10th Intersoc. Conf*, **2006**, pp. 1400-5 ().

52. M. T. Khan, A. Kaur, S. K. Dhawan, and S. Chand. *J. Appl. Phys.* **2011**, 110, 044509.

# CHAPTER 2

# Field-Effect Transistor Application

## Introduction

Organic field-effect transistors (OFETs) are increasingly considered for low-cost, low-power electronic applications such as radio frequency identification (RFID) tags, light-emitting diode (LED) displays, and sensors due to continuous development of their device performance and stability.[1-4] Their advantages stem mainly from processing and mechanical attributes, therefore, inorganic materials that are amenable to similar processing methods and temperatures could be used in "organic electronics" platforms, either alone or in hybrid devices with organic partners.

OFETs comprise of a gate electrode supplying gate voltage $V_g$, a gate dielectric, a semiconducting film typically of 10-100 nm thickness in which a charge channel forms, and source/drain electrodes between which current $I_d$ flows, driven by drain voltage $V_d$. In a thin-film configuration OFETs are associated with complex electronic functionality, simple processing, transparency, and mechanical flexibility. These advantages could be realized from inorganic semiconductors as well, in the form of easily deposited films and nanostructures.[5-9] To this day organic semiconductor (OSC) molecules have the highest operating performances compared to their polymer counterparts, and sublimed films show the greatest crystallinity/performance compared to polycrystalline films deposited from solution. Still, OFETs suffer from high power requirements and lower carrier mobilities, which must be addressed before reaching their potential as circuit components.

Besides the intrinsic bulk properties of OSCs, charge transfer in OFETs is governed by injection barriers at the electrodes and electronic traps at the semiconductor/dielectric interface. Under an applied gate potential, mobile charges injected at the electrodes accumulate near the dielectric to form a planar conducting channel.[10] For typical accumulation-mode OFETs, traps at the interface must first be filled before conduction from source to drain electrodes becomes significant, and so the number of traps determines how much power is required to turn the device On. Therefore the semiconductor/dielectric interface plays a crucial role in the operation of single component OFETs. For OFETs containing heterojunctions, two dissimilar semiconductors in direct contact, the critical charge channels form at the interface between semiconductor components, which is a more complicated system. Understanding these factors has led directly to the development of commercially viable organic electronics, such as LEDs, RFID tags, photovoltaic cells, and ambipolar transistors that function as both n- and p-type. Accordingly there is a strong need to better comprehend the underlying physics of heterojunction effects to ensure further progress.

In a recent study, we described vapor-deposited elemental tellurium (Te) films with a wide variety of morphologies on differing substrates.[9] In particularly favorable cases, with Te deposited on an organic semiconductor (OSC), charge carrier (hole) mobility ($\mu$) was >3 $cm^2\ V^{-1}\ s^{-1}$. However, this $\mu$ coincided with mostly depletion-regime activity, loss of field effect once reaching the accumulation regime, and poor saturation at high depletion voltages. To better understand the reasons for the observed field effect behaviors, we investigated local static electric fields spontaneously formed at the Te-organic interfaces, which are discussed in the following section, and in the last section of

the chapter we discuss effects of intentional static charge implantation using a charging method.

In this section we explore the heterojunction effects between OSC thin films and tellurium, an inorganic elemental semiconductor with rich history. Advantages to elemental semiconductors include simplicity of structure, well-known intrinsic properties, and no need for additional synthesis or chemical modification after purification. Tellurium is a great candidate for combining with organic materials because of its extensive performance capabilities and low processing requirements. A wide range of structural properties, and thus electronic properties, can be achieved over a wide range of processing methods. The semi-metal behavior also makes tellurium unique for studying organic-inorganic heterojunctions because organic-metal junctions are fairly understood.

Before silicon was developed for high performance electronic and optical devices, tellurium was among the most studied elemental semiconductors. Since it has been used in electronic devices prior to the development of silicon and compound semiconductors, both bulk and thin film properties for tellurium are well-understood; it has a high work function (4.9 eV), low resistivity (few tenths of an Ohm.cm), and a narrow band gap (0.34 ev); it resists oxidation to air, can be easily evaporated without dissociation, and has a low melting temperature in atmosphere (440C). Most compounds are too heavy to deposit by thermal evaporation without breaking apart first. Despite the advantages, tellurium is not a conventional material seen in electronic devices. This is because silicon has shown high performance and stands ubiquitous in nature.

Although tellurium's natural occurrence is rare, 40% of the world's tellurium production comes from the United States as a byproduct of refining copper and lead

(World Mineral Production, 2009). More importantly, tellurium shows advantageous thermoelectric properties, soft x-ray absorption, blue and ultraviolet light adsorption, and infrared detection. Tellurium thin film transistors were shown to exceed 100-MHz and one-watt capabilities.[11] Directly combining tellurium atoms with organic molecules via chemical synthesis to form hybrid nanostructured materials is another field of considerable. This class of materials, called organochalcogens, has received more attention in the past few years due to the increasing awareness of its technological potential. Zhang et al. focus particularly on the packing arrangements and crystal motifs exhibited by planar aromatic molecules, which may be benefited by functionalization with chalcogen atoms, such as S, Se and Te. Huang et al. demonstrated good mechanical flexibility and low thermal conductivity of hybrid organic-telluride molecules.[4] Many similar works foreshadow the potential of organic-tellurium compounds for electronic, thermal, and photovoltaic applications, yet very few papers study their direct application as such. Although organochalcogens are one material, free of abrupt interfaces common of conventional composites, we find that heterojunction effects have their own advantages which should not be overlooked.

Compared to compound semiconductors, Te is an attractive material to use in conjunction with organic devices because only a single element is involved, and its properties are well studied, such as piezoelectric, thermoelectric, catalytic, photoconductive, and non-linear optic behavior. Te crystal structure is highly anisotropic, attributed to the covalent bond between atoms within spiral chains, which align in parallel through van der Waals forces to form the hexagonal Te unit cell.[12] The helical structure results in strongly overlapping molecular orbitals between chains and a highly percolated

thin-film structure, favoring charge carrier transport. Te is normally twofold coordinated when molecules of Te come together. The lone electron pair created by two nonbonding valence states forms a pseudo-valence band which dictates tellurium's semiconductor properties (i.e. the energy band gap, 0.34 eV).

**Figure 1** shows the general platform used for studying Te hybrid devices, comprising multilayer films of Te and an OSC deposited onto Si-$SiO_2$ substrates (100 nm oxide). Gold source and drain electrodes were deposited (50 nm thick) by thermal evaporation through a shadow mask with four different dimensions (W/L ratios of 80, 53, 40, and 32). Devices were fabricated using bare oxide, oxide modified with molecular monolayers, and oxide modified with polystyrene. We consider Te as an inorganic nanostructured semiconductor[13-18] on top of organic semiconductors pentacene or 5,5'-bis(4-hexylphenyl)-2,2'-bithiophene (6PTTP6).[19-21] We focus on bilayers of Te deposited onto 6PTTP6, and trilayers of Te sandwiched between two 6PTTP6 layers (as shown in Figure 1). **Figure 2** shows the chemical structure of all the materials used in this chapter, including the tellurium unit cell (a), a poly(styrene) polymer (g), small organic molecules which can be vacuum deposited (b-f), and small organic molecules which can functionalize onto the $SiO_2$ surface from solution or vapor phase (h-j).

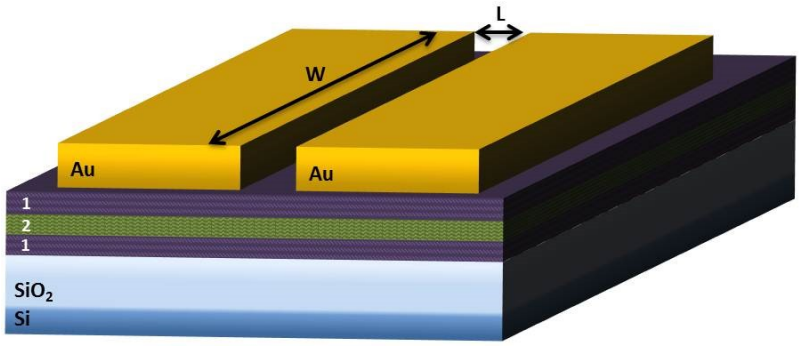


**Figure 1.** General schematic for trilayer OFET structure; three thin-films deposited onto 100 nm thick bare silicon dioxide are represented as materials number 1 and 2; material 1 is generally the OSC and material 2 is Te, and each semiconductor is nominally deposited to 10 nm. Gold source and drain electrodes were deposited (50 nm thick) with four different W/L ratios of 80, 53, 40, and 32.

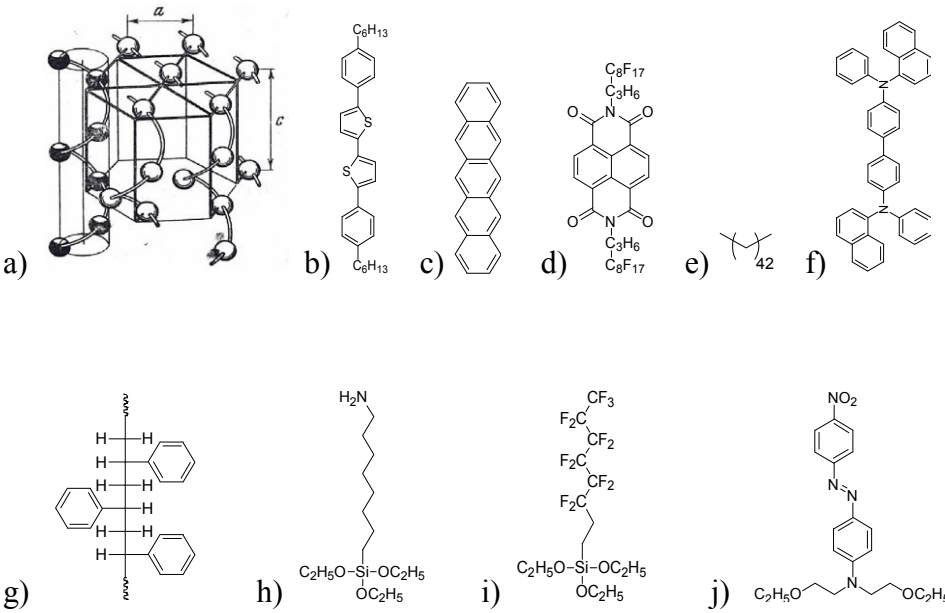


**Figure 2.** a) Te unit cell (a=0.445 nm, c=0.591 nm) b) 5,5'-bis(4-hexylphenyl)-2,2'bithiophene (6PTTP6) c) pentacene d) N,N'-bis(3-perfluorooctylpropyl) naphthalenetetracarboxylic diimide (8-3NTCDI) e) tetratetracontane f) N,N'-diphenyl-

N,N'-bis(1-Naphthyl)-1,1'-biphenyl-4,4"-diamine (NPD) g) atactic polystyrene h) (3-aminopropyl)trimethoxysilane i) 1H,1H,2H,2H-perfluorooctyltriethoxysilane j) Disperse Red 19 with triethoxysilane groups (DR19).

During electrical testing, the source electrode is always grounded (0 V), and the drain voltage ($V_D$) is always swept from 0 to -20 V (for p-channel transistors). The drain current ($I_D$) is measured while constant gate voltage ($V_G$) is held between source and gate contacts. Threshold voltage ($V_T$) and mobility ($\mu_{meas}$) were extrapolated from $I_D^{1/2}$ vs. $V_G$ plots using the saturation-regime equation for FET drain current.[10]

$$I_D = \frac{W}{2L}\mu C_i (V_G - V_T)^2 \qquad (1)$$

We perform device characterization by conventional continuous voltage application and by pulsing $V_g$ at 1 kHz. At this time scale, the equilibrium charge distribution is not always reached, and thusly it is shown that field effect behavior can be enhanced at higher frequency. We also employ scanning Kelvin probe microscopy[24] to observe interfacial potential differences, and use a statically charged gate dielectric[23] to alter those interfacial potentials. We show that $V_g$ at which the field effect is lost is significantly influenced by internal fields. More broadly, we illustrate ways in which the essential OFET parameters, generally obtained under DC conditions regardless of the intended applications, are frequency dependent because of the time needed to equilibrate charge distributions with applied fields.

The field-effect charge carrier mobility μ is generally assumed to apply to the entire semiconductor film. Sometimes μ is acknowledged to be dependent on the electric field (gate voltage per unit dielectric thickness, $V_g/d$) applied across the gate dielectric

between the gate electrode and semiconductor.[10] If traps in the semiconductor are filled as $V_g$ increases, μ increases with $V_g$. It is also conceivable that higher $V_g$ can drive the channel of mobile charge carriers from a high-μ bulk region of the semiconductor into a more disordered region of the semiconductor film within 2-5 nm (1-2 molecular monolayers) of the gate dielectric, in which case mobility would decrease as $V_g$ increases.[11]

Importantly, the dependence of μ on the device characterization timescale is rarely considered. Because of the RC time constant of a device test circuit, charge distribution in the semiconductor might not be at the equilibrium expected from the applied voltages. We recently used time-resolved measurements to characterize an OFET containing a fluoroalkylbenzyl-substituted naphthalenetetracarboxylic diimide (NTCDI) on a 3-nm oxide, showing that μ was higher on shorter timescales than on longer timescales, and some of the NTCDI layers closer to the gate dielectric contributed to gate capacitance.[12] This would have been consistent with the charge channel forming farther from the gate dielectric and in a higher mobility region compared to direct current (DC, "zero frequency") conditions.

Time-resolved current-voltage and capacitance measurements can help model charge distribution/transport and explain possible switching/trapping phenomena, or clarify how differences in material transport properties are influential to device performance. Constant $V_G$ measurements accumulate charges in lower semiconducting layers, so most of the charge channel forms at the dielectric interface.[10] The effective charge channel layer may be modulated by the operating frequencies. By pulsing the applied $V_G$ at higher frequencies, the charge channel extends away from the dielectric

interface into higher semiconductor layers because the potential is pulsed too quickly to move charges farther. Previously we have used time-resolved measurements to extensively characterize the low voltage operation of 8-3 NTCDI and the dielectric contributions of its side-chain to gate capacitance of multilayer films.[21] From a technological standpoint, applying the FET gate potential at some low frequency improves the measured carrier mobility because upper layers tend to have better morphology, and interfacial traps are avoided. Pulsing too quickly results in no movement of carriers. However, understanding the time-resolved ability of carriers to move within materials will eventually lead to more efficient devices and improved signal/measurement resolution.

We pulse $V_G$ at 1 kHz, which resulted in much better transistor characteristics for all devices. Pulsing the gate bias resulted in simultaneous decrease in the Off current and increase in the On current for all device configurations, and improved saturation. The measured mobility was increased for all devices operating at low frequency. The performances for bilayer and trilayer hybrids with heated substrates are greatly improved when $V_G$ is applied at 1 kHz. Specific capacitance was measured in Te and hybrid films on bare $SioO_2$, using an electrode area of 0.05 $cm^2$. Current-voltage was measured for the range -20 to 20 V, using bias frequencies 0.1, 1.0, 10, and 100 kHz. Assuming 6PTTP6 has a dielectric constant of 2.1, which is reasonable for small organic molecules, then 10nm of 6PTTP6 on 100nm SiO2 has a theoretical capacitance of 29 nF $cm^{-2}$ using the equations for parallel plate capacitors.[21]

$$C_i = \varepsilon_i \varepsilon_0 \frac{A}{d} \qquad (2)$$

$$\frac{1}{C_{tot}} = \frac{1}{C_1} + \frac{1}{C_2} \quad (3)$$

For the individual material layers, $A$ is electrode area, $d$ is layer thickness, $\varepsilon_i$ is the material dielectric constant, and $\varepsilon_0$ is the vacuum permittivity. The calculated value matches our experimental observation at 0 V (**Figure 3**). We observe that when negative voltage is applied at frequencies greater than 1 kHz, charges don't have the chance to accumulate or move through 6PTTP6 layers.

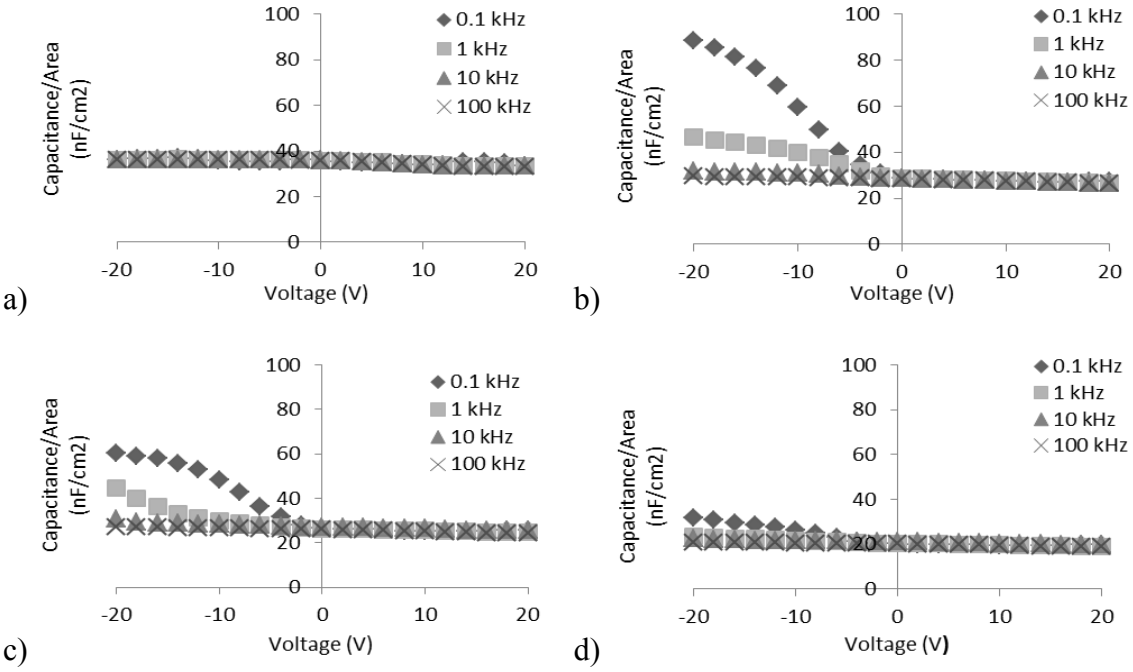


**Figure 3.** Capacitance of hybrid gate stacks using bare oxide for a) bare $SiO_2$, b) 6PTTP6/$SiO_2$, c) Te/6PTTP6/$SiO_2$, d) 6PTTP6/Te/6PTTP6/$SiO_2$

The mobility and on/off ratio were both improved for Te deposited on bare oxide using a heated substrates (2.7 μV/cm$^2$) compared to room temperature (1.8 μV/cm$^2$), as expected. The mobility was enhanced by the 6PTTP6 bilayer when substrates were

heated (3.8 μV/cm$^2$, and were about the same if not heated) and achieved greater mobility with the 6PTTP6 trilayer (5.5 μV/cm$^2$). The $V_T$ for this configuration was among the lowest achieved (16 V) and on/off ratios were among the highest (>10), while maintaining output current in the milliAmps. Unlike the 6PTTP6 bilayer when deposited at room temperature, however, pentacene bilayers had improved mobility compared to Te on bare oxide (reaching 3 μV/cm$^2$), at large costs to $V_T$ and on/off ratio. **Figure 4** shows representative output curves. **Table 1** compares device parameters measured under constant and pulsed bias, and for cases when substrate was held at 55 ˚C.

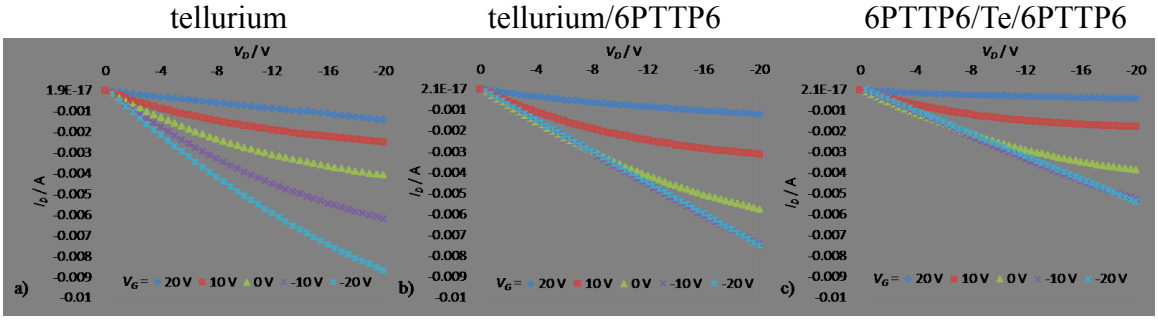


**Figure 4.** Output curves for a) tellurium, b) Te/6PTTP6 bilayer, and c) 6PTTP6/Te/6PTTP6 trilayer. Bare $SiO_2$, substrates held at 55 °C during deposition.

**Table 1.** FET Parameters and Performance under Static or Pulsed Bias, and Heated Substrates

| Semiconductor | Dielectric | Gate bias | $\mu_{meas}$ [$cm^2 V^{-1} s^{-1}$] [a] | $V_T$ [V] [a] | On/Off | $N_s$ [b] |
|---|---|---|---|---|---|---|
| 6PTTP6 [c] | $SiO_2$ | pulsed [e] | 0.028 ± 0.002 | -3.29 ± 0.29 | 4230 ± 70 | 8 |
| | | static | 0.025 ± 0.002 | -1.97 ± 0.31 | 1840 ± 40 | 8 |
| Pentacene [c] | $SiO_2$ | pulsed | 0.053 ± 0.006 | -4.60 ± 0.25 | 21000 ± 1400 | 4 |
| | | static | 0.038 ± 0.001 | -4.00 ± 0.35 | 1400 ± 400 | 4 |
| Te | $SiO_2$ | pulsed | 1.7 ± 0.5 | 42.0 ± 0.8 | 3.38 ± 0.09 | 4 |
| | | static | 1.10 ± 0.06 | 61.6 ± 2.0 | 2.08 ± 0.03 | 4 |
| Te/ 6PTTP6 | $SiO_2$ | pulsed | 1.55 ± 0.04 | 39.1 ± 1.1 | 4.30 ± 0.22 | 20 |
| | | static | 0.82 ± 0.02 | 52.2 ± 1.5 | 2.85 ± 0.10 | 20 |
| Te/pentacene | $SiO_2$ | pulsed | 2.7 ± 0.3 | 110 ± 6 | 1.8 ± 0.08 | 4 |
| | | static | 1.4 ± 0.2 | 150 ± 10 | 1.5 ± 0.05 | 4 |
| 6PTTP6/ Te/6PTTP6 | $SiO_2$ | pulsed | 1.58 ± 0.07 | 26.4 ± 0.64 | 14.9 ± 1.7 | 20 |
| | | static | 0.89 ± 0.05 | 31.5 ± 0.84 | 8.98 ± 0.86 | 20 |
| Te | $SiO_2$ (55°C) [d] | pulsed | 2.68 ± 0.13 | 16.5 ± 0.71 | 10.7 ± 0.85 | 4 |
| | | static | 2.42 ± 0.08 | 29.9 ± 1.8 | 8.00 ± 0.88 | 4 |
| Te/ 6PTTP6 | $SiO_2$ (55°C) | pulsed | 3.84 ± 0.29 | 42.4 ± 3.4 | 3.80 ± 0.59 | 4 |
| | | static | 3.05 ± 0.34 | 48.2 ± 4.8 | 3.28 ± 0.44 | 4 |
| 6PTTP6/ Te/6PTTP6 | $SiO_2$ (55°C) | pulsed | 5.48 ± 0.05 | 16.0 ± 1.3 | 13.0 ± 1.9 | 4 |
| | | static | 3.69 ± 0.13 | 20.1 ± 2.4 | 5.27 ± 0.42 | 4 |
| Te | DR19/$SiO_2$ | pulsed | 1.15 ± 0.23 | 62.5 ± 5.6 | 2.2 ± 0.10 | 4 |
| | | static | 0.33 ± 0.06 | 115 ± 9.9 | 1.6 ± 0.10 | 4 |
| Te | DR19/$SiO_2$ (55°C) | pulsed | 0.016 ± 0.005 | -9.2 ± 0.31 | 1120 ± 705 | 4 |
| | | static | 0.006 ± 0.001 | -7.9 ± 0.47 | 740 ± 236 | 4 |

[a] Mobility $\mu_{meas}$, and $V_T$ values were extrapolated from $I_d^{1/2}$ vs. $V_g$ plots. W/L is 80. [b] $N_s$ is number of samples corresponding to calculated values and standard deviations. [c] Devices measured in the accumulation regime ($V_g$ of 0 to -20 V). Te devices were analyzed in the depletion regime ($V_g$ of 20 to 0 V). [d] Substrates held at 55 °C during deposition, and the others were kept at room temperature [e] Gate voltage was applied in pulses at 1 kHz. Static gate voltage was applied under DC.

Applying the OFET gate potential at low frequencies proves to have a large effect on the ideality of characteristic curves obtained from both single-component tellurium and hybrid OSC-tellurium devices. From a technological standpoint, the pulsed-gate method allows for charge trapping at the conduction channel interface to be avoided, typically leading to improved carrier mobility. However, understanding the time-resolved ability of carriers to move within materials will eventually allow engineering of heterojunctions where the flow of carriers is funneled entirely by design. Previously we have used time-resolved measurements to extensively characterize the low voltage operation and side-chain dielectric contributions of an air-stable n-channel molecule, 8-3 NTCDI.[21]

We conclude the following section by demonstrating tellurium and 8-3 NTCDI in cooperation for ambipolar devices. Here we use an inorganic element and an n-type organic semiconductor to fabricate novel ambipolar transistor devices. Whatever the application, it's clear that electronic behavior depends strongly on the energy band structure of the OSC and its alignment with tellurium. Explaining the underlying physics will allow for a variety of multipurpose devices to be realized, which can have the best attributes of both inorganic and organic materials, such as electrical and mechanical durability, optical and chemical functionality, high mobility, and simple processing.

**References**

1. B. Crone, A. Dodabalapur, Y. Y. Lin, R. W. Filas, Z. Bao, A. LaDuca, R. Sarpeshkar, H.E. Katz, W. Li, *Nature.* **2000**, 403, 521-523.

2. G. H. Gelinck, H. E. A. Huitema, E. Van Veenendaal, E. Cantatore, L. Schrijnemakers, J. Van der Putten, T. C. T. Geuns, M. Beenhakkers, J. B. Giesbers, B. H. Huisman, E. J. Meijer, E. M. Benito, F. J. Touwslager, A. W. Marsman, B. J. E. Van Rens, D. M. De Leeuw, *Nature Mater.* **2004**, 3, 106-110.

3. D. Braga, G. Horowitz, *Adv. Mater.* **2009**, 21, 1473-1486.

4. H. E. Katz, J. Huang, *Thin-Film Org. Elect. Dev.* **2009**, 39, 71-92.

5. C. R. Kagan, D. B. Mitzi, C. D. Dimitrakopoulos, *Science* **1999**, 286, 945-947.

6. B. A. Ridley, B. Nivi, J. M. Jacobson, *Science* **1999**, 286, 746-749.

7. B. N. Pal, B. M. Dhar, K. C. See, H. E. Katz, *Nature Mater.* **2010**, 8, 898-903.

8. M. R. Perez, I. Mejia, A. L. Salas-Villasenor, H. Stiegler, I. Trachtenberg, B. E. Gnade, M. A. Quevedo-Lopez, *Org. Elect.* **2012**, in press.

9. R. M. Ireland, P. Gopalan, H. E. Katz, *Adv.Mater.* **2012**

10. G. Horowitz, *J. Mater. Research* **2004**, 19, 1946-1962.

11. H. L. Wilson, W. A. Gutierrez, *IEEE Lett.* **1967**, 415-416.

12. M. J. Capers, M. White, *Thin Solid Films* **1971**, 8, 353-357.

13. A. De Vos, B. Hindryckx, . *Proc. IEEE* **1980**, 127, 42-44.

14. H. Torii, M. Tsuji, J. Kawaguchi, *J.Mater. Res.* **1996**, 11, 970-980.

15. T. Hoffmann, J. Martinez-Salazar, P. Herrero, J. Peterman, *Phys. Rev. B* **1997**, 55, 1858-1863.

16. L.B. Luo, F.X. Liang, X.L. Huang, T.X. Yan, J.G. Hu, Y.Q. Yu, C.Y. Wu, L. Wang, Z.F. Zhu, Q. Li, J.S. Jie, *J. Nanopart. Res*. **2012**, 14:967.

17. M. L. Tiago, J. E. Northrup, S. G. Louie, *Phys. Rev. B* **2003**, 67, 115212.

18. J. Huang, J. Sun, H. E. Katz, *Adv. Mater.* **2008**, 20, 2567-2572.

19. J. Huang, H. E. Katz, J. E. West, *Langmuir* **2007**, 23, 13223-13231.

20. C. D. Dimitrakopoulos, P. R. L. Malenfant, *Adv. Mater.* **2002**, 14, 99-117.

21. B. J. Jung, J. F. Martinez-Hardigree, B. M. Dhar, T. J. Dawidcyzk, J. Sun, K. C. See, H. E. Katz, *ACS Nano* **2011**, 5, 2723-2734.

**Interfacial Fields in Tellurium-Organic Hybrids**

Studies of evaporated thin-film Te on salt single crystals,[1] amorphous glass,[2-7] and polymer dielectrics,[8-10] have revealed a range of possible morphologies, and correlated them with some electrical properties. Te initially forms amorphous islands/grains when thermally deposited onto glass substrates held at room temperature, which become polycrystalline films upon exposure to air, or heat.[11,12] Above 50 °C, vapor-deposited Te immediately forms crystalline structures with uniaxial and elongated shape, which has also been shown for Te evaporated directly onto insulating organic polymers.[12-15] Orientation of Te crystallites with respect to oriented poly(1-butene) fibers was achieved using substrates temperatures above 50 °C during deposition.[14] Substrate temperatures above 150 °C were required to grow aligned Te crystallites parallel to poly-1,4-phenylene fibers.[15]

Scanning Electron Micrography (SEM) is used to characterize resultant thin film morphologies. Attention is then paid to the work function alignment in order to investigate possible energy dependent scattering, and shifting quasi-Fermi levels. The electrical properties of 6PTTP6-Te interfaces are investigated by current-voltage measurements of transistor and diode architectures, as described above, and Kelvin Probe Microscopy (KPM) of the heterointerface at the end of this section. Lastly, thermoelectric

measurements provide further insight, and may prove to be an effective method for determining the magnitude and effectiveness of scattering processes due to tellurium films as-processed.

We experimentally investigated hybrid devices comprising vacuum-deposited tellurium and both semiconducting and insulating organic films. Te morphology and thus mobility are both strongly modulated by the underlying organic. Te thin-film growth ranges from dense to sparse and semispherical to rod-like, or needle-like, depending strongly on both the substrate and deposition conditions. X-ray diffraction confirms that Te films are polycrystalline on both glass and OSC substrates (**Figure 5**). Te has the hexagonal unit cell and orients itself with its c-axis at an angle to each substrate upon crystallization, but OSC substrates result in less crystallinity due to increased roughness and lower surface-energy compared to glass substrates. The shape and size of polycrystalline Te grains, however, depend greatly on the substrate.

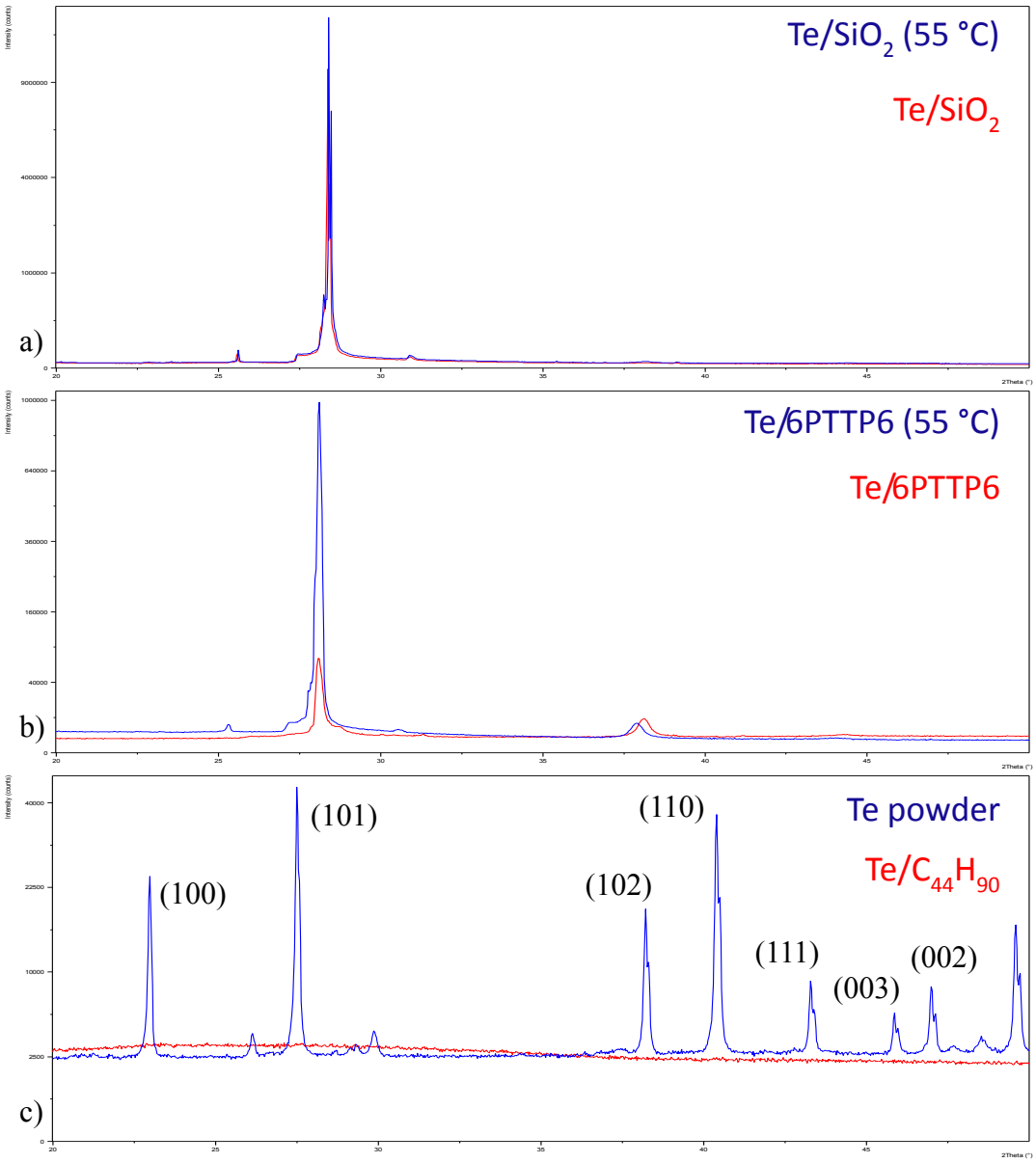


**Figure 5.** X-ray diffraction of tellurium films deposited onto a) glass, b) 6PTTP6 on glass, and tetratetracontane ($C_{44}H_{90}$) on glass.

**Figure 6** shows scanning electron micrographs of various Te morphologies and nanostructures when deposited onto some materials. Te morphology appears as granular crystallites with submicron diameter. We observed semispherical, rod-like, rod, and

needle crystallite structures. Rod-like refers to morphology where semispherical (rounded) grains coalesce to form worm-like structures, or peapods, of interconnected globular crystallites. Deviation from densely-packed semispherical crystallites is seen for systems with either additional thermal energy or low surface energy. Crystallites are able to coalesce in these cases, producing larger grains and alternative forms.

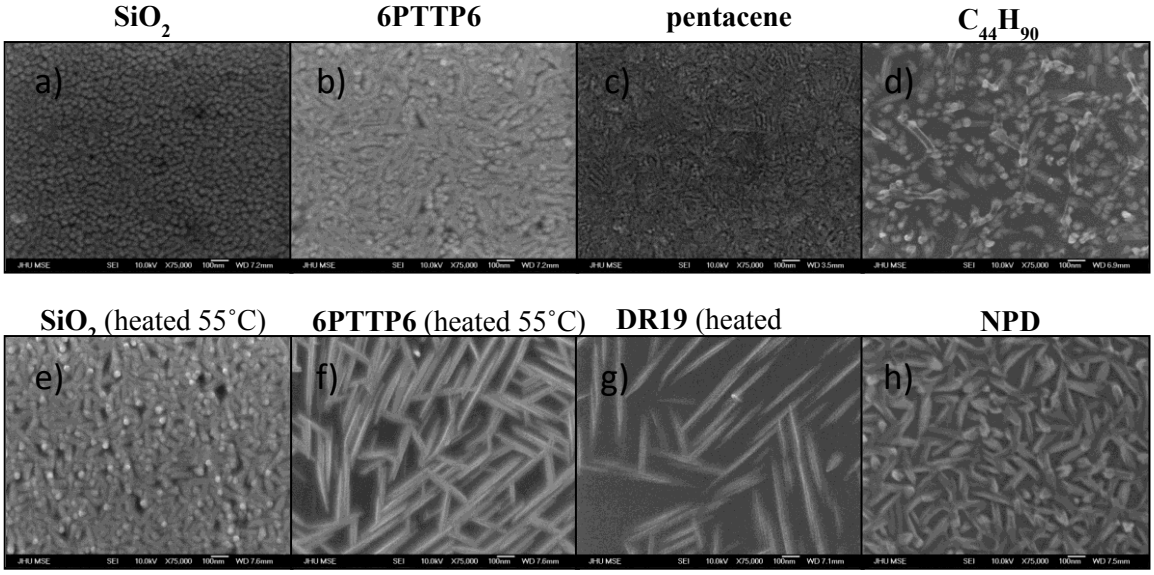


**Figure 6.** Scanning electron micrographs of Te morphology when deposited at 0.3 Å $s^{-1}$ onto various organic thin-films, including a) $SiO_2$, b) 6PTTP6, c) pentacene, d) tetratetracontane ($C_{44}H_{90}$), e) SiO2 while substrate held at 55 ˚C, f) 6PTTP6 while substrate held at 55 ˚C, g) Dr19 monolayer while substrate held at 55 ˚C, and h) NPD.

For Te films deposited at 0.3 Å $s^{-1}$ on bare oxide at room temperature, the percolation threshold was 8 nm nominally. That is, we saw no conduction (current < 100 nA at 1 V) for thin-films deposited to less than this value. Using a higher deposition rate (3.0 Å $s^{-1}$) resulted in grains which are more densely packed. We obtained similar

percolation values to others for Te deposited on glass or polymers at ~3.0 Å $s^{-1}$, around 5 nm.[16,17] Tellurium deposited at 10.0 Å $s^{-1}$ on bare $SiO_2$ had no granular morphology or appearance of crystallites. The effect of higher deposition rates (3.0 and 10.0 Å $s^{-1}$) on Te morphologies can be seen in **Figure 7**.

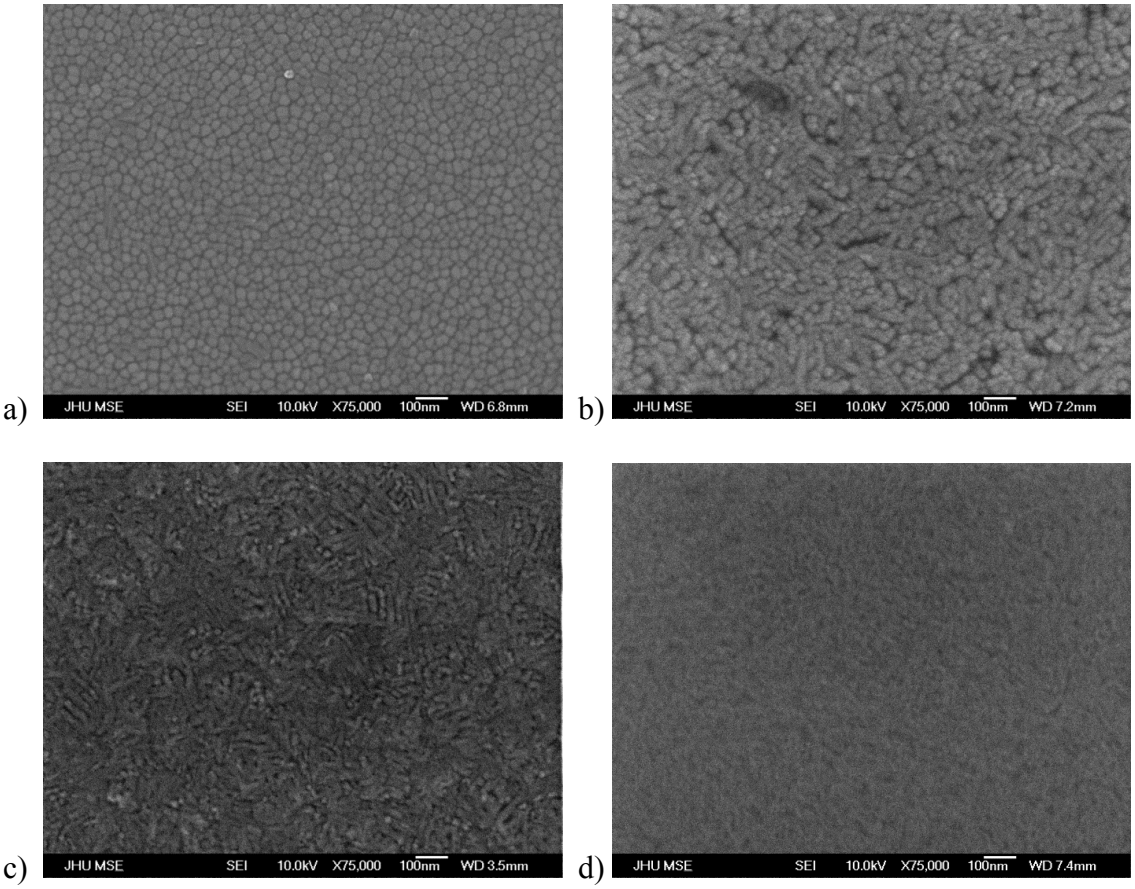


**Figure 7.** a) SEM micrograph of Te deposited on $SiO_2$ at 3.0 Å $s^{-1}$. b) Te deposited on 6PTTP6/$SiO_2$ at 3.0 Å $s^{-1}$. c) Te deposited on pentacene/$SiO_2$ at 3.0 Å $s^{-1}$. d) Te deposited on $SiO_2$ at 10.0 Å $s^{-1}$.

Hereafter, we consider films of Te and OSCs using a single low deposition rate (0.3 Å $s^{-1}$) and nominal film thickness (10 nm of each semiconductor material). OSC and Te films were thermally evaporated in succession during the same vacuum cycle at base pressures below $3x10^{-6}$ Torr. Substrates were held at room temperature during deposition, and also at 55 °C for comparison. Heated substrates enhance packing of 6PTTP6 molecules,[18] and crystallization of Te deposited by thermal evaporation.[11-13]

Tellurium films deposited onto silicon dioxide at room temperature appear as semispherical crystallites with diameters ~ 40 nm (**Figure 6a**). Thin films deposited at a substrate temperature of 55 °C yielded randomly-oriented rods, lying parallel to the substrate (**Figure 6e**). Both unheated and heated substrates gave complete surface coverage, although the latter reveals some voids due to the small aspect ratio (~ 2.5). Semispherical Te grains coalesce to form dense rod-like structures when deposited onto 6PTTP6 films at room temperature, having widths of the same dimension as Te crystallites on bare $SiO_2$ (**Figure 6b**). Sharp needle-like crystallites form for Te deposited onto 6PTTP6 (Te/6PTTP6) when the substrate is heated 55 °C during deposition, revealing anisotropic orientation lying parallel to the substrate, and large voids (**Figure 6f**). The needle-like crystallites also have the similar width to thin films deposited on $SiO_2$, but with larger aspect ratios of 5-15. The needle-like morphology observed for Te/6PTTP6 with substrates held at 55 °C was obtained again when Te was deposited onto DR19 at 55 °C (**Figure 6g**).

Micrographs show somewhat similar, but different structures for Te deposited onto pentacene (Te/pentacene) compared to Te/6PTTP6 at room temperature. Te forms semispherical crystallites on pentacene, but the diameters range from 20-50 nm (**Figure**

**6c**). Crystallites on pentacene coalesce differently also, forming distinct domains between larger and smaller grains, rather than randomly oriented structures. These differences are likely due to the respective morphologies of OSCs. Te deposited on tetratetracontane did not form continuous films, which appear to be nanoribbons (**Figure 6d**). Te on NPD gave more uniform shape and coverage, but also appears more like ribbons than rods (**Figure 6h**).

Consistently, we found that Te growth is sparse on fluorinated surfaces. Te forms discrete semispherical grains when deposited onto polycrystalline 8-3 NTCDI, with diameters 20-30 nm for nominally 4 nm of Te. Away from the gold electrodes, semispherical grains are sparse and align to form long-range networks, seemingly along terraces of underlying 8-3 NTCDI islands. The surfaces between source-drain electrodes, less than 100 micrometers from electrodes, reveal densely packed semispherical grains of the same diameter. It's known that Te nucleates preferentially near predeposited gold contacts.[13] Metal "decoration" is due to decreased interfacial energies at particular sites for deposition of certain metals onto polymer crystal or macromolecular surfaces. Most surprisingly, tellurium nanoribbons and nanorods can be seen on the surface of 8-3 NTCDI (**Figure 8**).

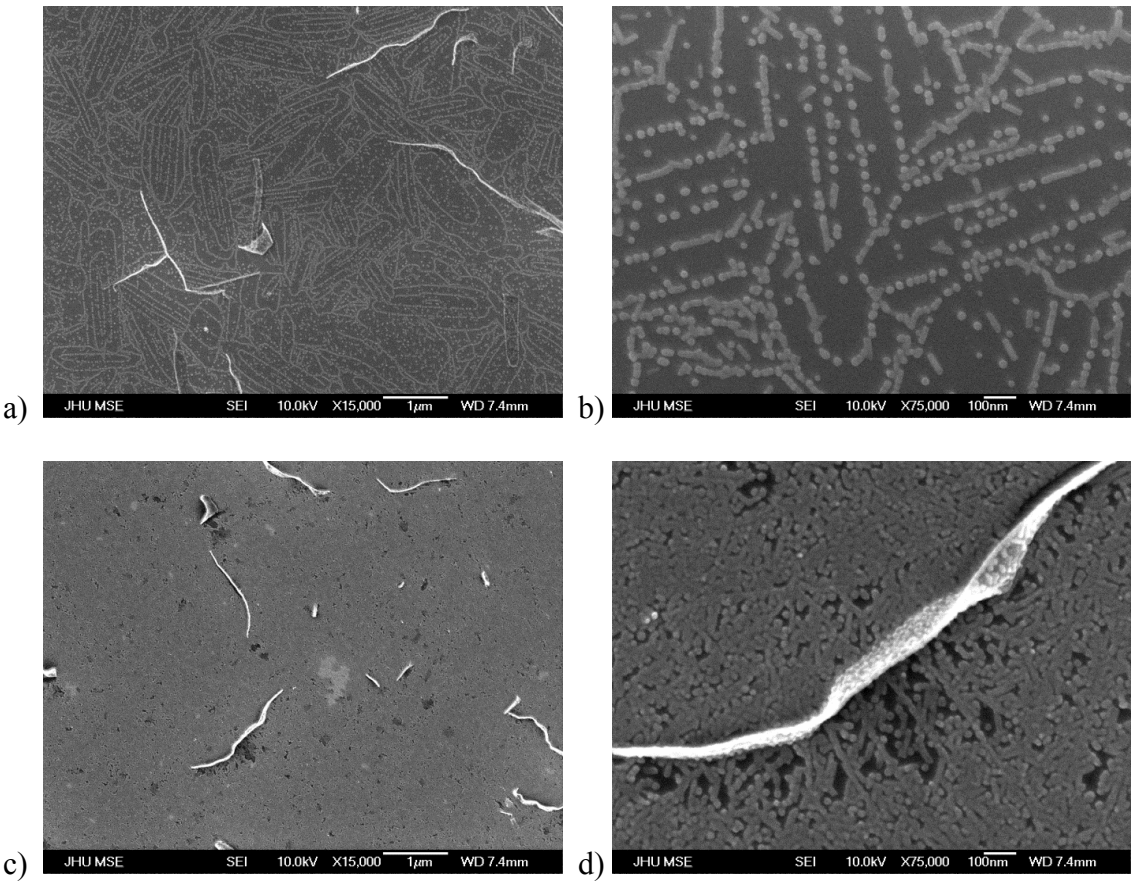


**Figure 8.** a-b) SEM micrograph of 4 nm Te on 8-3 NTCDI, located away from the source-drain electrodes c-d) 4 nm Te on 8-3 NTCDI, located inbetween source-drain electrodes.

Inhibited growth of large tellurium grains was observed on fluorinated side-chains of 8-3 NTCDI. This Te morphology proves useful for designing devices which transport holes and electrons (ambipolar) rather than forming a p-channel or n-channel exclusively. 8-3NTCDI OFETs with predeposited gold electrodes will give clear ambipolar behavior when capped with very thin Tellurium, nominally 4 nm (see Fig. 4c-d for morphology). The mobilities calculated from the initial experiment are low, magnitude of $10^{-5}$ $cm^2$ $V^{-1}$ $s^{-1}$ for both holes and electrons. The mechanism for ambipolar transport, however, may be

interesting. Tellurium networks on the surface of 8-3 NTCDI facilitate formation of p-channels, and this effect is very strong. Initial devices behaved p-channel mostly, and becomes n-channel when sufficient positive gate is applied in order to accumulate electrons in 8-3 NTCDI. This occurred above 20 $V_G$ for our first devices. OFETs encapsulated with more than 4 nm of Te behaved as resistors only.

Bilayer devices with 10 nm of Te deposited on 20 nm of 8-3 NTCDI prior to gold electrodes behaved as n-channel only, which could be due to a couple factors: the Te structure on fluorinated side chains, and the proximity of NTCDI to the dielectric interface. Devices with 8-3 NTCDI above Te behaved as Te-alone, but with a series resistance between Te and the electrodes. When Te was used as the electrode material, 8-3 NTCD1/Te was an effective configuration to turn OFF devices. We obtained p-type conduction in accumulation mode ($V_G$ from 0 to -20 V), with some depletion necessary ($V_T$ ~ 6 V). However, the On/Off current ratio is still low (~ 15), and mobility decreased an order of magnitude relative to Te/$SiO_2$. Output and transfer curves for this configuration are shown in (**Figure 9**).

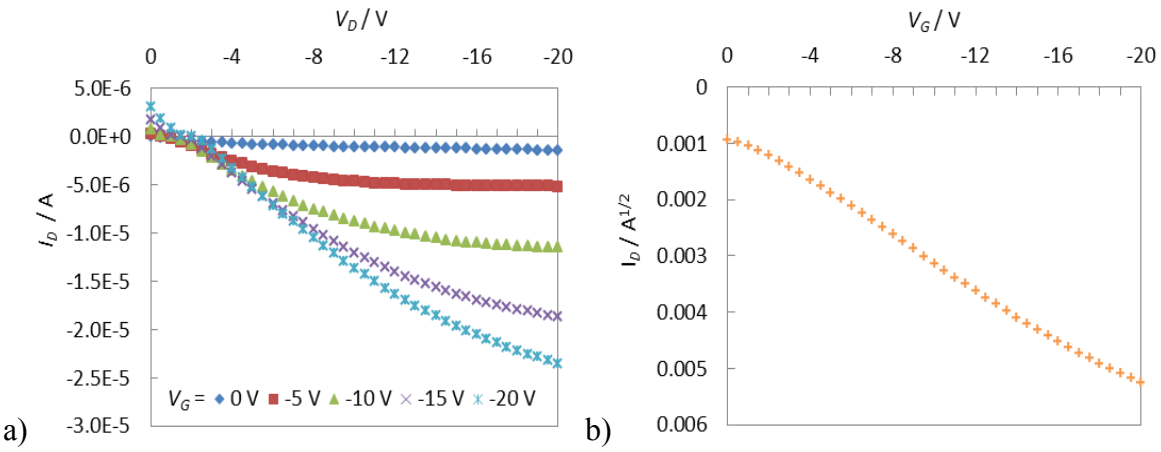


**Figure 9.** a-b) $I_D$ vs. $V_D$ plot for 8-3NTCDI/Te on $SiO_2$ at room temperature with top contact Te electrodes. W/L is 80. b) $I_D^{1/2}$ vs. $V_G$ plot

To help explain the 10-15 volt difference in field effect ranges between Te/6PTTP6 and Te/pentacene bilayers and the reason for field effect loss altogether, we performed scanning Kelvin probe microscopy (SKPM) on lateral boundaries at the interface between the bilayer materials deposited side-by-side. SKPM measures local variations in surface potential across an interface by scanning the junction at some distance above the surface (200 nm in this case), and then retraces the height profile while measuring changes in potential.[19] Here, SKPM qualitatively reveals the surface potential difference between a single 6PTTP6 layer and Te deposited onto 6PTTP6 as a bilayer, and between a single pentacene layer and Te/pentacene. Due to the limitations of shadow masks in our fabrication process, quantification of the potential difference spanning an entire sample was not possible because the diffuse interface is wider than the maximum scan length of our instrument (~ 40 μm) by a factor of 2-3. Regardless, the relative polarities on either sides of interfaces are straightforward to interpret.

The results are shown in **Figure 10**, which indicate potential differences of opposite sign for 6PTTP6 and pentacene relative to Te on those OSCs. 6PTTP6 has more negative surface potential than Te deposited thereon. This indicates that holes are more stable in Te relative to 6PTTP6**.** Conversely**,** SKPM scans show pentacene with more positive surface potential than Te/pentacene. Therefore, pentacene more readily accepts holes from (donates electrons to) Te at equilibrium. The measured potentials are consistent with losing field-effect in hybrid FETs at more positive $V_G$ for Te/pentacene than Te/6PTTP6. The barrier to driving holes from the source through the Te into the organic is lower for pentacene than for 6PTTP6, so given the lower mobilities of the OSCs relative to Te, the increase of source-drain conductance resulting from making $V_g$ less positive ends at a more positive $V_g$ with pentacene. This is consistent with the relative energy band compositions (**Figure 11**). The highest occupied molecular orbital (HOMO) and lowest unoccupied molecular orbital (LUMO) values of 6PTTP6 are estimated as those reported for 2,5-dihexyltetrathiophene,[20] which is expected to be slightly more electron donating than 6PTTP6. A consequence of the Te/6PTTP6 interfacial voltage is the stabilization of holes in the Te layer of a 6PTTP6/Te/6PTTP6 trilayer, which had the highest μ of the useful heterostructures from our previous study.

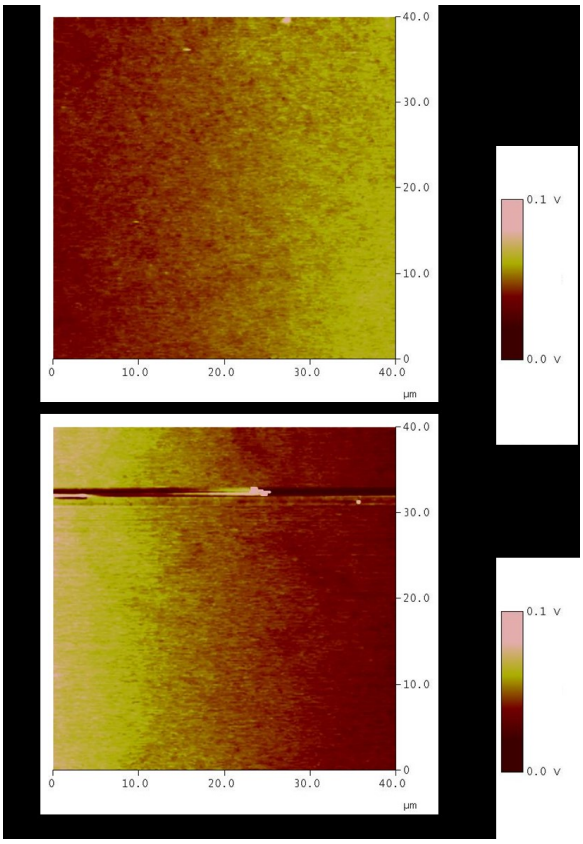


**Figure 10.** 2D SKPM surface potential scans across interfaces of OSC and Te deposited on top of the OSC for 6PTTP6 vs. Te/6PTTP6 (top, from left to right), and pentacene vs. Te/pentacene (bottom, from left to right).

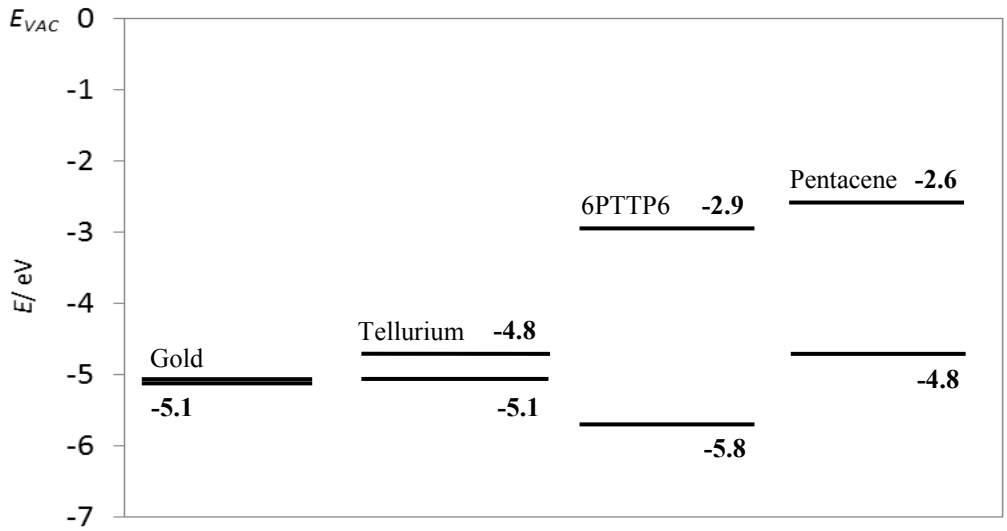


**Figure 11.** Energy band diagram of isolated intrinsic materials.

The interlayer potential created over each 2D interface plays a significant role in charge transport, accumulation and trapping. For instance, the pentacene HOMO level is more positive than the work function of Te, and implies that it accepts holes from Te more readily than 6PTTP6, having a HOMO level more negative than the Te work function.[21] Consequently, scattering of charges at the pentacene-Te interface may be reduced compared to 6PTTP6 and glass interfaces. This was substantiated by thermoelectronic measurements of Te films and bilayers. Te vapor-deposited as a nominal 10 nm film onto unheated Corning glass showed a positive Seebeck coefficient of 400 ± 10 μV/K. Te deposited on 6PTTP6 acted with the same polarity and improved Seebeck, 457 ± 6 μV/K. Possible reasons for this are introduction of new hole energy levels at the 6PTTP6 interface that were not present in Te-on-glass, or increased surface area of crossing Te nanowires, with which additional energy states could be associated. Although the nanocrystalline network on glass showed conductivity of 227 ± 21 S/m, and

the hybrid bilayer shows conductivity of 216 ± 16 S/m (accounting for the thickness of Te only, about 10 nm, measured by quartz crystal microbalance during deposition), the resulting power factor ($S^2\sigma$) was enhanced from 36 ± 3 to 45 ± 4 W/mK$^2$. Pure 6PTTP6 has essentially a very low conductivity (less than 0.01 S/m), so we conclude that changes in power factor are completely due to charge transport being affected in Te. In this case, the bilayer provides an enhancement in Seebeck without compromising conductivity drastically. Pentacene bilayers resulted in similar Seebeck to 6PTTP6 bilayers (468 ± 9 μV/K), but with more conductivity (266 ± 36 S/m), producing higher power factors (58 ± 6 W/mK$^2$). With optimization, these values compare favorably to other hybrid systems.[22,23] Typical plots are shown in **Figure 12**, and the performance data is compiled in **Table 2**.

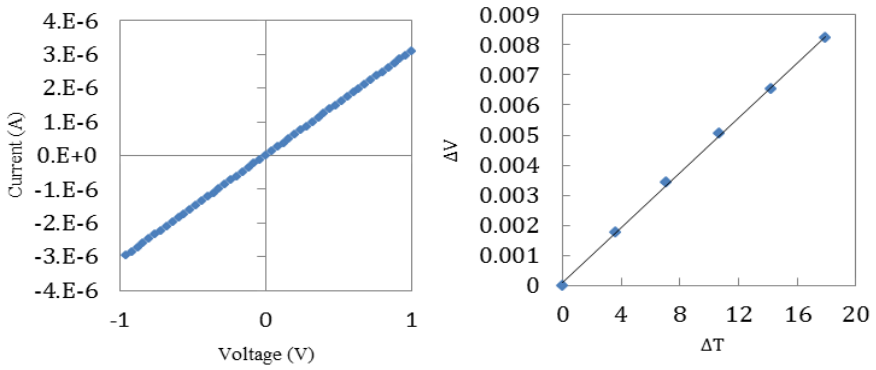


**Figure 12.** Plots used to calculate resistance (left) and Seebeck (right) for typical Te on 6PTTP6 sample.

**Table 2.** Thermoelectric Performance of Te, 6PTTP6, and Te/OSC bilayers

| Device | Conductivity (S/cm) | Seebeck (μV/K) | Power Factor (μW/mK$^2$) |
|---|---|---|---|
| Te | 2.3 ± 0.2 | 400 ± 10 | 36 ± 3 |
| Te/6PTTP6 | 2.2 ± 0.2 | 457 ± 6 | 45 ± 4 |
| Te/pentacene | 2.7 ± 0.4 | 468 ± 9 | 58 ± 6 |
| 6PTTP6 | < 0.01 | ~ 35 | 1x10$^{-6}$ |

## References


1. W. C. Cooper, in *Tellurium*, (Ed: W.C. Cooper), Van Nostrand Reinhold Co., New York, **1971**.

2. M. J. Capers, M. White, *Thin Solid Films.* **1971**, 8, 353-357.

3. R. L. Petriz, *Phys. Rev.* **1958**, 110, 1254.

4. S. K. Ghosh, *J. Phys. Chem. Solids* **1960**, *19, 61-65*.

5. K. Okuyama, Y. Kumagai, *Jap. J. Appl. Phys.* **1973**, 12, 1884-1889.

6. A. De Vos, J. Aerts, *Thin Solid Films.* **1977**, 46, 223-228.

7. M. Janda, A. Kubovy *Phys. Stat. Sol.* **1976**, 35, 391-402.

8. T. Hoffmann, B. Fideler, T. Kluck, J. Petermann, J. Martinez-Salazar, *Thin Solid Films.* **1994**, 245, 272-276.

9. T. Hoffmann, J. Martinez-Salazar, P. Herrero, J. Peterman, *Phys. Rev. B* **1997**, 55, 1858-1863.

10. H. Torii, M. Tsuji, Kawaguchi, *J. Mater. Research.* **1996**, 11, 970-980.

11. K. Okuyama, J. Tsuhako, Y. Kumagai **1973**, .

12. M. Janda, A. Kubovy *Phys. Stat. Sol.* **1976**, 35, 391-402.

13. T. Hoffmann, B. Fideler, T. Kluck, J. Petermann, J. Martinez-Salazar, *Thin Solid Films.* **1994**, 245, 272-276.

14. T. Hoffmann, J. Martinez-Salazar, P. Herrero, J. Peterman, *Phys. Rev. B.* **1997**, 55, 1858-1863.

15. H. Torii, M. Tsuji, Kawaguchi, *J. Mater. Research* **1996**, 11, 970-980.

16. A. De Vos, B. Hindryckx, *Proc. IEEE.* **1980**, 127, 42-44.

17. M. J. Capers, M. White, *Thin Solid Films* **1971**, 8, 353-357.

18. J. Huang, J. Sun, H. E. Katz, *Adv.Mater.* **2008**, 20, 2567-2572.

19. B. M. Dhar, G. S. Kini, G. Xia, B. J. Jung, N. Markovic, H. E. Katz, *PNAS* **2010**, 107, 3972-3976.

20. R. Capelli, S. Toffanin, G. Generali, H. Usta, A. Fachetti, M. Muccini, *Nature Mater.* **2010**, 9, 496-503.

21. R.M. Ireland, T. Dawidczyk, P. Cottingham, T. McQueen, G. Johns, N. Markovic, L. Zhang, P. Gopalan and H. E. Katz. *ACS Applied Mater. Interf.* **2013**

22. Y.Y. Wang, K.F. Cai and X. Yao. *J.Nanopart.Research* **2012,** 14.

23. T.O. Poehler and H.E. Katz. *Energy Environ. Science* **2012**, 5, 8110.

**Self-Assembled Monolayers on Gate Dielectric**

Typical OFET test architecture—the organic semiconductor (OSC) film on 100-300 nm of $SiO_2$ deposited on a conductive Si gate with >100 μm spacing between source

and drain electrodes—requires tens of volts to achieve effective switching. In the last ten years, many groups have studied high–capacitance dielectric layers in order to decrease operating voltages and enable closer source-drain separations than are typical for Si-$SiO_2$ substrates[7]. They used very thin amorphous polymers[8], monolayer-treated[9-11] or polymer-treated inorganic dielectrics[12], polymer electrolyte dielectrics[13], and high-k inorganic dielectrics[14]. An ultimate solution would be to produce OFETs from single layers of molecules that include both a dielectric side chain and a conjugated subunit; this has been attempted previously,[15, 16] and we have recently reported the first demonstration of OSC molecular segments within a multilayer film contributing to gate capacitance, acting substantially as gate materials in series with very thin oxide films.

However, based on our previous observations, thin oxides grown from highly-doped wafers yield less-insulating dielectrics than do thicker or chemical vapor-deposited $SiO_2$. High gate leakage has a detrimental effect on transistor performance, resulting in high OFF currents, low ON/OFF ratios, and increased power consumption, all of which negate the potential advantages of low-power OSC-based electronics. As a result, reducing the gate leakage in thin bottom gate-top contact OFETs is a technological priority for the study and development of OSC-based devices.

Recently the first investigation of a SAM dipole as an electrostatic barrier to reduce leakage currents in organic field-effect transistors (OFETs) fabricated on a minimal ~10 nm $SiO_2$ dielectric was reported.[17] More recently, the electric field associated with 1H,1H,2H,2H-perfluoro-octylsilyl (FOTS) dipolar chains affixed to the oxide surface gave an order of magnitude decrease in gate leakage current and a two order-of magnitude increase in on/off ratio for a synthesized naphthalenetetracarboxylic

diimide (NTCDI) transistor.[18] The surface potential conferred by the silane was directly measured using scanning Kelvin probe microscopy, and was of the correct sign and reasonable magnitude in light of the device measurements. This is the first time a connection between the OFET current-voltage relationships and surface potential values at the dielectric surface have been made. Our results highlight the potential of dipolar SAMs as performance-enhancing layers for marginal quality dielectrics, broadening the material spectrum for low power, ultrathin organic electronics. While other examples of SAMs used to shift OFET threshold voltages ($V_T$) have been reported by us and others[19-21], this is the first study of a SAM dipole being used specifically to lower gate leakage current. An explicit contribution of the SAM dipole field to the lowering of this current is demonstrated.

SAMs have potential for shifting of the $V_T$ in OFETs by tuning the accessibility of charges into layers near the semiconductor/dielectric interface,[1,2] and for fabricating unipolar inverters from 6PTTP6.[3] Here, we report the application of an alkyl molecule with an amine head group, APTS, a fluorinated alkyl chain, FOTS, and a dye molecule with much greater dipolar moment, DR19. X-Ray Photoelectron Spectroscopy was employed to confirm presence of these monolayers on oxide substrates (**Figure 13**). The range of chemical moites allows us to decouple the effects of a fluorinated surface, and gage the effectiveness of SAMs with different polarities to tune behavior of Te and hybrid devices.

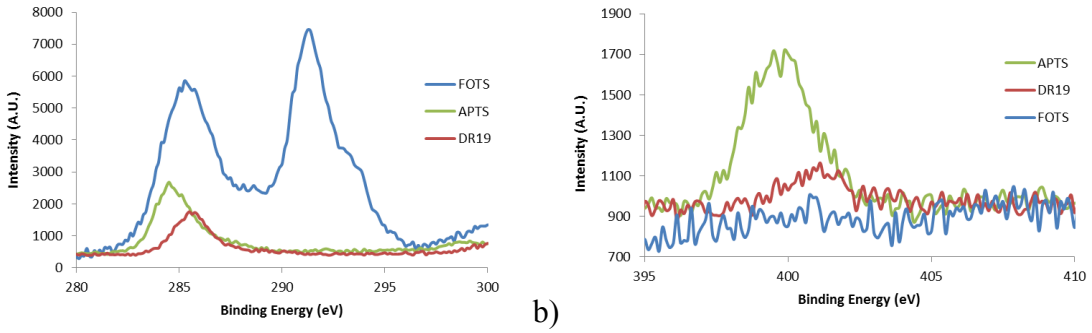


**Figure 13.** X-ray Photoelectron Spectra of substrates modified with SAMs. a) Carbon 1s spectra. APTS samples show the peak at 284.5, corresponding to the $CH_2$ bond. FOTS samples show a peak at 291 eV with shoulder at 293 eV, corresponding to $CF_2$ and $CF_3$ bonds. b) Nitrogen 1s spectra. APTS shows peak for $NH_2$ bond and DR19 with some $NO_2$ bonds.

Regarding morphology of tellurium when deposited onto molecular monolayers, it can display mostly anisotropic rod-like structures (**Figure 14**). Depositing Te/6PTTP6 onto SAM modified oxides at room temperature gave pronounced rod-like grains, resembling peapods on APTS, short fibers on FOTS, and rods on DR19. These morphologies are uniquely achieved at room temperature by using 6PTTP6 as an interlayer.

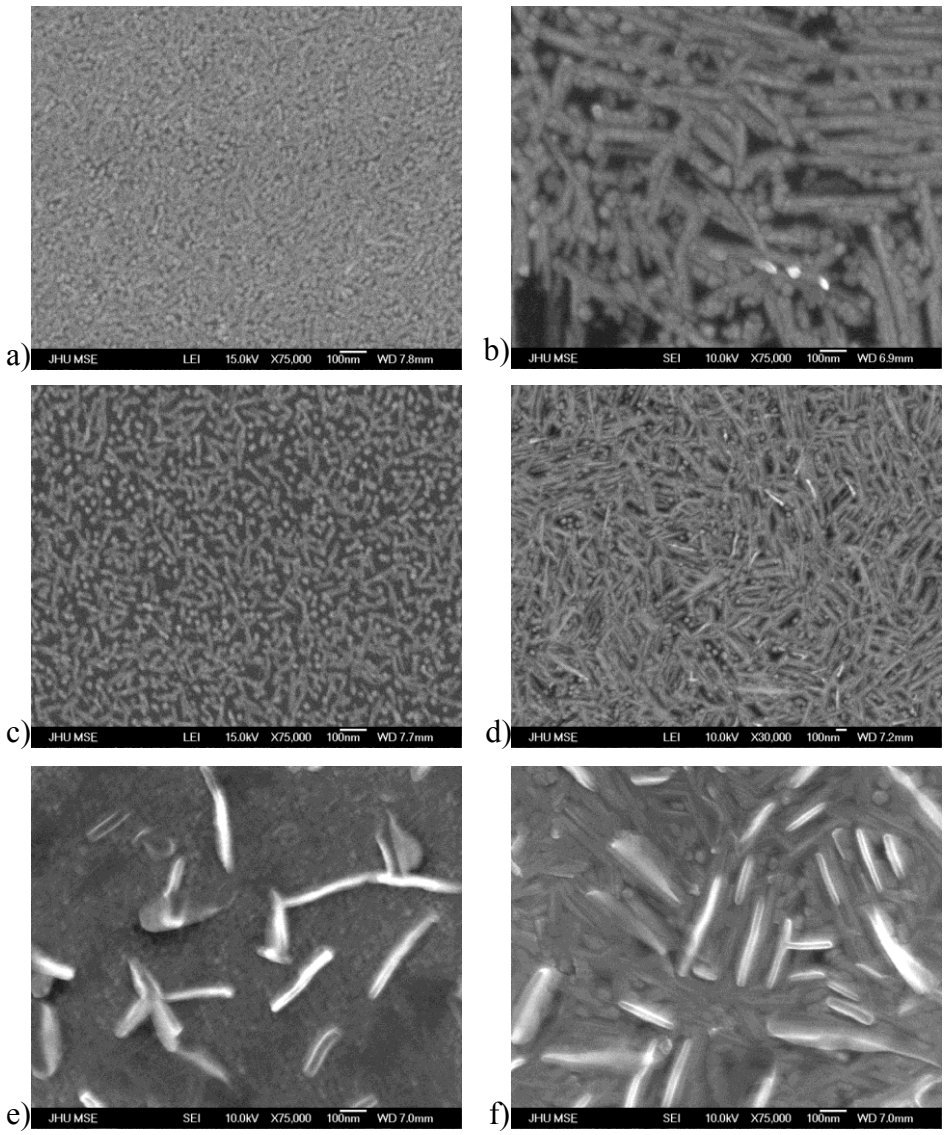


**Figure 14.** a) SEM micrograph of Te morphology on APTS/$SiO_2$ substrates b) Te/6PTTP6 on APTS/$SiO_2$ substrates c) Te on FOTS/$SiO_2$ d) Te/6PTTP6 on FOTS/$SiO_2$ e) Te on DR19/$SiO_2$ substrates and f) Te/6PTTP6 on DR19/$SiO_2$ substrates, all done at room temperature.

We observe that relative to Te on bare oxide, Te deposited onto APTS shows no field-effect, which is likely due to charge trapping at the amine interface. The

performance for Te on FOTS was degraded although field-effect was observed, probably due to poor morphology and incomplete coverage by Te. On the other hand, the mobility of Te/6PTTP6 is increased utilizing FOTS or DR19, which outperform both Te and Te/6PTTP6 on bare oxide at room temperature. This may be explained by enlarged grains and partial coalescence.

6PTTP6 OFETs utilizing DR19 showed reduction in current output and $V_T$ shift to higher negative voltages. Significantly, DR19 treatment was the best route towards accumulation mode Te devices with on/off ratios greater than $10^3$, but only for substrates heated to 55 °C during deposition. **Figure 15** shows the output curves, which have clear saturation for 0 to -20 $V_G$, and transfer curves ($V_T$ of -10 V), but mobility decreased three orders of magnitude relative to Te on bare oxide (Table 2). It is unknown whether the large $V_T$ shift for Te is due to the static dipole moment of DR19 monolayers, or the large amount of hole traps created by DR19. The decrease in current with increasingly negative $V_D$ indicates that hole-trapping occurs at the Te/DR19 interface. Under constant $V_G$, the mobility for Te on DR19 is lower than 6PTTP6 OFETs. Pulsing $V_G$ at I kHz resulted in higher mobility and steady-current after saturation because trapping at the interface was avoided. Pulsing doubled the mobility, consistent with charges not equilibrating with traps on the 1 kHz time scale, while the accumulation-only nature of the device was maintained. Thus, like in the above bilayer examples, pulsing placed charges preferentially in regions with higher mobility. In the DR19 case, the effect was from the more conventional increase in output current of a better behaved transistor, rather than simply extending the range over which current was modulated in depletion

mode. These devices are important because they show Te, as-deposited, with current modulation above $10^3$ orders of magnitude.

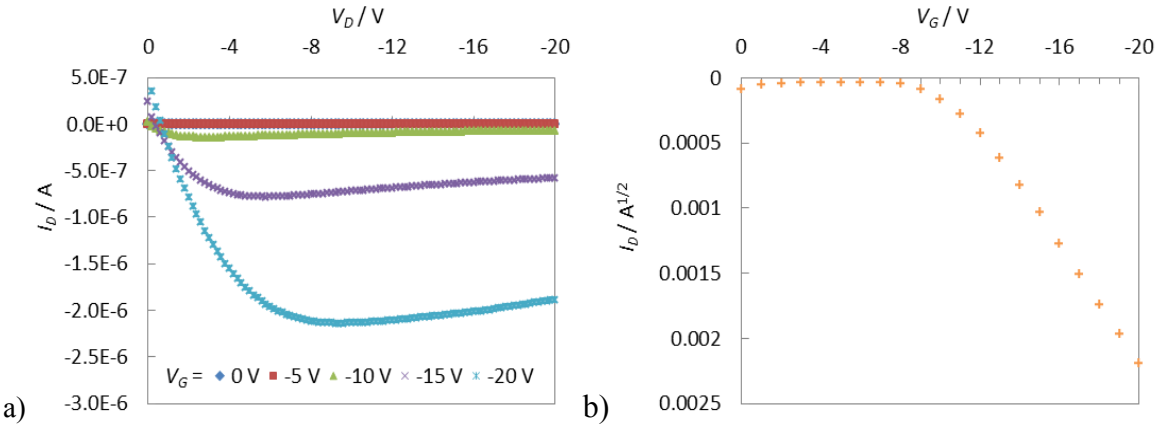


**Figure 15.** a) $I_D$ vs. $V_D$ (static $V_G$) plot for Te deposited on DR19/$SiO_2$ at room temperature with top contact Au electrodes; W/L is 80 b) $I_D^{1/2}$ vs. $V_G$ plot

## References


1. B. Crone, A. Dodabalapur, Y. Y. Lin, R. W. Filas, Z. Bao, A. LaDuca, R. Sarpeshkar, H. E. Katz, W. Li, *Nature* **2000**, 403, 521-523.

2. G. H. Gelinck, H. E. A. Huitema, E. Van Veenendaal, E. Cantatore, L. Schrijnemakers, J. Van der Putten, T. C. T. Geuns, M. Beenhakkers, J. B. Giesbers, B. H. Huisman, E. J. Meijer, E. M. Benito, F. J. Touwslager, A. W. Marsman, B. J. E. Van Rens, D. M. De Leeuw, *Nat. Mater.* **2004**, 3, 106-110.

3. V. Subramanian, J. M. J. Frechet, P. C. Chang, D. C. Huang, J. B. Lee, S. E. Molesa, A. R. Murphy, D. R. Redinger, *Proc. IEEE* **2005**, 93, 1330-1338.

4. K. Myny, S. Steudel, S. Smout, P. Vicca, F. Furthner, B. van der Putten, A. K. Tripathi, G. H. Gelinck, J. Genoe, W. Dehaene, P. Heremans, *Org. Elec.* **2010**, 11, 1176-1179.

5. T. Someya, T. Sekitani, S. Iba, Y. Kato, H. Kawaguchi, T. Sakurai, *Proc. Natl. Acad. Sci. USA* **2004**, 101, 9966-9970.

6. L. Torsi, G. M. Farinola, F. Marinelli, M. C. Tanese, O. H. Omar, L. Valli, F. Babudri, F. Palmisano, P. G. Zambonin, F. Naso, *Nat. Mater.* **2008**, 7, 412-417.

7. R. P. Ortiz, A. Facchetti, T. J. Marks, *Chem. Rev.* **2010**, 110, 205-239.

8. L. Wang, M. H. Yoon, G. Lu, Y. Yang, A. Facchetti, T. J. Marks, *Nat. Mater.* **2006**, 5, 893-900.

9. O. Acton, G. Ting, H. Ma, J. W. Ka, H. L. Yip, N. M. Tucker, A. K. Y. Jen, *Adv. Mater.* **2008**, 20, 3697-3701.

10. M. Halik, H. Klauk, U. Zschieschang, G. Schmid, C. Dehm, M. Schutz, S. Maisch, F. Effenberger, M. Brunnbauer, F. Stellacci, *Nature* **2004**, 431, 963-966.

11. H. Klauk, U. Zschieschang, J. Pflaum, M. Halik, *Nature* **2007**, 445, 745-748.

12. L. A. Majewski, R. Schroeder, M. Grell, *Adv. Mater.* **2005**, 17, 192-196.

13. M. J. Panzer, C. D. Frisbie, *J. Am. Chem. Soc.* **2005**, 127, 6960-6961.

14. B. N. Pal, B. M. Dhar, K. C. See, H. E. Katz, *Nat. Mater.* **2009**, 8, 898-903.

15. S. G. J. Mathijssen, E. C. P. Smits, P. A. van Hal, H. J. Wondergem, S. A. Ponomarenko, A. Moser, R. Resel, P. A. Bobbert, M. Kemerink, R. A. J. Janssen, D. M. de Leeuw, *Nature Nanotechnology* **2009**, 4, 674-680.

16. M. Mottaghi, P. Lang, F. Rodriguez, A. Rumyantseva, A. Yassar, G. Horowitz, S. Lenfant, D. Tondelier, D. Vuillaume, *Adv. Funct. Mater.* **2007**, 17, 597-604.

17. J. Huang, J. Sun, H. E. Katz, *Adv. Mater.* **2008**, 20, 2567-2572.

18. J. F. Martínez Hardigree, T. J. Dawidczyk, R. M. Ireland, G. L. Johns, B.J. Jung, M. Nyman, R. Osterbacka, N. Marković, and H. E. Katz, *ACS Appl. Mater. Interf.* **2013**, 5, 7025-7032.

19. K. P. Pernstich, S. Haas, D. Oberhoff, C. Goldmann, D. J. Gundlach, B. Batlogg, A. N. Rashid,G. Schitter, *J. App. Phys.* **2004**, 96, 6431-6438.

20. C. Huang, H. E. Katz, J. E. West, *Langmuir* **2007**, 23, 13223-13231.

21. N. Bjorklund, F. S. Pettersson, D. Tobjork, R. Osterbacka, *Synth. Met.* **2011**, 161, 743-747.

**Picosecond Laser Direct-Write Patterning of FET Arrays**

Furthermore, we used a solid-state picosecond laser for patterning the semiconductor thin-films that completely cover a substrate and utilize an array of top-contact electrodes.[1a] Isolating circuit components from the remaining film is essential in order to reduce parasitic capacitances and unwanted current pathways, for both general device performance and enabling key scientific observations. We investigated FETs which are comprised of p-channel tellurium and organic semiconductor molecules sequentially vapor-deposited onto $Si/SiO_2$ substrates. To determine effects of laser-isolation on FET performance we analyzed the steady-state electronic behavior (field-effect mobility, on/off current ratio, and gate currents) before and after patterning.

A solid-state picosecond laser is used to ablate semiconductor thin films in spatially localized areas, which is often called laser direct-writing (LDW), providing an alternative to device isolation strategies based on chemical or ion etching techniques.

Field-effect transistors (FET) of emerging organic and inorganic materials often utilize continuous semiconductor film and an array of top-contact electrodes. Electrically isolating individual FET components from other circuit elements is essential in order to reduce parasitic capacitances and unwanted current pathways, in order both to improve device performance and to enable the observation of new or enhanced physical phenomena. We pattern FET arrays with ultrafast pulse duration (1.5 ps) and low fluence (0.09 J $cm^{-2}$) optical pulses using the fundamental wavelength (1030 nm) of an Yb-YAG laser. We investigate two representative semiconductor materials. First, zinc oxide (ZnO) is deposited onto $Si/SiO_2$ substrates by sol-gel methods and used to create n-channel FETs with aluminum top electrodes. Isolation of individual FETs enables the clear observation of photomodulation of the FET device parameters via photoinduced electron donation from an adsorbed chromophore. The second system comprises thin-film bilayers of tellurium and organic semiconductor molecules sequentially vapor-deposited onto $Si/SiO_2$ substrates, with gold electrodes deposited last. Charge carrier mobility is at maintained for devices isolated by picosecond lasers, but leakage currents through the FET dielectric are drastically reduced.

Other effective strategies for limiting gate leakage must do so without modifying the interface chemical state of the material. Patterning semiconductor films is difficult using solution-based or mechanical methods without degrading the active materials and interfaces. LDW is thus particularly valuable for patterning devices while leaving the surface chemistry unchanged for the preservation of device performance, and for the attachment of functional molecules.

Optical pulses with picosecond durations enable high peak powers on the order of 10 MW to be produced with only a few watts of average optical power. Focused radiation can have intensities reaching several TW $cm^{-2}$, which permits direct machining of temperature-sensitive, brittle and soft materials without heating. In addition to materials that have fundamental optical bandgaps with energies lower than the photon energies, materials that are transparent at the laser wavelength can be machined via non-linear absorption. Previous applications of picosecond lasers in micromachining are in medical technology, anti-icing thin-films, optical filters, and circuit components.[2-9] Engelhardt , for example, investigated the fundamental processing properties of picosecond laser radiation on stainless steel, alumina, poly(methyl methacrylate), and quartz glass.[10] All the materials they investigated could be machined for practical application provided the laser fluence and peak powers were above the ablation threshold of the material, while maintaining temperatures below those that would result in thermally driven compositional or microstructural changes.

The physics of LDW allow it to be applied to semiconductor materials that require or benefit greatly from 'dry' post-processing methods, due to etching sensitivity or etch resistance. Micro-processing via laser allows us to fabricate semiconductor films under ideal conditions and then pattern a large area, which otherwise would require multiple invasive and complicated steps. We investigate two representative systems, including ZnO prepared as a standard transistor semiconductor and in a photomodulatable bilayer with a rhenium bipyridine (Re1c) chromophore, and thin-film bilayers of tellurium (Te) above OSCs.

Besides technical processing advantages, the laser isolation allows the confirmation of key scientific observations otherwise masked (or diminished) by leakage current, including the ZnO photomodulation and the effects of Te-OSC interfacial polarization. The semiconductor thin-films for this study were deposited on $Si/SiO_2$ substrates and subsequently optically patterned using the fundamental wavelength (1030 nm) of a solid-state picosecond laser (Yb-YAG, Hamamatsu Photonics). Detailed experimental conditions for the optical patterning are given in the Methods section.

LDW methods are extremely reproducible, and negligible variation in microstructural (i.e. trench depth, line-edge roughness) or FET parameters (i.e. field-effect μ) was observed between samples. Gate leakage is significantly reduced by LDW for the devices that we examined here. LDW is was shown to be an effective alternative for removing selected domains of both soft semiconductors and metal oxides of certain relative hardness compared to that of the dielectric, a useful alternative for materials that can be easily damaged by photolithography and chemical etchants. The measured photocurrent for ZnO devices functionalized with donor molecules was initially masked by significant gate leakage current, and that photocurrent is substantially enhanced by the donor as deposited. Isolation is critically important for devices where sensitivity and high signal-to-noise measurements of physical processes are required. Similarly, we emphasized that removing parasitic currents allows us to more clearly observe effects of the intrinsic dipole due to energy alignment of Te-OSC heterojunctions.

Preservation of lifetime characteristics, yield, and performance for devices using semiconductors other than Si will be driven by processing solutions which limit adverse thermal and chemical effects, while providing automation and high volume scaling.

Ultrafast pulses allow for non-invasive and selective material ablation, ensuring a clean and precise isolation technique which improves FET electrical performance and eases FET performance assessment, thus making LDW a viable patterning alternative.

**References**


1. R. M. Ireland, Y. Liu, J. Spalenka, S. Jaiswal, K. Fukumitsu, S. Oishi, H. Saito, M. Ryosuke, P. Evans, H. E. Katz, *Phys. Rev. Appl.* **2014**, 2, 044006.

2. P. Tormala, T. Pohjonen, P. Rokkanen, J. Eng. Med. **1998**, 212, 101.

3. D. Analdo del Cerro, G.R.B.E.R. Omer, A.J. Huis Veld, in *Proceedings of the 11th International Symposium on Laser Precision Microfabrication, Stuttgart,* **2010**.

4. M. D. Perry, B. C. Stuart, P. S. Banks, M. D. Feit, V. Yanovsky, A. M. Rubenchik, J. Appl. Phys. **1999**, 85, 6803.

5. V. V. Rana Z. Zhang, in *Proceedings of the SPIE Conference on Solid State Lasers XVIII: Technology and Devices, San Jose,* ***2009***.

6. J. Kruger, M. Lenzner, S. Martin, M. Lenner, C. Spielmann, A. Fiedler, W. Kautek, *J. Appl. Surf. Sci*. **2003**, 208, 233.

7. F. Haase, E. G. Rojas, K. Bothe, R. Brendel, *Energy Procedia* **2011**, 8, 577.

8. R. Mandamparambil, H. Fledderus, G. Van Steenberge, A. Dietzel, *Optics Express* **2010**, 18, 7575.

9. J. Bonse, G. Mann, J. Kruger, M. Marcinkowski, M. Eberstein, *Thin Solid Films* **2013**, 542, 420.

10. U. Engelhardt, J. Hildenhagen, K. Dickmann, *Micro Mater. Proc.* **2011**, 5, 32.

**Electrostatic Gating by Corona Charging of Electret Polymer**

We performed another experiment, this time aiming to alter the internal potentials determining the voltage at which the field effect is lost. We took advantage of our already reported technique of applying static charge to a nonpolar polymer dielectric,[20,21] in this case polystyrene[23] (PS) to shift OFET $V_T$, a method particularly effective for a normally-off OSC such as 6PTTP6. We used a corona charging method to insert an additional internal layer filled with static charge, or a floating gate that is built into the device as a bias. We observed that the effective gate voltage range allowable for FET behavior could be shifted towards reasonable low-power voltages, while also broadening the output curves (in both Te and Te/OSC bilayers).

Atactic (alternating structure) polystyrene forms amorphous polymeric films. Te deposited onto uncharged PS behaved similar to Te on bare $SiO_2$, but gave more densely packed semispherical crystallites with smaller diameters, ~ 20 nm (**Figure 16a**). Te deposited on negatively charged PS (PS-50) had similar orientation and grain size as films on uncharged PS (not shown). On positively charged PS (PS+50), semispherical Te crystallites aggregate to form larger "popcorn" structures (**Figure 16b**).

For uncharged PS substrates, micrographs reveal distinct semispherical Te grains on 6PTTP6 islands (**Figure 16c**). When Te/6PTTP6 is deposited onto PS+50, however, Te crystallites form an anisotropic network of rods with aspect ratios of 2-4 (**Figure 16d**). Atomic force micrographs show that grain size and roughness are similar for 6PTTP6 deposited onto uncharged PS versus PS+50 (**Figure 17**). Our observations indicate that crystallization of Te is sensitive to surface charge in addition to surface roughness/structure. Significantly, the anisotropic rod structure obtained for Te/6PTTP6

has only been obtained previously for tellurium films deposited onto heated substrates, which we have uniquely obtained this structure at room temperature utilizing the 6PPTP6 bilayer in tandem with PS+50 modified substrates.

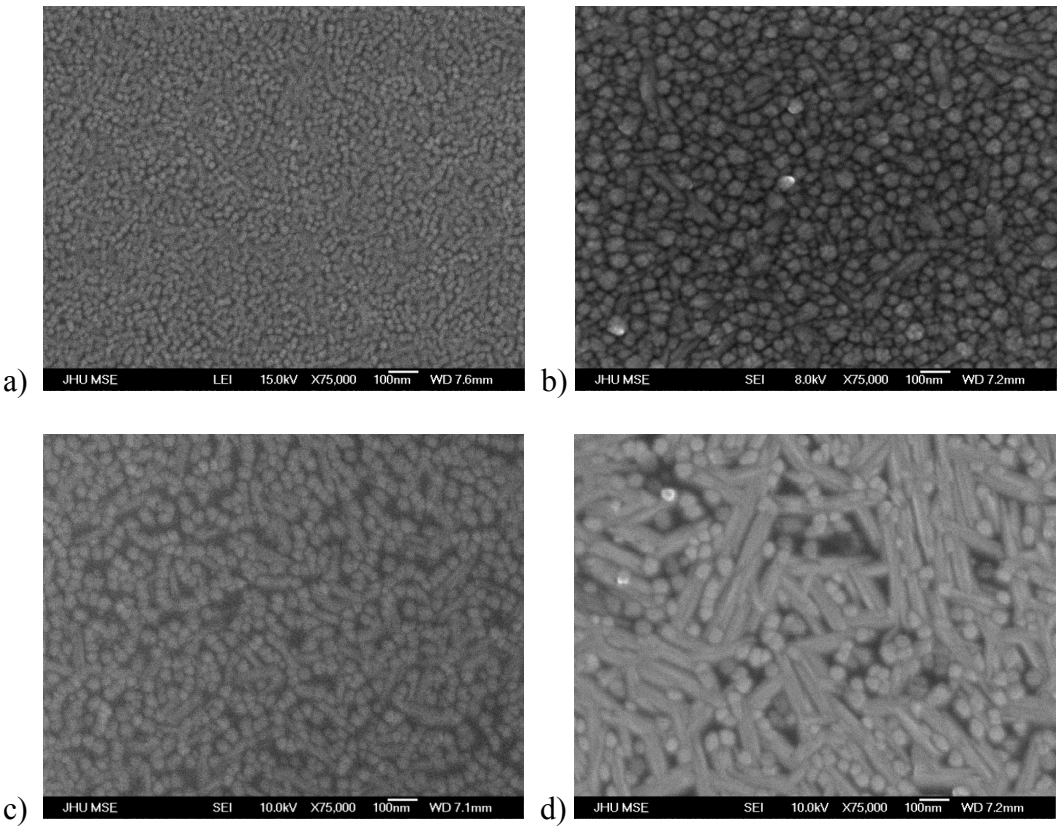


**Figure 16.** a) SEM micrograph of Te morphology on uncharged polystyrene at room temperature b) Te on polystyrene charged +50 V c) Te/6PTTP6 on uncharged polystyrene d) Te/6PTTP6 on polystyrene charged +50 V.

a)

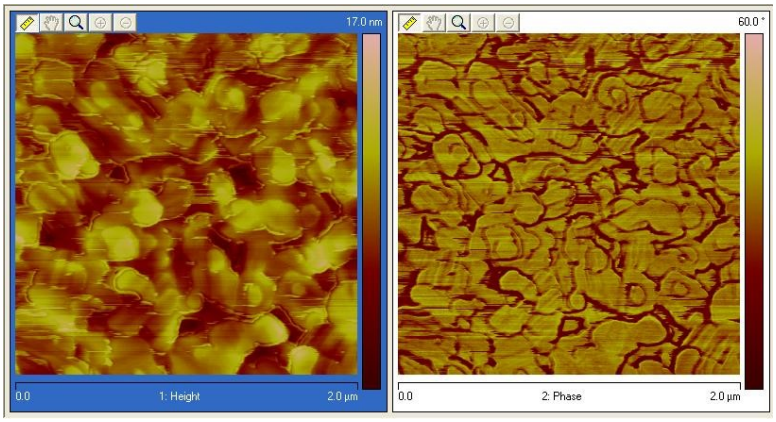


b)

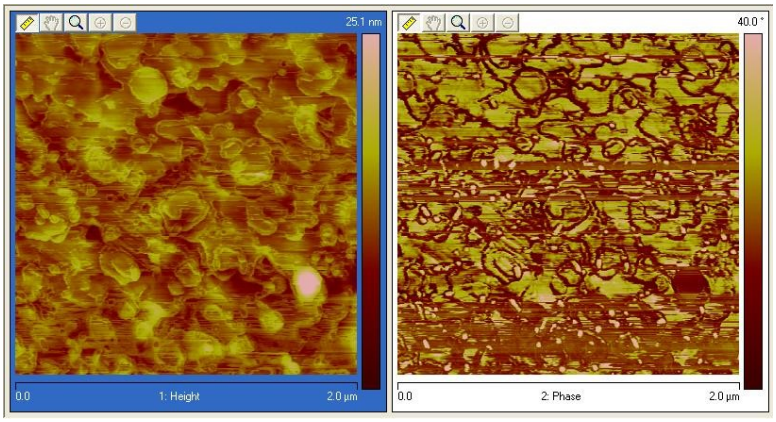


**Figure 17.** 6PTTP6 morphology on $SiO_2$/polystyrene dielectric. a) AFM image of 6PTTP6 morphology on uncharged polystyrene dielectric. b) 6PTTP6 morphology on polystyrene charged +50 V.

Embedding charges in polystyrene films produces an induced static-dipole at the dielectric interface, and has previously been reported for tuning the threshold voltage in OFETs.[1] **Figure 18** shows schematic charge distributions for the two Te bilayers and for Te/6PTTP6 on charged polystyrene, before application of $V_g$. For the bilayers, the charge distributions reflect the relative stability of holes in the materials as indicated by SKPM. As discussed above, holes are more easily driven into pentacene by a negative

gate voltage, lowering the mobility at a less negative $V_g$. For the charged system, the injected static charges are in the polystyrene and some of those static charges act as remote dopants for the Te layer as well, though we do not expect that charges in the polystyrene are themselves mobile. The static charges pose a barrier to driving positive charges into the 6PTTP6, increasing the $V_g$ range for useful field effect.

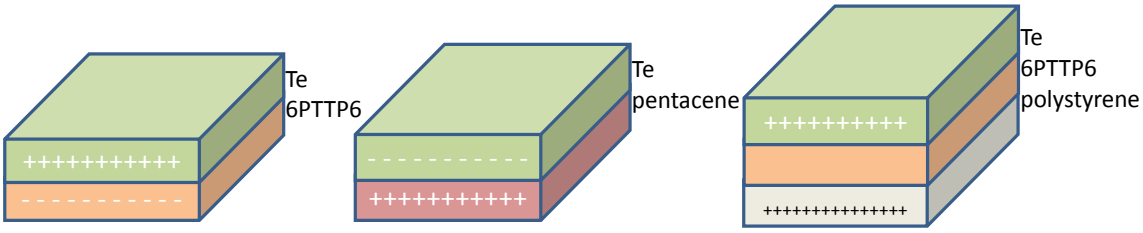


**Figure 18.** Schematic charge distributions for the two Te/OSC bilayers, and for Te/6PTTP6 on polystyrene charged with positive 50 V, before application of $V_g$.

**Figure 19** shows characteristics of OFETs with 6PTTP6 and Te FETs using PS gate dielectric interlayers, with and without prior static charging of +50 V. This charging polarity would be expected to result in FETs with the off state shifted further into the accumulation regime.[22] Indeed, this was observed for 6PTTP6 alone (**Figures 19a-b**), with maintenance of the expected mobility, correcting for the lowered gate capacitance. Surprisingly, this charging turned Te-containing FETs more "on", i.e. threshold voltage was shifted into depletion and output current was increased (**Figures 19c-f**). Furthermore, comparing to **Figure 2a**, the field effect of Te on 6PTTP6 extended farther into the accumulation regime with the polystyrene interlayer than without it, possibly reflecting the higher $V_d$ needed to create the same gate field with the PS present. Static

charging extends the field effect more significantly into accumulation, even though the charge density indicated by **Figure 19f** is also greater.

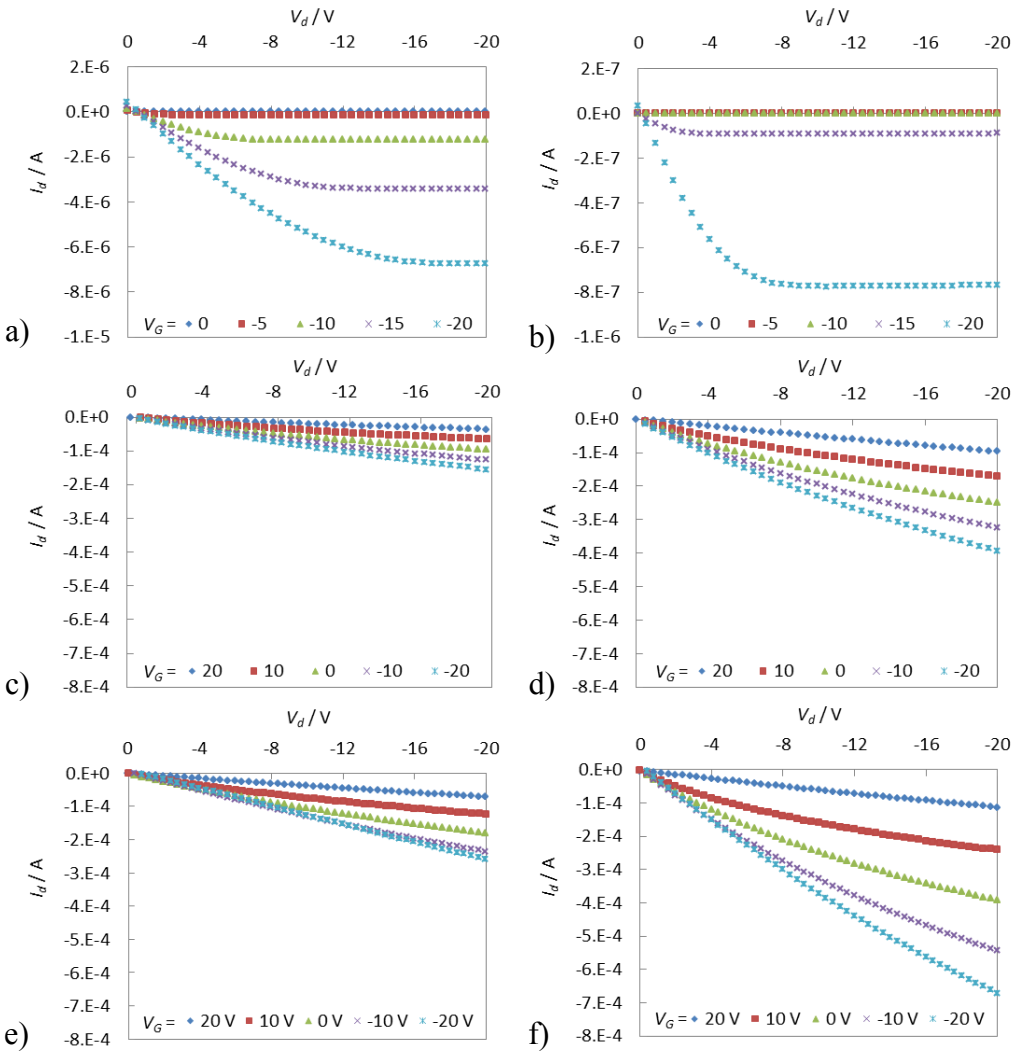


**Figure 19.** $I_d$ vs. $V_d$ plot for a) 6PTTP6 on PS/$SiO_2$ and b) PS+50/$SiO_2$. c) Te on PS/$SiO_2$ and d) PS+50/$SiO_2$. e) Te/6PTTP6 on PS/$SiO_2$ and f) PS+50/$SiO_2$.

Thus, the polystyrene layer and the static charging both decrease the effective gate field that drives holes from Te into the 6PTTP6. The resulting increase in $V_g$ range

showing field effect is evidence for our hypothesis that the loss of field effect in uncharged devices is due to charge becoming more distributed in the lower-μ layer at more negative $V_g$, and not because of the more negative $V_g$ eventually causing all hole-supporting sites in the Te to become filled. OFET performances for experiments on statically charged samples are summarized in the supporting information (**Table 3**). As was the case with Te on $SiO_2$, 1-kHz pulsing further spread the $I_d$-$V_d$ curves, increasing the apparent mobility and lowering $V_t$.

**Table 3.** Hybrid OFET Parameters and Performance with Charged Polystyrene

| Semiconductor Stack | Dielectric | $\mu_{meas}$ [$cm^2\ V^{-1}\ s^{-1}$] [a] | $V_T$ [V] [a] | On/Off | $N_s$ [b] |
|---|---|---|---|---|---|
| 6PTTP6 [c] | PS/$SiO_2$ | 0.038 ± 0.002 | -3.2 ± 0.071 | 23125 | 4 |
| | PS+50/$SiO_2$ [d] | 0.031 ± 0.003 | -24.5 ± 1.7 | 9075 ± | 4 |
| Te | PS/$SiO_2$ | 0.043 ± 0.003 | 47.2 ± 0.30 | 2.3 ± | 4 |
| | PS+50/$SiO_2$ | 0.383 ± 0.107 | 56.9 ± 0.45 | 2.5 ± | 4 |
| Te/ 6PTTP6 | PS/$SiO_2$ | 0.224 ± 0.026 | 43.9 ± 7.4 | 4.3 ± | 4 |
| | PS+50/$SiO_2$ | 0.593 ± 0.038 | 54.6 ± 6.7 | 4.6 ± | 12 |

[a] Mobility $\mu_{meas}$, and $V_T$ values were extrapolated from $I_d^{1/2}$ vs. $V_g$ plots. W/L is 80. $V_g$ is pulsed at 1 kHz. [b] $N_s$ is number of samples corresponding to calculated values and standard deviations. [c] Devices measured in the accumulation regime ($V_g$ of 0 to -20 V). [d] Devices measured in the high accumulation regime ($V_g$ of 0 to -50 V). All other devices were measured in the p-channel depletion regime ($V_g$ of 20 to 0 V).

Charged polystyrene experiments prove that the observed saturation collapse in Te/6PTTP6 devices is influenced by accessibility of the OSC. 6PTTP6 deposited on

uncharged PS behaved as normal p-channel devices. Taking into account the lowered capacitance of the modified dielectric bilayer, field-effect mobility is maintained for 6PTTP6 OFETs. When PS is charged positively, 6PTTP6 becomes harder to turn on because the high concentration of positive charges opposes the gate voltage in accumulation mode. The $V_T$ shifts from -5 V on bare oxide to -20 V with +50 V stored in PS. The effect is consistent with prior work.[1]

Embedding the polystyrene with +50 V did not make the Te device more difficult to turn On. Instead, the device became more difficult to turn Off. The induced dipole in PS does not seem to oppose the formation of a charge channel in Te field-effect devices. Although charged polystyrene did not help turn Off the Te or the 6PTTP6 hybrid devices, the built-in potential in PS still makes it much more difficult to pack holes into 6PTTP6 via gate modulation. This is observed as a negative $V_G$ shift for the output current saturation collapse in p-OSC/Te devices. The transition still occurs, but is requires more negative gate voltages, closer to -20 $V_G$ (**Figure 20**). The shift in $V_G$ dependence between uncharged PS and PS+50 hybrids further demonstrates that FET saturation collapse occurs as a result of the OSC filling with charges.

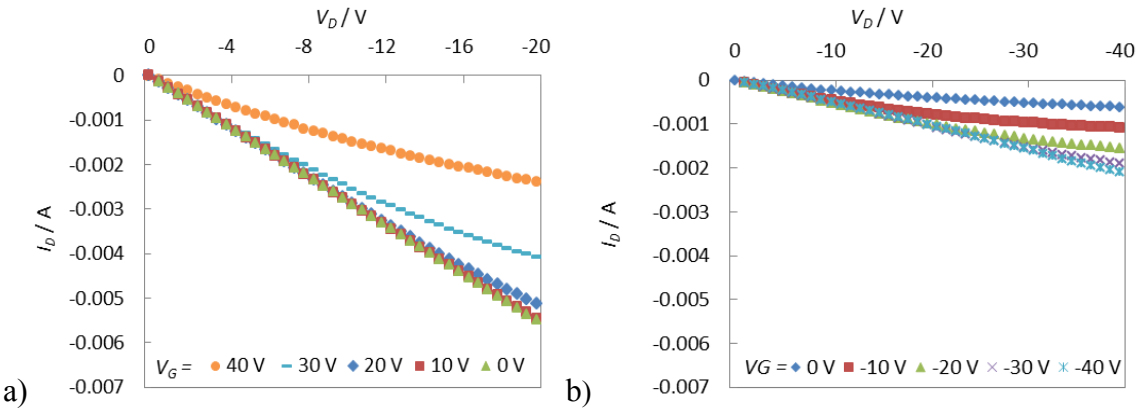


**Figure 20.** a) $I_D$ vs. $V_D$ plot for tellurium on pentacene/$SiO_2$ (collapse at $20V_G$). b) $I_D$ vs. $V_D$ plot for Te/6PTTP6 on PS+50/$SiO_2$ (collapse at $-20V_G$). W/L is 80.

## References


1. B. M. Dhar, R. Ozgun, T. J. Dawidcyk, A. G. Andreou, H. E. Katz, *Mater. Science Eng. R.* **2011**, 72, 49-80.

2. J. Huang, J. Sun, H. E. Katz, *Adv. Mater.* **2008**, 20, 2567-2572.

3. J. Huang, H. E. Katz, J. E. West, *Langmuir* **2007**, 23, 13223-13231.

4. R. Capelli, S. Toffanin, G. Generali, H. Usta, A. Fachetti, M. Muccini, *Nature Mater.* **2010**, 9, 496-503.

# CHAPTER 3

# Topological Insulator Application

## Introduction

Topological insulators (TIs) are an exotic new material with relatively novel physical properties. Particularly, they are considered to be insulators in the bulk of the material, but support helical metallic surface states on their boundaries or surfaces.[1,2] Unlike conventional surface states, these do not depend of the details of surface termination or environment, and would exist even if the bulk were insulating. They are determined by the stable termination at surfaces of quantum mechanical functions. Examples of such materials are $Bi_{1-x}Sb_x$, $Bi_2Se_3$, $Bi_2Te_3$, and $TlBiSe_2$. Angle Resolved PhotoElectron Spectroscopy (ARPES) has confirmed the existence of the surface states, and further development of the field hinges on controlling bulk electronic properties sufficiently to allow the surface properties to become dominant. In this regard, a spin-polarized current may be easily induced on the surface, which makes TIs ideal platforms for future low-dissipation spintronics applications.[3] Spin plasmons generated in the topological surface states by patterning the samples may be used for the next generation of plasmonic devices because spin-momentum locking reduces the energy dissipation.[4] Topological surface states display many interesting fundamental physics phenomena, however, including a topological magneto-electric effect, quantized Faraday rotation and axion electrodynamics.[5-7] Physicists are especially interested in Majorana fermions, which may be realized in the vortex core through a proximity effect between

superconductors and intrinsic Tis,[8] and their non-abelian statistical nature may serve as a foundation for fault-tolerant quantum computers in the near future.[9]

Unfortunately, most TIs are either doped in the bulk or quickly lose their intrinsic properties by exposure to atmosphere.[10-12] Chemical dedoping has been shown to be one effective method in reducing the carrier density. However, disorder introduced by dedoping tends to pin impurity states at the chemical potential and scatter charges, which can significantly decrease the carrier mobility.[13-15] Furthermore, these chemically compensated TIs still suffer from strong aging effects in the atmosphere.[12] Gating is an effective method to lower the chemical potential in the bulk gap while potentially also passivating the surface from oxidation,[16-18] however, for realistic applications, an external voltage source may not be convenient or cost-effective. An improved method to deplete the carrier density while keeping high mobility and preventing aging is needed to facilitate not only applications, but fundamental scientific studies of TIs.

Regarding the common topological insulator material $Bi_2Se_3$, recent investigations have explored the shifting of energy levels by surface transfer doping (a non-intrusive method of charge extraction, or dedoping) utilizing metal oxides such as ZnO or $MoO_3$,[19,20] or small-organic molecules such as F4TCNQ and TCNQ.[21] $MoO_3$ appears to be a popular candidate for p-type surface charge extraction of both organic[22,23] and inorganic[24-26] semiconductors due to high electron affinity and ease of processing by evaporation or from solution. Nevertheless, its relatively refractory nature makes it inconvenient for partial removal after charge extraction, which could allow for further study or processing, such as depositing ferromagnets leads for spintronic applications.[27]

All of the above phenomena can only be realized in intrinsic (i.e. bulk-insulating) TIs, of which $Bi_2Se_3$ is a particularly outstanding example. Reaching the intrinsic, or TI, regime depends crucially on positioning the electrochemical potential in the bulk bandgap. However an outstanding issue in this field is that all as-grown materials like $Bi_2Se_3$ typically have the chemical potential in the conduction band due to defect doping or band bending effects at surfaces, so their bulk properties are decidedly not insulating.[28-30] This includes the especially high quality molecular beam epitaxy (MBE)-grown $Bi_2Se_3$ used in our own work. Although MBE is the most precise method for fabricating high quality $Bi_2Se_3$, films prepared by this method generally have a high intrinsic n-type carrier concentration due to significant Se vacancies,[31] necessitating the depletion of negative carriers in order to observe and utilize intrinsic TI physics.

This chemical potential manipulation is typically achieved by means of a capacitively coupled gate electrode. For example, one may couple the gate electrode to the face of a two-dimensional inorganic sample via an ionic liquid.[32-38] This configuration, while indeed conveying a high capacitive field (up to 5 V across a molecular-scale distance, 10 MV/cm) to the sample, suffers from a number of problems, including chemical inhomogeneity at the inorganic surface (a source of hysteresis[39] and mobility-reducing scattering), limited control of parasitic capacitances and resistances, the possibility of electrochemistry at the inorganic sample surface, and an inability to confine the entire device structure to dimensions that would allow interference-free optical probing.

**References**

1. M. Z. Hasan, C. L. Kane, *Rev. Mod. Phys.* **2010**, 82, 3045.

2. X.L. Qi, S.C. Zhang, *Rev. Mod. Phys.* **2011**, 83, 1057.

3. D. Pesin, A.H. MacDonald *Nature Mater.* **2012**, 11, 409.

4. Y. Okada, V. Madhavan, *Nature Nanotechnology* **2013**, 8, 541.

5. X.L. Qi, T. L. Hughes, S.C. Zhang, *Phys. Rev. B* **2008**, 78,195424.

6. W.K. Tse, A. H. MacDonald, *Phys. Rev. Lett.* **2010**, 105, 057401.

7. R. Li, J. Wang, X.L. Qi, S.C. Zhang, *Nature Physics* **2010**, 6, 284.

8. L. Fu, C. L. Kane, *Phys. Rev. Lett.* **2008**, 100, 096407.

9. A.Y. Kitaev, *Annals Phys.* **2003**, 303, 2-30.

10. Y. Xia, D. Qian, D. Hsieh, L. Wray, A. Pal, H. Lin, A. Bansil, D. Grauer, Y. S. Hor, R. J. Cava, M. Z. Hasan, *Nature Physics* **2009**, 5, 398 ().

11. M. Bianchi, D. Guan, S. Bao, J. Mi, B. B. Iversen, P. D. C. King, P. Hofmann, *Nature Communications* **2010**, 1, 128.

12. M. Salehi, M. Brahlek, N. Koirala, J. Moon, L. Wu, N. P. Armitage, S. Oh, *APL Mater.* **2015**, *3*, 091101.

13. Y. S. Hor, A. Richardella, P. Roushan, Y. Xia, J. G. Checkelsky, A. Yazdani, M. Z. Hasan, N. P. Ong, R. J. Cava, *Phys. Rev. B* **2009**, *79*, 195208.

14. Z. Ren, A. A. Taskin, S. Sasaki, K. Segawa, Y. Ando, *Phys. Rev. B* **2010**, *82*, 241306.

15. J. Xiong, A. C. Petersen, D. Qu, Y. S. Hor, R. J. Cava, N. P. Ong, *Physica E: Low-dimensional Systems and Nanostructures* **2012**, *44*, 917-920.

16. Y. Xu, I. Miotkowski, C. Liu, J. Tian, H. Nam, N. Alidoust, J. Hu, C.K. Shih, M. Z. Hasan, Y. P. Chen, *Nature Physics* **2014**, 10, 956.

17. D. Kim, S. Cho, N. P. Butch, P., Syers, K. Kirshenbaum, S. Adam, J. Paglione, M. S. Fuhrer, *Nature Physics* **2012**, *8*, 459-463.

18. R. Yoshimi, A. Tsukazaki, Y. Kozuka, J. Falson, K. S. Takahashi, J. G. Checkelsky, N. Nagaosa, M. Kawasaki, Y. Tokura, *Nature Communications* **2015**, 6, 6627.

19. S. S. Hong, J. J. Cha, D. Kong, Y. Cui, *Nature Communications* **2012**, 3, 757.

20. M. T. Edmonds, J. T. Hellerstedt, A. Tadich, A. Schenk, K. M. O'Donnell, J. Tosado, N. P. Butch, P. Syers, J. Paglione, M. S. Fuher, *ACS Nano* **2014**, 8, 6400-6406.

21. Y. Tanabe, K. K. Huynuh, R. Nouchi, S. Heguri, G. Mu, J. Xu, H. Shimotani, K. Tanigaki,

22. M. Kroger, S. Hamwi, J. Meyer, T. Riedl, W. Kowalsky A. Kahn, *Appl. Phys. Lett.* **2009**, 95, 123301.

23. J. Meyer, S. Hamwi, M. Kroger, W. Kowalsky, T. Riedl, A. Kahn, *Adv. Mater.* **2012**, 24, 5408-5427.

24. B. He, T.W. Ng, M.F. Lo, C.S. Lee, W. Zhang, *ACS Appl. Mater. Interfaces* **2015**, 7, 9851-9857.

25. M. T. Edmonds, J. T. Hellerstedt, A. Tadich, A. Schenk, K. M. O'Donnell, J. Tosado, N. P. Butch, P. Syers, J. Paglione, M. S. Fuher, *ACS Nano* **2014**, 8, 6400-6406.

26. G. D. Yuan, T. W. Ng, Y. B. Zhou, F. Wang, W. J. Zhang, Y. B. Tang, H. B. Wang, L. B. Luo, P. F. Wang, I. Bello, C. S. Lee, S. T. Lee, *Appl. Pys. Lett.* **2010**, 97, 153126.

27. M. Veldhorst, M. Snelder, M. Hoek, T. Gang, V. K. Guduru, X. L. Wang, U. Zeitler, *Nature Mater.* **2012**, 11, 417-421.

28. J. G. Checkelsky, Y. S. Hor, M. H. Liu, D. X. Qu, R. J. Cava, N. P. Ong, *Phys. Rev. Lett.* **2009**, 103.

29. Y. S. Hor, A. Richardella, P. Roushan, Y. Xia, J. G. Checkelsky, A. Yazdani, M. Z. Hasan, N. P. Ong, R. J. Cava, *Phys. Rev. B* **2009**, 79.

30. J. G. Analytis, J. H. Chu, Y. L. Chen, F. Corredor, R. D. McDonald, Z. X. Shen, I. R. Fisher, *Phys. Rev. B* **2010**, 81.

31. S. Jakobs, A. Narayan, B. Stadtmüller, A. Droghetti, I. Rungger, Y. S. Hor, *Nano Lett.* **2015**, 15, 6022-6029.

32. K. Segawa, Z. Ren, S. Sasaki, T. Tsuda, S. Kuwabata, Y. Ando, *Phys. Rev. B* **2012**, 86.

33. S. Shimizu, R. Yoshimi, T. Hatano, K. S. Takahashi, A. Tsukazaki, M. Kawasaki, Y. Iwasa, Y. Tokura, *Phys. Rev. B* **2012**, 86.

34. H. T. Yuan, H. W. Liu, H. Shimotani, H. Guo, M. W. Chen, Q. K. Xue, Y. Iwasa, *Nano Lett.* **2011**, 11, 2601-2605.

35. Y. J. Zhang, J. T. Ye, Y. Matsuhashi, Y. Iwasa, *Nano Lett.* **2012**, 12, 1136-1140;

36. J. T. Ye, S. Inoue, K. Kobayashi, Y. Kasahara, H. T. Yuan, H. Shimotani, Y. Iwasa, *Nature Mater.* **2010**, *9*, 125-128.

37. J. Son, K. Banerjee, M. Brahlek, N. Koirala, S. K. Lee, J. H. Ahn, S. Oh, H. Yang, *Appl. Phys. Lett.* **2013**, 103.

38. J. Xiong, Y. Khoo, S. Jia, R. J. Cava, N. P. Ong, *Phys. Rev. B* **2013**, 88.

39. D. J. Late, B. Liu, H. Matte, V. P. Dravid, C. N. R. Rao, *ACS Nano* **2012**, 6, 5635-5641.

**Interfacial Fields in Bismuth Selenide-Organic Hybrids**

$Bi_2Se_3$ is not trivial to create in the laboratory. The best films (highest quality, least defects) of $Bi_2Se_3$ are currently made by depositing under high vacuum by molecular beam epitaxy. The reason for this is that defects, such as Se vacancies, are sources of electrons in the material and make the bulk material conductive. In order to have a topological insulator it is necessary to lower the carrier concentration since the chemical potential, or Fermi level, resides in the conduction band of as-made films, but should be inside the band gap. Oxidation or formation of defects in the $Bi_2Se_3$ is not desirable and does occur naturally in air, so we must take precautions to avoid it when possible, like capping with PMMA protective layer or storing in dry vacuum.

The $Bi_2Se_3$ films are currently best grown by molecular beam epitaxy, from 8 to 20 nm.[1] We have recently deposited a handful of different small organic molecules onto $Bi_2Se_3$ films in order to observe any shift in chemical potential. We test the efficacy of shifting the $Bi_2Se_3$ chemical potential by spectroscopic measurement. In this work, we demonstrate the ability to tailor/reduce the carrier concentration of low-carrier-density $Bi_2Se_3$ films prepared by MBE by utilizing various OSC layers as oxidizing surface dedopants. We show the electronic accessibility of the particular OSCs, revealing that the Fermi level of $Bi_2Se_3$ is shifted towards the Dirac point by altering $Bi_2Se_3$ carrier concentration. For these purposes we chose 2,3,5,6-tetrafluoro-7,7,8,8,-tetracyanoquinodimethane (F4TCNQ) and tris(acetylacetonato)cobalt(III) ($Co(acac)_3$) due to their commercial availability, low toxicity, and stable oxidation potential.[2] **Figure 21** shows two real conductance plots measured by infrared spectroscopy for nominally 16 nm $Bi_2Se_3$ films with about 100 nm of overlying organic film. The total area under real

conductance is the so called spectral weight, which tells you information about carrier density and effective mass. Usually, lower spectral weight means lower carrier density, as seen in samples after F4TCNQ is deposited. Tetracene is an electronically neutral (wide-band gap) material, so we didn't see significant change in the real conductance, as expected.

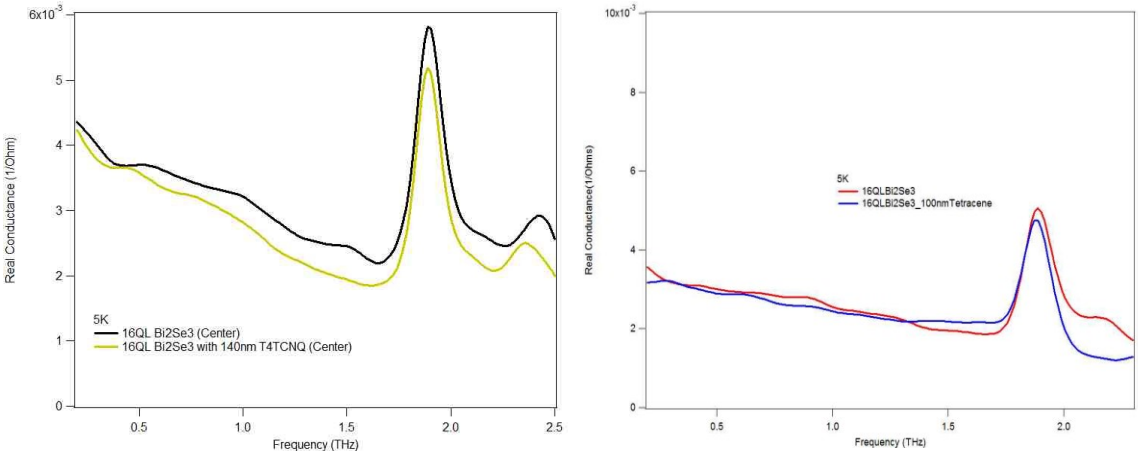


**Figure 21.** Real conductance plots for $Bi_2Se_3$ covered with F4TCNQ (left) and tetracene (right).

The low-carrier-density $Bi_2Se_3$ films used for this study were grown 16QL thick (1 quantum layer (QL) ≈ 1nm) on $(Bi_{1-x}In_x)_2Se_3$ buffer layers on sapphire substrates using a custom-designed molecular beam epitaxy (MBE) system at Rutgers University, and the details are published elsewhere.[3] DC transport, angle-resolved photoemission spectroscopy (ARPES) measurements and THz experiments of the as-prepared films have shown no signatures of bulk and trivial two-dimensional electron gas states.[3] To mitigate aging, $Bi_2Se_3$ samples were sealed in vacuum bags and sent to Johns Hopkins

University (JHU) overnight, and uncapped $Bi_2Se_3$ films were utilized for experiments without further cleaning. The overall exposure time in atmosphere is about 5 minutes after opening the vacuum bag and before loading into an optical cryostat for THz measurements. After finishing THz measurement on day 1, samples were kept in vacuum and were transported for charge extraction layer deposition. The transport time is about 10 minutes and the samples are exposure to atmosphere for maximum of 2 minutes before loading the samples into the evaporation system. OSC layers were deposited to 50 nm from powders held in alumina crucibles at a rate of 0.3 Å $s^{-1}$ in an Edwards thermal evaporation system using a base pressure around $3\times10^{-6}$ Torr. All deposition rates and nominal deposited thicknesses were monitored by a quartz crystal microbalance, and temperature was monitored by a thermocouple placed on the backside of substrates, although no increase in temperature was expected or observed. We immediately transported the samples back to the THz facility after OSC layer deposition.

Contact-free time-domain THz spectroscopy (TDTS) was performed in a transmission geometry utilizing a custom home-built THz spectrometer. In this technique an approximately single-cycle picosecond pulse of light is transmitted through the sample and the substrate, and then the complex transmission is obtained from the ratio of a Fourier transformed time-domain sample pulse over a Fourier transformed substrate pulse. By measuring both the magnitude and phase of the transmission, the inversion to conductance is done directly without need for Kramers-Kronig transformation. Non-destructive TDTS is an ideal tool to study the low frequency response of these materials, particularly for observing the metallic Drude response from topological surface states and

also observing an $E_{1u}$ infrared active phonon, and it can also directly measure the scattering rate.[1,4,5]

First we plot the THz conductance for bare $Bi_2Se_3$ (sample 1) at day 1, then with 50 nm F4TCNQ doping layer at day 2 and at day 120 in **Figure 22a-b**. Also we show the conductance for bare $Bi_2Se_3$ (sample 2) at day 1, then with 50 nm $Co(acac)_3$ at day 2 and day 120 in **Figure 22c-d**. The optical conductance can be well described by a single Drude term (a Lorentzian centered at ω = 0), a Drude-Lorentz term (which models the phonon) and a frequency independent real $\varepsilon_\infty$ contribution to the dielectric constant (that accounts for the effect of higher energy excitations on the low frequency physics).[1,4,5]

$$G(\omega) = \left[ -\frac{\omega_{pD}^2}{i\omega - \Gamma_D} - \frac{i\omega\omega_{pDL}^2}{\omega_{DL}^2 - \omega^2 - i\omega\Gamma_{DL}} - i(\epsilon_\infty - 1) \right] \epsilon_o d \qquad (4)$$

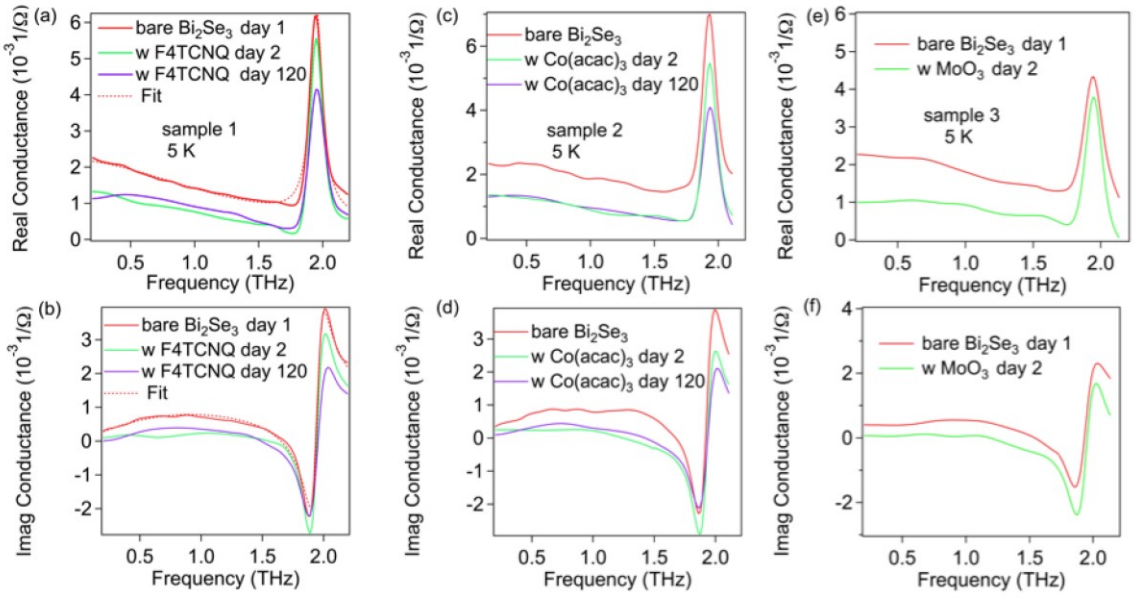


**Figure 22.** (a) Real and (b) imaginary conductance for bare 16QL $Bi_2Se_3$ (sample 1) at day 1, with 50 nm F4TCNQ doping layer at day 2 and with F4TCNQ at day 120 at 5 K.

(c) Real and (d) imaginary conductance for bare 16QL $Bi_2Se_3$ (sample 2) at day 1, with 50 nm $Co(acac)_3$ doping layer at day 2 and with $Co(acac)_3$ at day 120 at 5 K. (e) Real and (f) imaginary conductance for bare 16QL $Bi_2Se_3$ (sample 3) at day 1, with 50 nm $MoO_3$ doping layer at day 2 at 5 K.

In the above equation (eqn. 4) d is the film thickness, $\Gamma$'s are scattering rates and $\omega_p$'s are plasma frequencies. We include only a single Drude term because no bulk and trivial 2D electron gas states from band bending were found in these samples, and because top and bottom surface states are believed to have similar carrier density and mobility.[3] We can obtain the Drude spectral weight $\omega_{pD}^2$ and scattering rate $\Gamma_D$ from the fitting. Scattering rate is the half-maximum width of the Drude conductance, and the Drude spectral weight (squared) is a measure of carrier density. The integrated Drude spectral weight is proportional to the area under the real part of Drude conductance $G_{D1}$, giving the ratio of total sheet carrier density over transport effective mass.

We observe that electron-attracting OSC layers F4TCNQ and $Co(acac)_3$ both effectively lower the spectral weight of the Drude response, indicating that the surface states are depleted. The Drude conductance retains a similar scattering rate, which indicates the organic thin film layers are homogenous and don't induce new impurity scattering. When samples were kept in a desiccator for the next four months and then re-measured by the THz spectrometer, no significant increase of spectral weight or increase of scattering were found in the THz conductance. Therefore OSC layers decrease the carrier density, but they also stabilize the sample in the topologically intrinsic regime.

We performed DC transport on sample 1 with F4TCNQ and sample 2 with $Co(acac)_3$ at day 30. Longitudinal resistance as a function of temperature along with standard Hall effect measurements (at 5 K and room temperature) were carried out with a van der Pauw geometry in a magnetic field up to 0.6 T. The carrier density was extracted from the standard $R_{xy} = B/(en_{Hall})$ formula, and values for mobility were calculated based on $\mu = \sigma_{xx}/(en_{Hall})$. The control sample is capped by PMMA and was measured on day 2. From **Figure 23**, we can see the sheet carrier density $n_{2D}$ decreases from $6.4\times10^{12}/cm^2$ in bare $Bi_2Se_3$ to $4.2\times10^{12}/cm^2$ in the F4TCNQ sample and to $4.0\times10^{12}/cm^2$ in the $Co(acac)_3$ sample while mobility is enhanced from 1320 $cm^2/Vs$ to 1780 $cm^2/Vs$ and 1940 $cm^2/Vs$ respectively. We fit the data to analyze the quantitative change from THz spectra. A representative fit is shown as dashed lines in **Figure 22a-b**. Fitting parameters are plotted in **Figure 24a-b**.

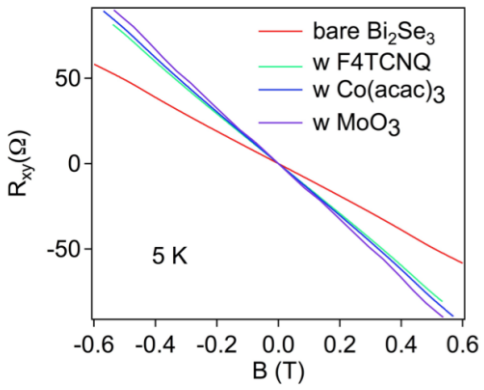


**Figure 23.** Hall resistance for 16QL bare $Bi_2Se_3$, with 50 nm F4TCNQ, with 50 nm $Co(acac)_3$ and with 50 nm $MoO_3$ at 5 K.

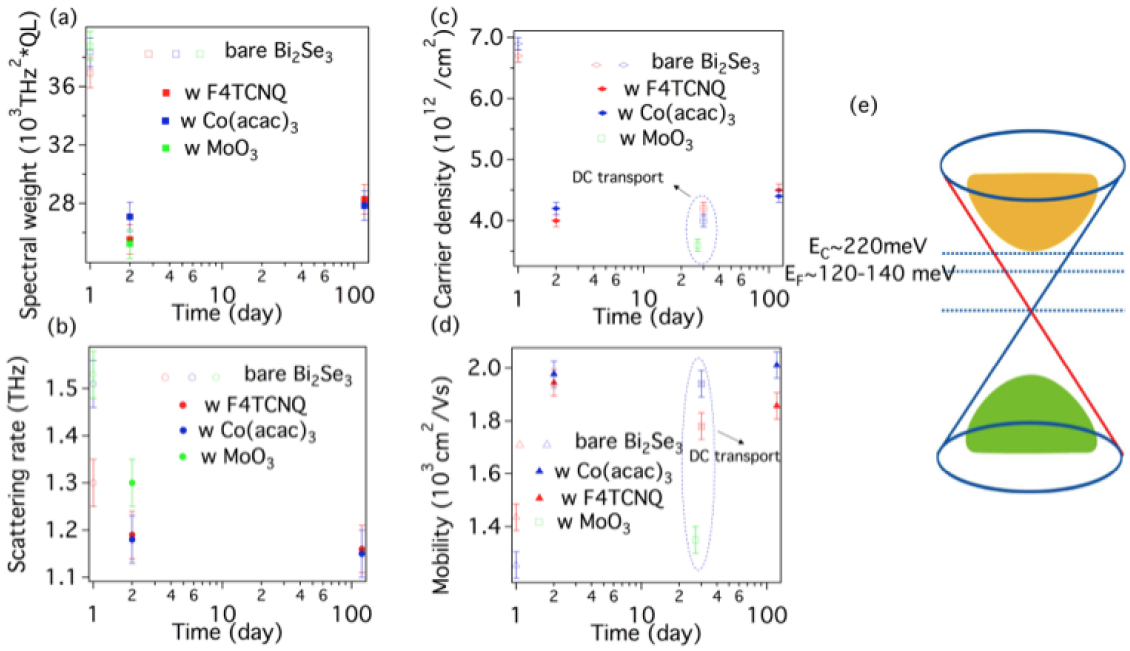


**Figure 24.** (a) Drude spectral weight (b) Drude scattering rate (c) carrier density and (d) mobility as a function of time for 16QL bare $Bi_2Se_3$, with 50 nm F4TCNQ, with 50 nm $Co(acac)_3$ and with 50 nm $MoO_3$ at 5 K. The data points marked with open squares are from DC transport. (e) Energy level diagram indicates the Fermi level of TI/OSC devices have chemical potential 80-100 meV below conduction band minimum.

The spectral weight is clearly reduced, which is consistent with depletion of charges. The scattering rate is more or less unchanged, likely since lowering of the chemical potential reduces the phase space for scattering. The carrier density and mobility as a function of time are plotted in **Figure 24c-d**. F4TCNQ decreased the carrier density of sample 1 from 6.7 $\times 10^{12}/cm^2$ to 4.0 $\times 10^{12}/cm^2$, while the mobility is enhanced from 1440 $cm^2/Vs$ to 1950 $cm^2/Vs$. More importantly, F4TCNQ protects the sample from severe aging effects over time. For instance, carrier density in bare $Bi_2Se_3$ would increase to $10 \times 10^{12}/cm^2$, which corresponds to the conduction band minimum, within a week.[12]

After four months, sample 1 with F4TCNQ has similar reduced carrier density of 4.5 $\times 10^{12}/cm^2$ and mobility 1860 $cm^2/Vs$. Converting this into the chemical potential value above the Dirac point, it is still stabilized at $E_F$~140 meV (80 meV below the conduction band). F4TCNQ is known as one of the strongest hole donors/electron acceptors among organic materials. $Co(acac)_3$ on the other hand is a new organic CE layer that we found to be as effective for this system. $Co(acac)_3$ depletes the carrier density of $Bi_2Se_3$ sample 2 from $6.9\times10^{12}/cm^2$ to $4.2\times10^{12}/cm^2$ while the mobility is enhanced from 1260 $cm^2/Vs$ to 2020 $cm^2/Vs$. After four months, sample 2 with $Co(acac)_3$ has a carrier density $4.4\times10^{12}/cm^2$ and mobility 1980 $cm^2/Vs$, which corresponds to a chemical potential above the Dirac point of 135 meV (85 meV below conduction band).

Even at room temperature, sample 1 with F4TCNQ has a carrier density of $4.3\times10^{12}/cm^2$ and mobility of 1080 $cm^2/Vs$ and sample 2 with $Co(acac)_3$ has a carrier density of $4.5\times10^{12}/cm^2$ and mobility of 1120 $cm^2/Vs$. This shows the chemical potential is maintained ~80 meV below the conduction band minimum, so we realized and stabilized a room-temperature intrinsic topological insulator with high mobility. The experiments on F4TCNQ and $Co(acac)_3$ were repeated at least three times and show the same results. We also thermally evaporated $MoO_3$ on top of $Bi_2Se_3$ to compare with our OSCs, and performed THz spectroscopy (**Figure 22e-f**) and DC transport (**Figure 23**) measurements. We found that $MoO_3$ reduces the total sheet carrier density to 3.6 $\times$ $10^{12}/cm^2$, which corresponds to both surface states having their chemical potential ~120 meV above the Dirac point.

Interestingly we observe that three compounds deplete the carriers similarly despite their different molecular orbital energies. The energy levels are shown in **Figure**

**25**. The Fermi energy of isolated $Bi_2Se_3$ is reported to be about 4.9 eV below the vacuum level.[11] The reason why thermally evaporated $MoO_3$ does not reduce carrier density more is likely because the film quality is not as good as MBE deposition and it is processed ex-situ, with transfer steps between depositions. The good performance of $Co(acac)_3$ is surprising considering its relatively high LUMO bands, which does not indicate a thermodynamic/enthalpic driving force for the extraction of electrons from $Bi_2Se_3$ by $Co(acac)_3$. However, entropic considerations would lead to some electron transfer in spite of unfavorable enthalpy, and there are a number of mechanisms by which charge transfer or accumulation could still occur. First, the oxidizing power of solid $Co(acac)_3$ might be higher than the dissolved form so it is not obvious from these reported levels (typically in solution) that charge extraction would occur. Second, the solid film might contain Co(III) species that are not fully coordinated, so individual sites of higher oxidizing power might be present. Third, the formation of an interfacial dipole between $Bi_2Se_3$ and $Co(acac)_3$ might interpose an additional driving voltage promoting electron transfer out of $Bi_2Se_3$ into $Co(acac)_3$. In addition to electron transfer, the $Bi_2Se_3$-$Co(acac)_3$ interface could be rich in intermetallic chemical species that could act as electron traps, such as by the passivation of Se vacancies that are the main origin of the mobile electrons.

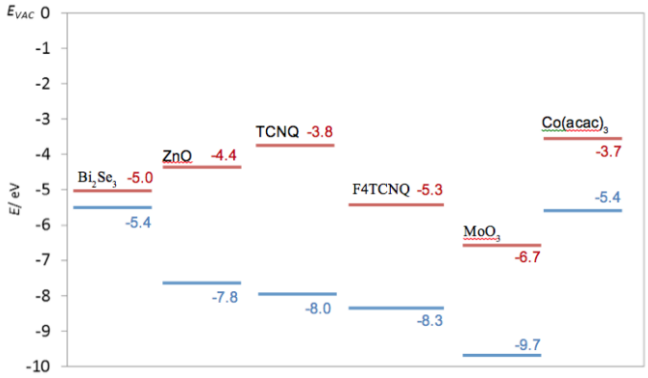


**Figure 25**. Energy level diagram with energy band edges for $Bi_2Se_3$[11], ZnO[9], 7,7,8,8-tetracyanoquinodimethane (TCNQ)[9], F4TCNQ[9], $MoO_3$[10], and redox potentials of $Co(acac)_3$[12]. Blue and red lines stand for highest occupied molecular orbital (HOMO) and lowest unoccupied molecular orbital (LUMO) bands.

## References


1. R. Valdés Aguilar, A. V. Stier, W. Liu, L. S. Bilbro, D. K. George, N. Bansal, L. Wu, *Phys. Rev. Lett.* **2012**, 108, 087403.

2. M. K. Kashif, J. C. Axelson, N. W. Duffy, C. M. Forsyth, C. J. Chang, J. R. Long, L. Spiccia U. Bach, *J. Am. Chem. Soc.* **2012**, 134, 16646–16653.

3. N. Koirala, M. J. Brahlek, M. Salehi, L. Wu, J. Dai, J. Waugh, T. Nummy, *Nano Lett*. **2015**, 15, 8245-8249.

4. L. Wu, M. Brahlek, R. Valdés Aguilar, A. V. Stier, C. M. Morris, Y. Lubashevsky, L. S. Bilbro, N. Bansal, S. Oh, N. P. Armitage. *Nature Physics* **2013**, 9, 410.

5. L. Wu, W.K. Tse, M. Brahlek, C. M. Morris, R. Valdés Aguilar, N. Koirala, S. Oh, N. P. Armitage. *Phys. Rev. Lett.* **2015**, 1, 217602.

6. C. H. Li, O. M. J. van't Erve, J. T. Robinson, Y. Liu, L. Li, B. T. Jonker, *Nature Nanotechnology* **2015**, 9, 218-224.

7. M. Veldhorst, M. Snelder, M. Hoek, T. Gang, V. K. Guduru, X. L. Wang, U. Zeitler, *Nature Mater.* **2012**, 11, 417-421.

8. Y. Okada, V. Madhavan, *Nature Nanotechnology* **2013**, 8, 541.

9. W. Chen, D. Qi, X. Gao, A. T. S. Wee, *Prog. Surf. Science* **2009**, 84, 279-321.

10. J. Meyer, S. Hamwi, M. Kroger, W. Kowalsky, T. Riedl, A. Kahn, *Adv. Mater.* **2012**, 24, 5408-5427.

11. J. Suh, D. Fu, X. Liu, J. K. Furdyna, K. M. Yu, W. Walukiewicz, J. Wu, *Phys. Rev. B* **2014**, 89, 11307.

12. C. W. Anderson, K. R. Lung, T. A. Nile, *Inorganica Chemica Acta*, **1984**, 85.

**Electrostatic Gating by Corona Charging of Electret Polymer**

Here we demonstrate the ability to tailor/reduce the carrier concentration of $Bi_2Se_3$ films prepared by MBE by utilizing a novel approach, namely nonvolatile electrostatic gating via the corona charging of electret polymers. Sufficient electric field can be imparted to a polymer-TI bilayer to result in significant electron depletion using a simple spincoated overlayer, even without the continuous connection of a gate electrode or the chemical modification of the TI. We show that the Fermi level of $Bi_2Se_3$ is shifted towards the Dirac point by altering $Bi_2Se_3$ carrier concentration with this method. We find that electrostatic gating is highly effective for lowering surface chemical potential into the bulk band gap and stabilize it in the intrinsic regime while enhancing electron mobility.

Some issues regarding the intrinsic behavior of $Bi_2Se_3$ are ameliorated using conventional static solid gates. For example, ceramic[1-12] gates have been used to observe changes in σ and magnetoelectronic effects. However, this still requires connection and operation of a gate electrode during charge density and transport measurements. To avoid this drawback, a few quasipermanent gating modifications have been made to TIs. Electron irradiation reversed the majority carrier sign in bismuth telluride.[13] In a related demonstration, corona charging of graphene on silicon carbide brought the charge density through the Dirac point.[14] Tuning the antimony/bismuth ratio in tellurides decrease the charge density by two orders of magnitude, with further decrease and carrier sign reversal obtained by gating.[15] Electron-accepting overlayers such as molybdenum trioxide and tetracyanoquinodimethane can be deposited adjacent to TIs.[16,17] A recent work also utilized organics to engineer topological insulators, but they increase the Fermi energy and created Rashba surface states, which are considered topologically trivial.[18]

Prompted by our initial observations of a strong influence of adjacent static charge on charge carrier density in bismuth selenide topological insulator, we performed a systematic study of conditions and materials that would allow the maximum static electric field to be stored in a polymer dielectric layer overlying the selenide. Polymer-hosted static charge offers the combination of kinetic stability, all-solid-state configuration, and high absolute gating voltage.

We selected commercially available polymers: polystyrene, polystyrene with 3% chloromethylstyrene comonomer, polystyrene with 3% $C_{60}$-methyl side chains, and the perfluorinated polymers Cytop and Novec, the latter two being registered trademarks of Asahi Glass and 3M, respectively. All four are highly hydrophobic, have wide

electrochemical windows, and would be expected to have little or no chemical interaction with $Bi_2Se_3$. Polystyrene and Cytop are known electret/charge storage materials, with demonstrated capability to tune semiconductor charge densities in a nonvolatile way.[19-25] The chloromethylstyrene and $C_{60}$-methylstyrene derivatives were investigated to see whether the labile chloro groups or additional fullerene energy levels would increase charge trapping relative to polystyrene. Novec has apparently not been used for this purpose before, but as will be seen, is particularly advantageous for the application under consideration here.

Static charge was applied to the upper polymer surface via a metal screen (a "grid") powered by a corona (plasma) emanating from a needle above the grid, establishing a potential of 10,000 volts between the needle and a grounded copper stage, as shown in **Figure 26**. A grounded metal chamber encloses the entire apparatus, and is never removed when the needle or grid are powered. A key aspect of the charging procedure is to ground the bismuth selenide layer via copper tape to the ground plate of the apparatus in an attempt to set the $Bi_2Se_3$ semiconducting layers to ground as well, as shown in **Figure 26**. Stable polarization, up to 1 kV, as functions of charging time and voltage, have been recorded. Stored voltage was indicated by measuring with an electrostatic voltmeter (Isoprobe 279, Monroe Electronics). The electrostatic voltmeter is a surface DC voltmeter that measures surface potential in the range of ±3000 volts without physically contacting the measured surface. It features high-accuracy (0.1%), drift-free measurements that are almost fully independent of probe-to-surface separation.

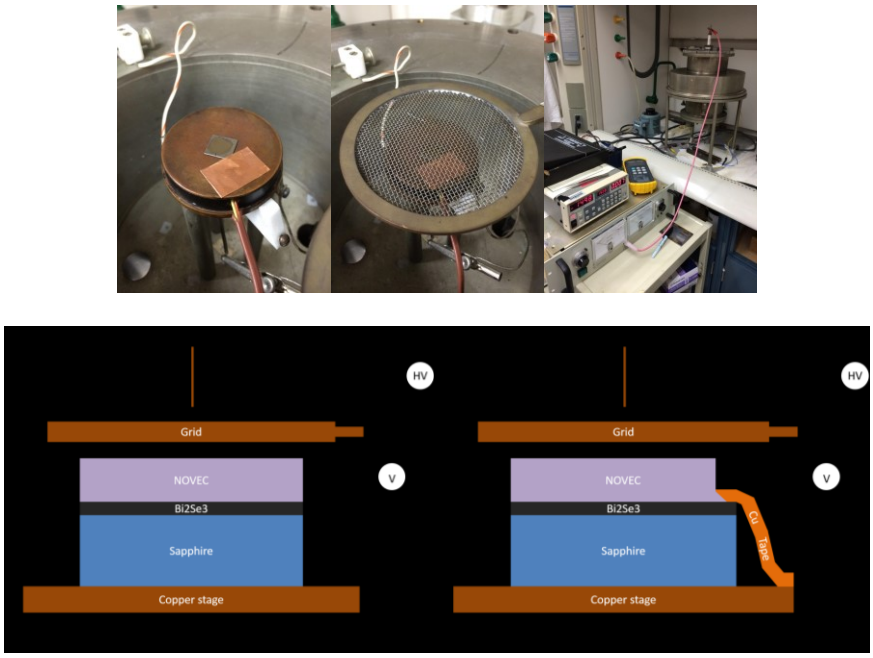


**Figure 26.** Photographs (top, left to right) of a sample and copper tape on the copper stage, the grid screen in place, and the external connection to the needle corona source. Schematics (bottom) of the corona charging setup with and without copper tape grounding of the $Bi_2Se_3$ layer.

Charging was carried out in the ambient atmosphere for specific time periods to determine the time evolution and maximum magnitude of deposited static voltage for each multilayer. We took data of surface voltages that result by imposing different grid voltages for 5 minutes, finding that the stored surface potential will saturate at some grid voltage (in the hundreds of volts for 2-5 micron thick drop-cast polymers). This is consistent with a measured RC time constant of 20-150 seconds for the polymer films. We also imposed various high grid voltages for varying amounts of time, in order to check how long it takes to charge samples, determining that 5 minutes allows for more than enough time for saturated charging to be reached at each grid voltage used (less than

two minutes is typically required for full charging at given grid potential, and most charging occurs in the first 1-30 seconds). Our initial screening was conducted on gold-coated sapphire to conserve the more valuable $Bi_2Se_3$.We first compared the polystyrenes. Based on the effectiveness of the chloromethyl polymer and the modest influence of elevated temperature combined with a reluctance to heat TI films unnecessarily, we chose the 3%-chloromethylated polystyrene for an initial test on $Bi_2Se_3$. Representative data are shown in **Figure 27**. Conclusions drawn from this experiment are that both of the functionalized side chains contributed to charge storage ability, about half of the maximum voltage that could be stored across the entire sample could be localized between the top and bottom polymer surfaces, and about one third more voltage could be stored if the sample were heated to 80 ºC during charging.

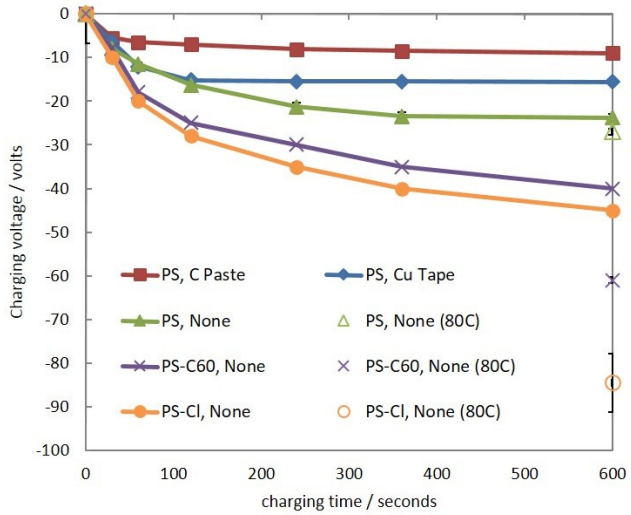


**Figure 27.** Surface charge measured as a result of corona charging for various times with -1500 V applied to the grid over spincoated polymer films (thickness of ~1 µm). PS, polystyrene. C60 and Cl refer to $C_{60}$-methyl and chloromethyl styrenes at 3% monomer

fraction. None, C paste, and Cu Tape refer to connections between gold and the grounded copper stage. 80 C refers to final surface voltages after heating the samples to 80 °C during the charging.

**Figure 28a** shows the resulting potential stored in Novec after charging at constant grid voltage as a function of time. **Figure 28b** shows the resulting potential stored in Novec after charging for a fixed time (5 minutes) at incremental grid voltages. **Figure 28c** shows the resulting potential stored in Novec after charging at single high grid voltage and then monitoring the stability of stored charge as a function of time (samples left in air). The effectiveness of a monolithic single-component charged electret in extracting charge carriers from bismuth selenide was demonstrated utilizing THz (AC) measurements and DC Hall measurements. **Figure 29a** shows three samples of $Bi_2Se_3$ without, with positive and with negative charged polystyrene with crosslinkable side chains. **Figure 29b** shows samples of $Bi_2Se_3$ without, and with negatively charged Novec in increasing increments. In the THz spectra, there is a Drude component peaked at zero frequency and a phonon peak at ~1.9THz. The area below the Drude conductance is proportional to carrier density over effective mass. Lower area means lower carrier density.

We can see $Bi_2Se_3$ with positive charged polymers has the smallest area and the negatively charged one has the highest area, indicating positive charged polymers deplete carrier density of surface states of $Bi_2Se_3$ while negative one increases carrier density a little. DC transport measurements reach the same conclusion. The sample with positive charged polymer has very low carrier density $1.8*10^{12}/cm^2$ and highest mobility

~1800cm$^2$/Vs at 5K. $Bi_2Se_3$ with neutral PMMA has carrier density 6.4*10$^{12}$/cm$^2$ and mobility ~1300cm$^2$/Vs at 5K. The sample with negative charged polymer has very low carrier density 6.8*10$^{12}$/cm$^2$ and mobility (~900 cm$^2$/Vs) at 5K. Even at room temperature, the sample with positive charged polymer has low carrier density 2.4*10$^{12}$/cm$^2$ and high mobility (~1100 cm$^2$/Vs). This is well into the topological regime where only surface state electrons are contributing, which makes room temperature application possible.

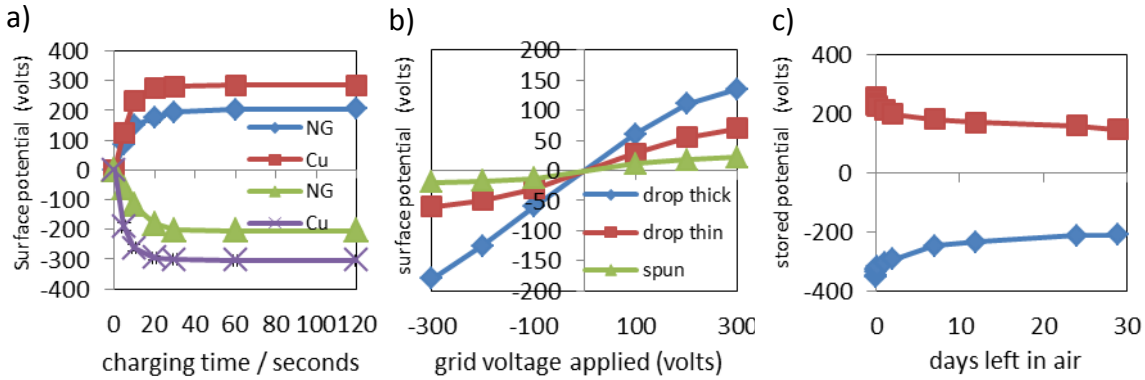


**Figure 28.** Plots shows the resulting potential stored in Novec after a) charging at constant grid voltage as a function of time, b) charging for a fixed time (5 minutes) at incremental grid voltages, and c) charging at single high grid voltage and then monitoring the stability of stored charge as a function of time (samples left in air).

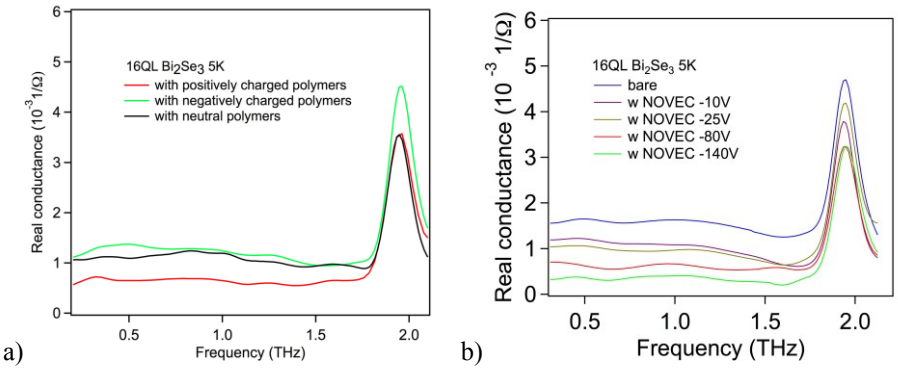


**Figure 29.** Frequency-dependent conductance of $Bi_2Se_3$ affected by charging of overlying a) cross-linkable PS or b) Novec.

## References


1. C. Z. Chang, Z. C. Zhang, K. Li, X. Feng, J. S. Zhang, M. H. Guo, Y. Feng, J. Wang, L. L. Wang, X. C. Ma, X. Chen, Y. Y. Wang, K. He, Q. K. Xue, *Nano Letters* **2015**, *15*, 1090-1094.

2. J. Chen, H. J. Qin, F. Yang, J. Liu, T. Guan, F. M. Qu, G. H. Zhang, J. R. Shi, X. C. Xie, C. L. Yang, K. H. Wu, Y. Q. Li, L. Lu, *Physical Review Letters* **2010**, 105.

3. X. Y. He, T. Guan, X. X. Wang, B. J. Feng, P. Cheng, L. Chen, Y. Q. Li, K. H. Wu, *Applied Physics Letters* **2012**, 101.

4. D. Kim, S. Cho, N. P. Butch, P. Syers, K. Kirshenbaum, S. Adam, J. Paglione, M. S. Fuhrer, *Nature Physics* **2012**, 8, 459-463.

5. J. Lee, J. Park, J. H. Lee, J. S. Kim, H. J. Lee, *Physical Review B* **2012**, 86.

6. A. Sulaev, M. G. Zeng, S. Q. Shen, S. K. Cho, W. G. Zhu, Y. P. Feng, S. V. Eremeev, Y. Kawazoe, L. Shen, L. Wang, *Nano Letters* **2015**, 15, 2061-2066.

7. J. F. Tian, C. Z. Chang, H. L. Cao, K. He, X. C. Ma, Q. K. Xue, Y. P. Chen, *Scientific Reports* **2014**, *4*.

8. L. X. Wang, Y. Yan, Z. M. Liao, D. P. Yu, *Applied Physics Letters* **2015**, 106.

9. F. X. Xiu, L. A. He, Y. Wang, L. N. Cheng, L. T. Chang, M. R. Lang, G. A. Huang, X. F. Kou, Y. Zhou, X. W. Jiang, Z. G. Chen, J. Zou, A. Shailos, K. L. Wang, *Nature Nanotechnology* **2011**, 6, 216-221.

10. F. Yang, A. A. Taskin, S. Sasaki, K. Segawa, Y. Ohno, K. Matsumoto, Y. Ando, *Applied Physics Letters* **2014**, 104.

11. F. Yang, A. A. Taskin, S. Sasaki, K. Segawa, Y. Ohno, K. Matsumoto, Y. Ando, *Acs Nano* **2015**, 9, 4050-4055;

12. T. Zhang, J. Ha, N. Levy, Y. Kuk, J. Stroscio, *Physical Review Letters* **2013**, 111.

13. C. W. Rischau, B. Leridon, B. Fauque, V. Metayer, C. J. van der Beek, *Physical Review B* **2013**, 88.

14. A. Lartsev, T. Yager, T. Bergsten, A. Tzalenchuk, T. Janssen, R. Yakimova, S. Lara-Avila, S. Kubatkin, *Applied Physics Letters* **2014**, 105.

15. D. S. Kong, Y. L. Chen, J. J. Cha, Q. F. Zhang, J. G. Analytis, K. J. Lai, Z. K. Liu, S. S. Hong, K. J. Koski, S. K. Mo, Z. Hussain, I. R. Fisher, Z. X. Shen, Y. Cui, *Nature Nanotechnology* **2011**, 6, 705-709.

16. Y. Tanabe, K. K. Huynh, R. Nouchi, S. Heguri, G. Mu, J. T. Xu, H. Shimotani, K. Tanigaki, *Journal of Physical Chemistry C* **2014**, 118, 3533-3538.

17. M. T. Edmonds, J. T. Hellerstedt, A. Tadich, A. Schenk, K. M. O'Donnell, J. Tosado, N. P. Butch, P. Syers, J. Paglione, M. S. Fuhrer, *Acs Nano* **2014**, 8, 6400-6406.

18. Koirala, Nikesh, Matthew J. Brahlek, Maryam Salehi, Liang Wu, Jixia Dai, Justin Waugh, Thomas Nummy *Nano Letters*. **2015**, 15, 8245-8249.

19. U. Bartsch, J. Gaspar, O. Paul, in *Polymer-Based Smart Materials - Processes, Properties and Application, Vol. 1134* (Eds.: S. Bauer, Z. Cheng, D. A. Wrobleski, Q. Zhang), **2009**, pp. 223-228.

20. T. J. Dawidczyk, J. F. M. Hardigree, G. L. Johns, R. Ozgun, O. Alley, A. G. Andreou, N. Markovic, H. E. Katz, *Acs Nano* **2014**, 8, 2714-2724.

21. T. J. Dawidczyk, G. L. Johns, R. Ozgun, O. Alley, A. G. Andreou, N. Markovic, H. E. Katz, *Applied Physics Letters* **2012**, 100.

22. K. D. Deshmukh, K. Reuter, H. Kempa, J. E. West, H. E. Katz, *Applied Physics Letters* **2009**, 95.

23. D. P. Erhard, D. Lovera, R. Giesa, V. Altstadt, H. W. Schmidt, *Journal of Polymer Science Part B-Polymer Physics* **2010**, 48, 990-997.

24. K. Kashiwagi, K. Okano, T. Miyajima, Y. Sera, N. Tanabe, Y. Morizawa, Y. Suzuki, *Journal of Micromechanics and Microengineering* **2011**, 21.

25. K. Reuter, H. Kempa, K. D. Deshmukh, H. E. Katz, A. C. Hubler, *Organic Electronics* **2010**, 11, 95-99.

# CHAPTER 4

# Thermoelectric Application

## Introduction

Waste heat is one of our most abundant alternative energy sources because less than 40% of the energy input to conventional systems is converted to useful work, while over 60% is wasted in the form of dissipating heat (according to study at Lawrence Berkeley, 2010). The intention of thermoelectric energy harvesting is to reuse some of this waste heat, and therefore make all of our current systems more efficient, from stoves to cars to solar panels to the human body. Not only can thermoelectric materials harvest energy from heat, but they can also be used as solid-state refrigerators. No moving parts or additional materials or harmful gases are needed to remove heat from a system, just electricity.

Many researchers are interested in high-performance and high-temperature inorganic materials for these purposes. Unfortunately, fabricating inorganic materials into large area modules involves high-cost processes, making it challenging to affordably integrate these rigid, high performance materials into unusual topologies. Hence there is growing and immediate interest in composites of inorganic particles and organic semiconducting materials for thermoelectric energy harvesting and spot cooling applications.[1-6] Physical mixing, solution mixing, and in-situ synthesis of polymers and/or inorganic crystals have all been used to prepare polymer-inorganic composites which show TE improvements over the individual constituents, leading to greater practical efficiencies. Such composites combine solution processing, mechanical

flexibility, and potentially low thermal conductivity, potentially contributing to high values of the figure of merit, $ZT = S^2\sigma T/\kappa$, where S is Seebeck coefficient, $\sigma$ is electronic conductivity, T is absolute temperature, and $\kappa$ is thermal conductivity.[7-9] $S^2\sigma$ is known as the power factor.

Polymer-based materials would be less expensive to implement, could be applied to surfaces with irregular geometries, and would desirably contain only common and nontoxic elements. Polymers have inherent advantages in their physical and mechanical properties, such as light weight, tunable flexibility, and broad optical modification, which contribute practical efficiency to polymer-based electronics rather than performance efficiency.[10-13] Furthermore, the versatility of polymer processing, and low-energy required to make these materials, renders them more cost effective and allows alternative processing techniques to be utilized, such as all-solution processing and printing. Their ease of processing, low cost and environmental impact compared to typical thermoelectric materials will allow sustainable large-scale production. Although they may become more practical, however, they will always have lower working efficiency because polymeric materials degrade at sufficiently high temperatures (and working efficiency increases with increasing temperature difference being utilized). Although organic polymers are not stable at high temperatures (above 250 ˚C) they may be of great interest in niche applications for room temperature cooling and TE power generation on the micro-scale where sufficient power is more critical than high efficiency. Applications include small-scale refrigeration, thermal diodes, and off-grid or battery-free power supply to wireless or mobile devices, such as hearing replacements, implants, thermal powered LED and LED coolers.

Significant progress has been made in increasing thermoelectric power factors of hole-carrying (p-type) polymers,[14-18] with values >100 μW/mK$^2$ that lead to ZT >0.1. The search for high efficiency n-type polymer-based materials is more challenging. We recently reported the first measurement of thermoelectric properties of an n-type polymer.[19] Following that, values on the order of 0.1 μW/mK$^2$ were reported for the commercial polymer Polyera N2200, and this was termed the "highest value obtained to date".[20]

Progress towards greater power factors has been achieved in p-type polymers by incorporating high performance inorganic TE materials. Elemental tellurium is worthy of consideration for these purposes because of its well defined composition, high charge carrier mobility, and submetallic charge carrier density.[21-23] The readiness with which Te forms nanostructures is favorable for homogeneous microscale mixing and possible reduction in thermal conductivity that is the main origin of inefficiencies in thermoelectric energy conversions. Recently, a collaboration at Lawrence Berkeley Laboratories demonstrated the dispersion of Te nanostructures in an aqueous solution of the conducting thiophene polymer poly(3,4-ethylenedioxythiophene) (PEDOT), and cast films of the combined materials to form composites with ZT of about 0.1.[5] The use of Te nanostructures in thermoelectrics was suggested earlier, and the fundamental thermoelectric properties of elemental Te have appeared in literature extending decades back.[24-27]

Our group measured a value of 80 μW/mK$^2$ for an n-type $Bi_2Te_3$ particle-PEDOT composite,[4] but this material suffered from the partial cancellation of the negative $Bi_2Te_3$ Seebeck coefficient by the positive Seebeck of the p-type polymer used. In addition,

$Bi_2Te_3$, like many other inorganic thermoelectric materials, is undesirably composed of less common and toxic elements. It is desirable to develop electron-carrying (n-type) thermoelectric polymer composites with common-element inorganic compounds.

We use standard thermoelectric measurement techniques, taken on a homemade setup. The Seebeck coefficient is measured with the sample mounted between a pair of Peltier heater-cooler tiles, with one electrode of the sample over each tile. Thermal EMF ($\Delta V$) and temperature difference ($\Delta T$) were measured simultaneously by probing the pair of electrodes with a source meter and thermocouples. Numerous measurements of $\Delta V$, typically 500, were made for each value of $\Delta T$, with a standard deviation of 1-5% (0.01-0.05 mV) per data set. These $\Delta V$ were averaged to eliminate the noise signal induced by the environment and obtain just the consistent steady-state value. Several $\Delta T$ were imposed on the sample. The slopes of $\Delta V$ versus $\Delta T$ gave values of the Seebeck coefficient. The linearity of the data of $\Delta V$ and $\Delta T$ was used as a key criterion to ensure valid measurements. The setup is calibrated using Ni metal, for which the value we obtain (-21.0 ± 0.6 μV/K) agrees well with those reported (-20.5 μV/K). Conductivity measurements were employed using an Agilent 4155C Semiconductor Parameter Analyzer. Resistance was measured by obtaining I-V curves, and conductivity was calculated using the physical dimensions of each device. All devices are tested under ambient conditions in air, but protected from light and convection.

We have shown that Te vapor-deposited as a nominal 10 nm film onto Corning glass gives a positive Seebeck coefficient of 400 ± 10 μV/K. Te deposited on 6PTTP6 acted with the same polarity and improved Seebeck, 457 ± 6 μV/K.[28] Possible reasons for this are introduction of new hole energy levels at the 6PTTP6 interface that were not

present in Te-on-glass, or increased surface area of crossing Te nanowires, with which additional energy states could be associated. Although the nanocrystalline network on glass showed conductivity of 227 ± 21 S/m, and the hybrid bilayer shows conductivity of 216 ± 16 S/m (accounting for the thickness of Te only, about 10 nm, measured by quartz crystal microbalance during deposition), the resulting power factor was enhanced from 36 ± 3 to 45 ± 4 W/mK$^2$. Pure 6PTTP6 has essentially no conductivity (less than 0.01 S/m), so we conclude that changes in power factor are completely due to charge transport being affected in Te. In this case, the bilayer provides an enhancement in Seebeck without compromising conductivity drastically. Pentacene bilayers resulted in similar Seebeck to 6PTTP6 bilayers (468 ± 9 μV/K), but with more conductivity (266 ± 36 S/m), producing higher power factors (58 ± 6 W/mK$^2$). The interlayer potential created over each 2D interface plays a significant role in charge transport, accumulation, and trapping. For instance, the pentacene HOMO level is more positive than the work function of Te, which implies that it accepts holes from Te more readily than 6PTTP6, having a HOMO level more negative than the Te work function. Consequently, scattering of charges at the pentacene-Te interface may be reduced compared to 6PTTP6 and glass interfaces. With optimization, these values compare favorably to other hybrid systems.[1,9] However, in the future we would prefer to move away from tellurium-based materials, or other rare or toxic materials.

Recently we systematically investigated the S and σ for thin-films of electron-conducting (n-channel) organic polymers. For this we were focused on a recently synthesized polymer. The polymer is a pyromellitic diimide (PyDI)-based structure with acetylene linkages that we have recently reported as the first such polymer to show

activity in an n-channel field-effect transistor, and which we measure as having a higher intrinsic Seebeck coefficient (and greater unipolarity) than commercial polymer N2200. Commercially available Polyera N2200 serves as another n-channel polyimide for comparison, with the chemical name P(NDI2OD-T2). **Figure 30** shows the chemical structure for the two n-channel polymers used in this proposal, PyDI-5FPE (a) and P(NDI2OD-T2) (b), and for two p-channel polymers mentioned later, P3HT (c) and PQT12 (d).

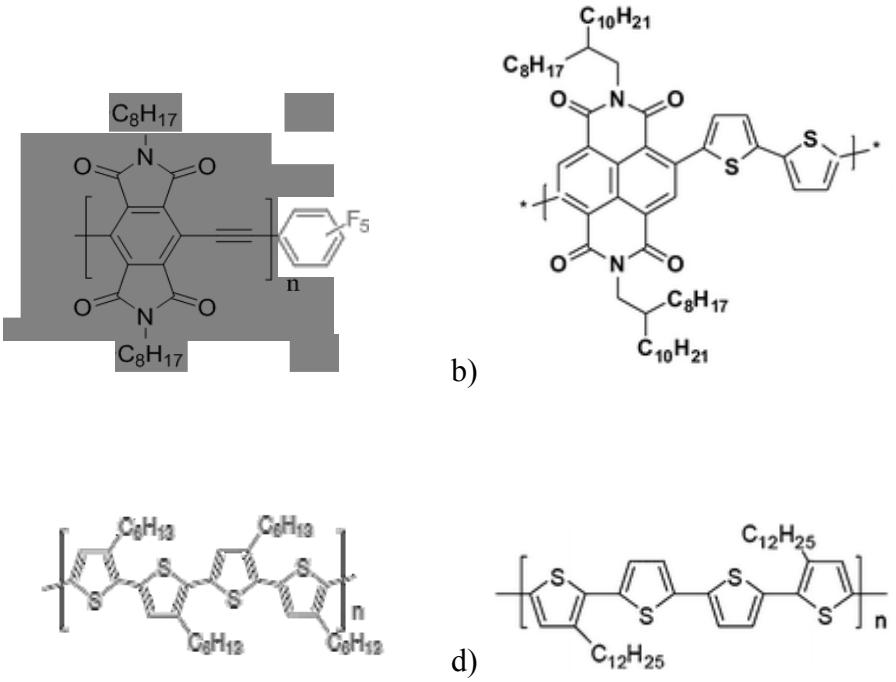


**Figure 30**. Chemical structure of a) poly(PyDI-ethynylene)-5FPE, b) P(NDI2OD-T2), c) P3HT, and d) PQT12.

PyDI-5FPE shows modest conductivity in its undoped form (0.001 S/cm), and a significant S (-220 μV/K). P(NDI2OD-T2) shows greater conductivity (0.001 S/cm), as expected due to higher intermolecular overlaps of diimide cores, but only slightly greater

power factor due to lower intrinsic S (-130 μV/K). Power factors are 0.014 and 0.029 $\mu W/mK^2$ for PyDI-5FPE and P(NDI2OD-T2) respectively. Our value for the power factor is one tenth of that which was reported in Advanced Materials, 2014.[20] This is because our measured Seebeck coefficients are lower (they obtained around -800 μV/K). However, we also measured thermal conductivity recently, which is only being done by a handful of laboratories because this it is so difficult in polymer systems. The thermal conductivity we measured is 0.14 W/mK for both PyDI-5FPE and P(NDI2OD-T2) polymers, thusly the thermoelectric ZT of both polymers are on the order $1x10^{-5}$.

**References**


1. Y. Y. Wang, K. F. Cai, X. Yao. *J. Nanoparticle Research* **2012**, 14.

2. Y. Du, K. F. F. Cai, S. Z. Shen, B. J. An, Z. Qin, P. S. Casey. *J. Mater. Sci., Mater. Elec.* **2012**, 23, 870.

3. N. Toshima, M. Imai, S. Ichikawa. *J. Elec. Mater.* **2011**, 40, 898.

4. B. Zhang, J. Sun, H. E. Katz, F. Fang, R .L. Opila. *ACS Appl. Mater. Interf.* **2010**, 2, 3170.

5. K. C. See, J. P. Feser, C. E. Chen, A. Majumdar, J. J. Urban, R. A. Segalman. *Nano Lett.* **2010**, 10, 4664.

6. S. K. Yee, N. E. Coates, A. Majumdar, J. J. Urban, R. A. Segalman, *Physical Chemistry Chemical Physics* **2013**, *15*, 4024-4032.

7. M. Zebarjadi, K. Esfarjani, M. S. Dresselhaus, Z. F. Ren and G. Chen. *Energy Environ. Science* **2012**, 5, 5147.

8. Y. C. Lan, A. J. Minnich, G. Chen and Z. F. Ren. *Adv. Funct. Mater.* **2010**, 20, 357.

9. T. O. Poehler, H. E. Katz, *Energy Environ. Science* **2012**, 5, 8110.

10. O. Bubnova, X. Crispin, *Energy Environ. Science.* **2012**, 5, 9345.

11. W.M. Qu, M. Plotner, W. J. Fischer, *J. Micromech. Microeng.* **2011**, 11, 146.

12. W. Glatz, E. Schwyter, L. Durrer, C. *J.* Hierold, *Microelectromech. Syst.* **2009**, 18, 763.

13. K. Yazawa, A. Shakouri, *J. Electronic Materials* **2012**, 41, 1845.

14. M. Leclerc, A. Najari, *Nature Mater.* **2011**, 10, 409-410.

15. G. H. Kim, L. Shao, K. Zhang, K. P. Pipe, *Nature Mater.* **2013**, 12, 719-723.

16. M. He, F. Qiu, Z. Q. Lin, *Energy Environ. Science* **2013**, 6, 1352-1361.

17. M. Chabinyc, *Nature Mater.* **2014**, 13, 119-121.

18. O. Bubnova, Z. U. Khan, H. Wang, S. Braun, D. R. Evans, M. Fabretto, P. Hojati-Talemi, D. Dagnelund, J. B. Arlin, Y. H. Geerts, S. Desbief, D. W. Breiby, J. W. Andreasen, R. Lazzaroni, W. M. M. Chen, I. Zozoulenko, M. Fahlman, P. J. Murphy, M. Berggren, X. Crispin, *Nature Mater.* **2014**, 13, 190-194.

19. S. Kola, J. H. Kim, R. M. Ireland, M. L. Yeh, K. Smith, W. M. Guo, H. E. Katz, *ACS Macro Lett.* **2013**, 2, 664-669.

20. B. Russ, M. J. Robb, F. G. Brunetti, P. L. Miller, E. E. Perry, S. N. Patel, V. Ho, W. B. Chang, J. J. Urban, M. L. Chabinyc, C. J. Hawker, R. A. Segalman, *Adv.Mater.***2014**, 26.

21. L. B. Luo, F. X. Liang, X. L. Huang, T. X. Yan, J. G. Hu, Y. Q. Yu, C. Y. Wu, L. Wang, Z. F. Zhu, Q. Li, J. S. Jie. *J. Nanoparticle Research* **2012**, 14.

22. H. Tao, H. M. Liu, D. H. Qin, K. Chan, J. W. Chen, Y. Cao, *J. Nanoscience Nanotechnology* **2010**, 10, 7997.

23. A. Zaiour, K. Zahraman, M. Roumie, J. Charara, A. Fawaz, F. Lmai, M. Hage-Ali, *Mater. Sci. Eng. B.* **2006**, 131, 54.

24. C. H. Cartwright, *Annalen Der Physik.* **1933**, 18, 656.

25. S. Chaudhuri, B. Chakrabarti, A. K. Pal, *Solid Films* **1981**, 82, 217.

26. S. K. Ramasesha, A. K. Singh, *Philosophical Magazine B-Physics of Condensed Matter Statistical Mechanics Electronic Optical and Magnetic Properties* **1991**, 64, 559.

27. A. K. Sharma, *Physica Status Solidi a-Applied Research* **1983**, 77.

28. J.Sinha, R. M. Ireland, S. Lee, H. E. Katz, *MRS Communications* **2013**, 3, 97-100.

## Interfacial Fields in Polymer-Particle Composites

### N-type Composite Hybrids

Polymer thermoelectrics are attractive for energy harvesting and localized cooling amid moderate temperature gradients and irregular surfaces, where toxic or rare elements are avoided, and low-cost print-processing is preferred. While significant progress has been made in p-type polymer composites, there are few unipolar n-type composites for this purpose. In order to enhance their n-type thermoelectric performance, we investigate hybrid thin films incorporating organometallic particles that can be dispersed in the polymer via facile solution-processing utilizing convenient precursors. Specifically, inorganic semiconductor domains are grown in polymer films *in situ*. All films are fabricated and tested at room temperature in air, and hybrid composites are analyzed as a function of initial precursor concentration. The inorganic component I have had the most success with so far is $SnCl_2$, an inexpensive and soluble compound known as an effective reducing agent in organic synthesis. However this salt has never been considered before

as a dopant for electronic materials, nor grown in a microstructured or nanostructured form for electronic material application.

Many researchers have sought soluble additives for n-type polymers that could provide n-type thermoelectric activity and also doping capability for the polymers, itself a challenge.[1-4] We expect composites to have improved thermoelectric performance due to enhanced electron conduction pathways, enhanced polymer doping, additional electronic states at the domain interfaces, along with low thermal conductivity. Polymer-assisted microstructure growth has been shown to strengthen interfacial interactions, including electronically driven interactions between polymer and as-grown particles. For example, cadmium telluride nanocrystals were synthesized in poly(3-hexylthiophene) without surfactants for photovoltaic applications.[5] Spectral results show that the particles are bound to the polymer via dipole-dipole interactions and form a charge transfer complex. We chose $SnCl_2$ as an additive because of its well-established reducing activity in organic chemistry. Surprisingly, its electronic properties as an anhydrous solid do not appear to have been measured, nor has its *in-situ* microcrystallization in polymer environments been observed; the closest precedent being hydrated proton conductors.[6,7] Other tin-based materials have previously been investigated as potential TE materials, experimentally and through computation, including pure tin films, tin oxides, tin selenides, tin clathrates, and tin sulfide, or as beneficial TE impurities in telluride-based materials.[8-19]

We now show that a form of our original pyromellitic diimide (PyDI) polymer, with pentafluorophenyl end caps (thus abbreviated PyDI-5FPE), mixed with in situ-crystallized $SnCl_2$, forms a particularly effective platform for n-type polymeric thermoelectric materials. We compare this system with a commercial n-type polymer,

P(NDI2OD-T2) (Polyera N2200), and with analogous p-type polymer systems (PQT12 and P3HT with cobalt(III) acetylacetonate ($Co(acac)_3$)) to show more broadly that weakly-doping microstructured inclusions can act synergistically with both n- or p-type polymers to give enhanced thermoelectric performance. **Figure 31a** shows the chemical structure for the polymers.

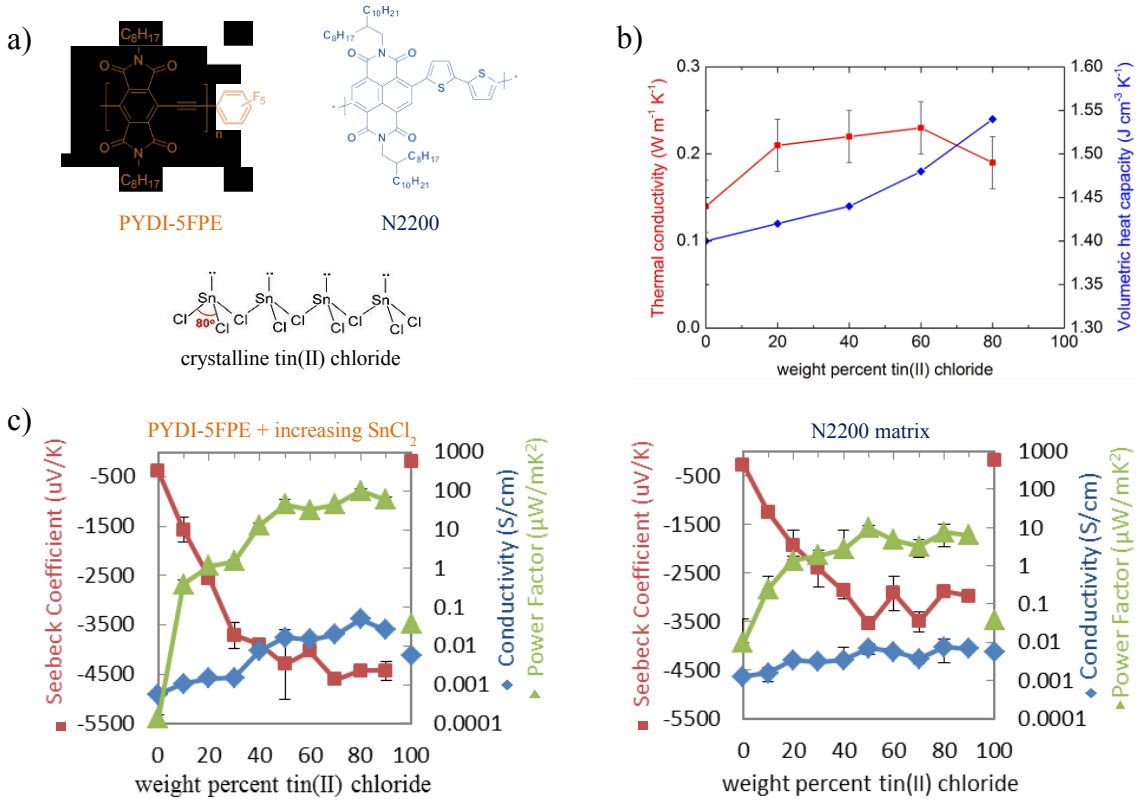


**Figure 31** a) Chemical structure of poly(PyDI-ethynylene)-5FPE, P(NDI2OD-T2) (known as N2200), and tin(II) chloride. b) Thermal conductivity and heat capacity vs weight % $SnCl_2$ in P1 films. c) The Seebeck coefficient, electrical conductivity, and power factor are plotted versus concentration of initial tin(II) chloride precursor within PYDI-5FPE (left) and P(NDI2OD-T2) (right) polymer matrices. Values are the average of at least 10 samples. Error bars are standard deviations.

The novel n-type pyromellitic diimide polymer composite with in-situ microstructure growth of the common element compound $SnCl_2$ can reach power factor of 50 to 100 $\mu W/mK^2$, largely from a gigantic Seebeck coefficient between -4000 and -5000 $\mu V/K$ in the composite (**Figure 31c**), which is between 5 and 100 times higher than what has been reported for prior polymer composites. With a low thermal conductivity, ~0.2 W/m K, the ZT now projects to an unprecedented value > 0.1 for an n-type solution-processable thermoelectric polymer.[20] The principle of using solid, weakly doping inclusions in semiconducting polymers, demonstrated here for $SnCl_2$ in imide polymers and also $Co(acac)_3$ in thiophene polymers, is broadly applicable.

Our n-type polymer is particularly effective at promoting $SnCl_2$ micro/nano-structure growth. Power factors of hybrid composites are greater than any of the individual components, reaching 80 $\mu W/mK^2$ for tin precursor concentrations above 50 wt%. These power factors were obtained without any strong n-doping, and were observed under ambient conditions. The power factors are on par with high performing p-type hybrid composites, but show much lower electrical conductivity. We expect the ZT to be greater than 0.1 for highest performing tin oxide-PyDI-5FPE blends, which show slightly increased thermal conductivity of about 0.2 W/mK. Although there is much room for improvement (via chemistry and processing), our use of a novel unipolar n-type polymer and inorganic additives has led to the first demonstration of ZT > 0.1 in electron-only polymer composites that contain neither highly toxic nor rare elements.

Most dramatically, *in situ* microwire/nanostructure growth of $SnCl_2$ enormously increases the Seebeck coefficients and electrical conductivities of the polymers. The

difference is only observed for 5FPE-PyDI and not for N2200 because microwires uniquely grow in the former polymer, likely contributing conducting paths and interfacial states that enhance the Seebeck coefficient. Only well-dispersed spherical clusters are obtained in N2200, which resembles a more homogenous bulk composite. The growth of distinct inorganic domains creates a more heterogeneous composite. Further reduction of the crystallite sizes, from micro- to nano-scale, will improve the TE performance further. Incorporation of $SnCl_2$ and subsequent drop-casting or spin-casting on glass results in spontaneous formation of tin-based microcrystals within the PyDI-5FPE polymer matrix during solvent evaporation. **Figure 32** shows laser optical micrographs of representative morphologies of $SnCl_2$ in PyDI-5FPE prepared by slow solvent evaporation during drop-casting, increased solvent evaporation rate, and by spin-casting. **Figure 33** shows laser optical micrographs of $SnCl_2$ in PyDI-5FPE for concentrations 20-90 wt%, and for pure $SnCl_2$ films prepared by drop-casting. The pure $SnCl_2$ films were processed exactly the same way as composites, meaning that the powder was dispersed in organic solvent but not mixed with polymer, just drop-cast or spin-cast onto the substrate utilizing the same conditions. Pure inorganic films are very rough and have low surface coverage, and precipitate very easily, making thicker films especially difficult to fabricate. These issues can be overcome somewhat by decreasing the solvent concentration used to make a solution (particle concentrations 10-100 mg/ml can be more amenable), and using a well with walls that are many micrometers high.

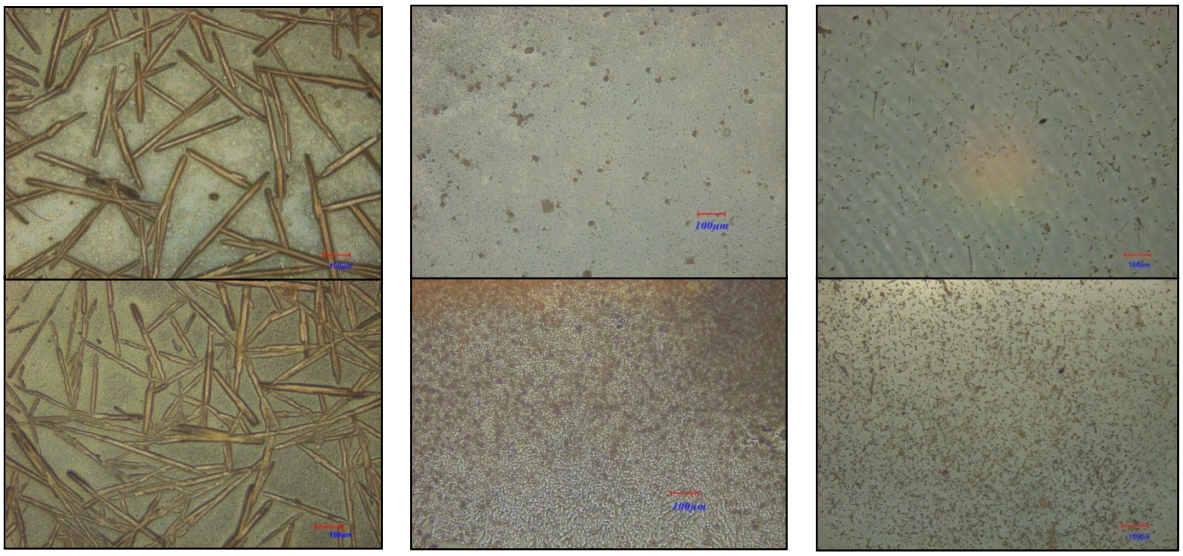

**Figure 32.** Optical microscope images of 60wt% $SnCl_2$ (top) and 70wt% $SnCl_2$ (bottom) in PyDI-5FPE polymer, captured as microwires by drop-casting (left), clusters by drop-casting (middle), and submicron clusters by spin-casting (right).

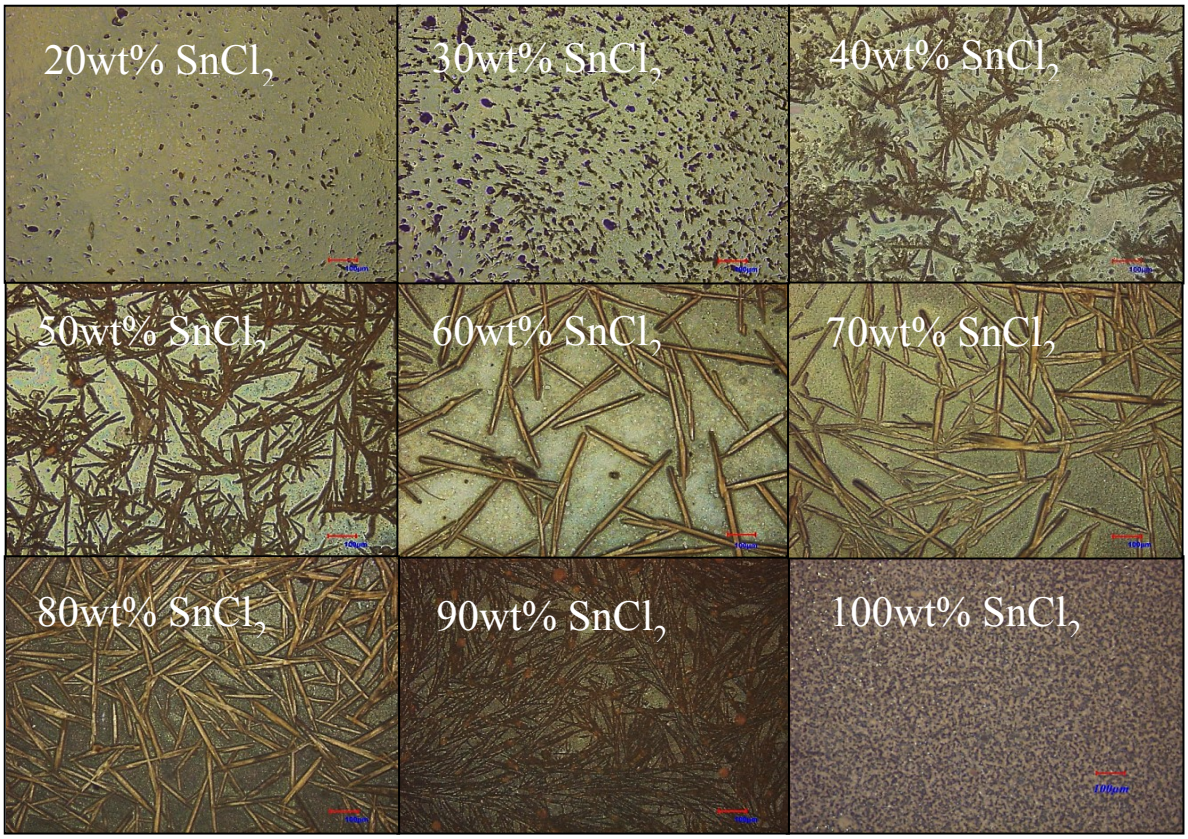


**Figure 33.** Optical micrographs of $SnCl_2$ microstrostructure captured in PyDI-5FPE polymer matrix by drop-casting from starting concentrations ranging 20-90 wt%, and of pure $SnCl_2$ drop-cast from solution on glass alone. Scale bars are all 100 μm.

Clusters and elongated crystals grown in the polymer matrix both appear to be mostly $SnCl_2$, possibly with some metallic tin and tin oxide, according to energy dispersive spectroscopy (EDS) utilizing a scanning electron microscope (SEM), X-ray diffraction (XRD), and X-ray photoemission spectroscopy (XPS). Elemental maps of particles in polymers obtained by EDS can be seen in **Figures 34**. We observe that the $SnCl_2$ additive is dispersed homogeneously within the polymer at a molecular level in addition to the secondary phase particulates at micrometer scale that are more easily

observed. EDS shows that crystals have high $SnCl_2$ content but also have some oxide presence, and that there is essentially no difference in the composition of different *structures/shapes* (clusters vs. crystals vs. pure film). Small XRD peaks can be indexed to tin metal and tin oxide, demonstrating that the obtained product is composed of multiple hybrid structures and interfaces. The polymer-grown tin structures formed in polymers exhibit very similar phases.

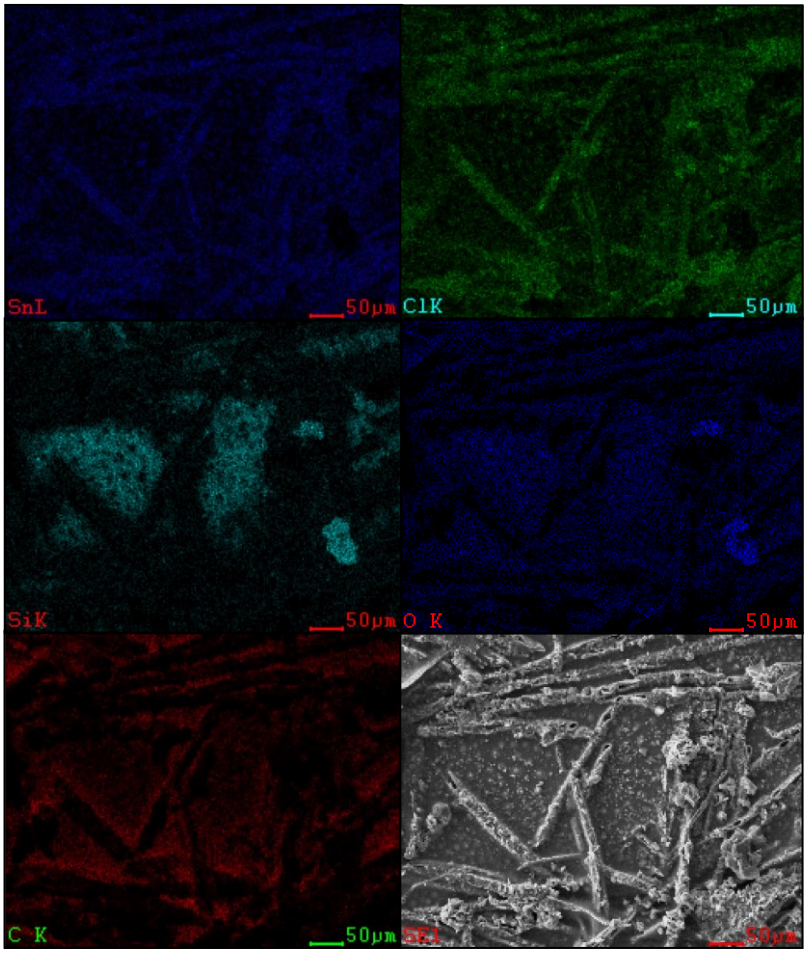


**Figure 34.** Elemental maps obtained by EDS using an SEM backscatter detector show the coverage of Sn, Cl, Si, O, and C atoms for 60wt% $SnCl_2$ in PYDI-5FPE polymer obtained by drop-casting. Bottom right is the original SEM image.

The electronic landscape of the composites can be analyzed via scanning Kelvin probe microscopy (SKPM) and Ultraviolet Photoelectron Spectroscopy (UPS). SKPM shows that the polymer chemical potential is pulled towards vacuum and $SnCl_2$ is pushed away from vacuum at the interface, which suggests that electrons accumulate in the polymer at their interface, with negative end of the interfacial dipole within the polymer. SKPM evidence that $SnCl_2$ does act as an n-dopant for our imide polymers can be seen in **Figure 35**. UPS shows that charge transfer occurs by evidence of an extra broad peak at lowest binding energy (**Figure 36**). This is a direct observation of the interfacial charge transfer and new states that lie within the polymer bandgap, where electrons generated at the polymer-inorganic interface can reach the surface and contribute to the UPS signal. XPS suggests $SnCl_2$-in-polymer has decreased work function due to a shift in tin 4d peak to lower binding energy (**Figure 37),** which is consistent with SKPM and UPS results.

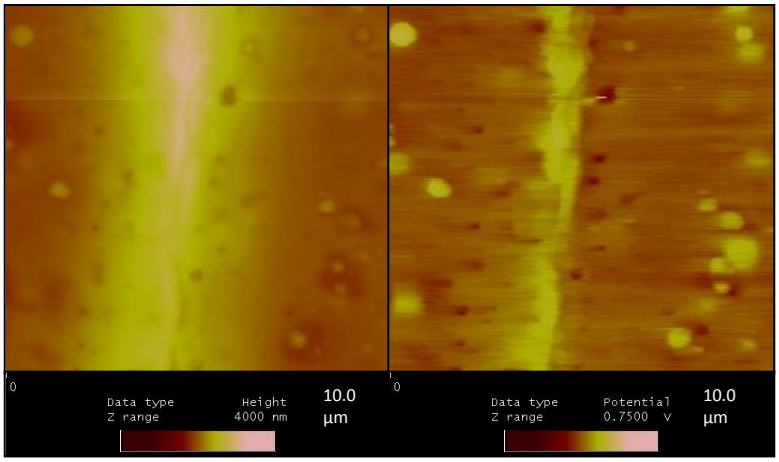


**Figure 35.** Scanning Kelvin probe microscopy measurement of tin chloride microwire captured in PyDI-5FPE polymer, left is the height measurement and right is the surface

potential, showing that the electronic states in the wire are more positive, or pushed away from the vacuum level, so electron depletion occurs in the inorganic at their interface, and electron accumulation in the polymer.

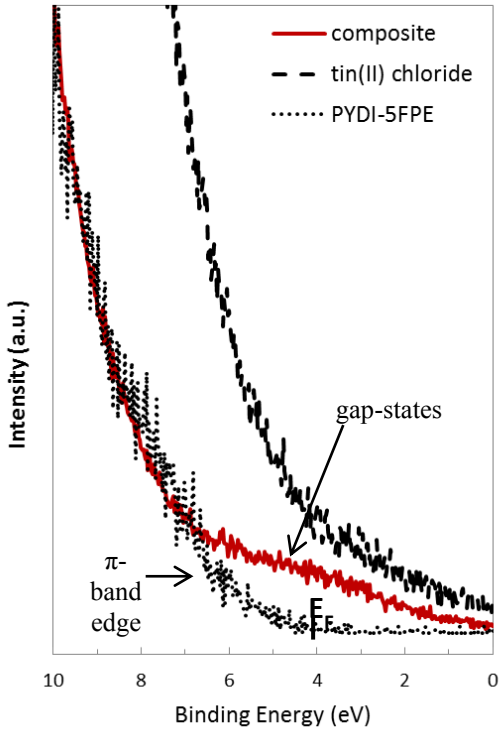


**Figure 36.** Ultraviolet photoelectron spectra of leading edge of valence band for PYDI-5FPE polymer, tin(II) chloride, and polymer composite with 60wt% $SnCl_2$.

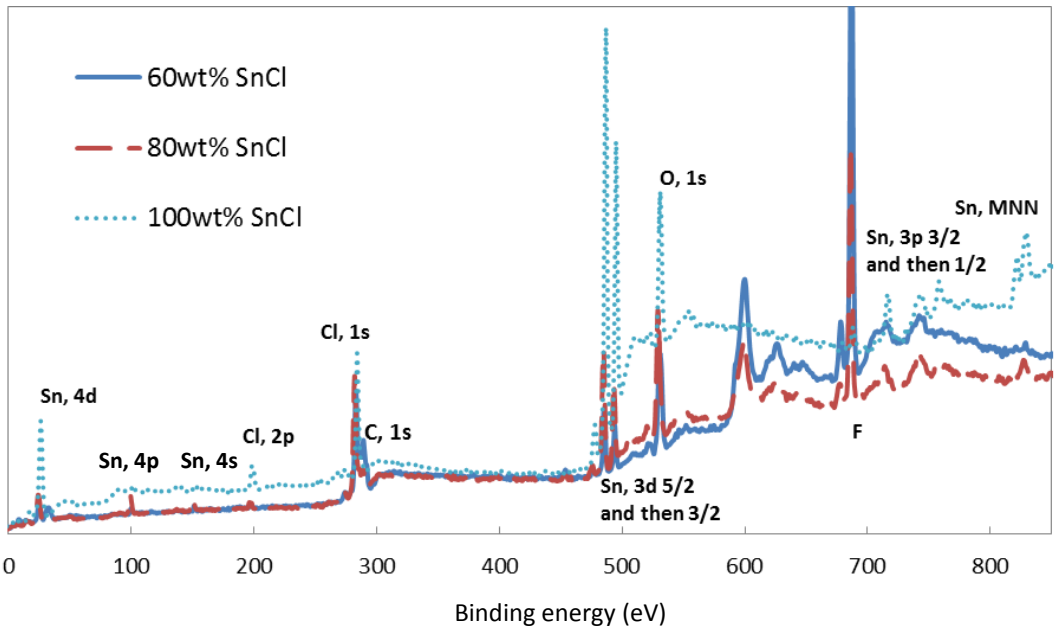


**Figure 37.** XPS of 60 and 80 wt% tin(II) chloride blended in PYDI-5FPE polymer matrix, and for pure tin(II) chloride film.

Since micro/nano inorganic crystals in polymers are generally useful materials, understanding their thermal conductivity is crucial for device heat management. We already have the results that as-grown $SnCl_2$ needles have comparable sizes and TE properties but occupy different volume fractions in the 60 to 90 wt% drop-cast samples. Their thermal conductivities and a comparison to the drop-cast microclusters and spun-cast nanoparticles is a novel investigation in itself.

Values of κ for polymers and composites were measured using the femtosecond laser-based frequency-dependent transient-thermoreflectance (TTR) method in conjunction with a multiple location and multiple spot-size sampling technique.[21] The TTR technique requires that all samples be coated with a thin layer of metal transducer. The metal transducer serves two functions: it converts the light into heat by absorbing a

fraction of the incident pump pulse and it also reflects the probe pulse according to a reflectance coefficient that is related to its own surface temperature. The TTR technique employs two laser beams: the pump beam and the probe beam. Each beam is comprised of a series of discrete, consecutive light pulses that are 12.5 ns apart. A pump pulse does the heating to the sample surface and a probe pulse comes in at a constant "delay time" after the pump pulse, which measures the surface temperature. The surface temperature will be measured as a function of the delay time between the pump pulse and the probe pulse. Knowing the thermal conductivity is the key to calculating the ZT, since it is not trivial to measure in any laboratory only the power factor is reported in many cases.

The κ we measured is 0.14 W/mK for both PyDI-5FPE and P(NDI2OD-T2) with an uncertainty of 0.02 W $m^{-1}$ $K^{-1}$ while the heat capacity is 1.40 J/$cm^3$K with an uncertainty of 0.2 J $cm^{-3}$ $K^{-1}$. The measurements on drop-cast $SnCl_2$ composites indicate that values of κ are only slightly increased relative to pristine polymers, converging on 0.2 W/mK for all compositions as the area sampled is increased to cover representative contributions from both components (**Figure 31b).** The thermal conductivity of composites depends on the volume fraction, morphology, the thermal conductivity of the polymer and the inorganic crystals, and the thermal conductance of the separating interfaces in well understood ways that apply to our systems as well.[22-24] Although the thermal conductivity of $SnCl_2$ is not available in the literature, we expect the value to be around 0.2-0.4 W/mK, as the thermal conductivity of the similar crystalline solids $ZnCl_2$ and TlCl are both below 0.5 W/mK.[25] Considering that the microstructure is relatively large, on the order of a few microns, based on the models cited,[22-24] the contribution of the interface conductance will be negligible in these composites.

**Figure 31c** shows S, σ, and PF as function of $SnCl_2$ concentration in polymer matrices PyDI-5FPE and P(NDI2OD-T2) prepared by drop-casting. The values are averages over at least 10 samples, taken from 3-5 repeated experiments, balancing statistical significance with the consideration that it takes about 1 hour for each run. PyDI-5FPE shows modest σ in its undoped form (0.00057 S/cm), and a significant S (-380 μV/K). P(NDI2OD-T2) shows greater σ (0.00124 S/cm), as expected due to higher intermolecular overlaps of diimide cores, resulting in much greater PF despite its lower intrinsic S (-280 μV/K). PFs are 0.00014 and 0.0095 $\mu W/mK^2$ for PyDI-5FPE and P(NDI2OD-T2)**,** respectively. Our PF value for the pristine P(NDI2OD-T2) is almost one tenth the value recently reported in a doped P(NDI2OD-T2) system.[26]

PFs of our hybrid composites are greater than those of any of the individual components, reaching 50 to 100 $\mu W/mK^2$ for $SnCl_2$ precursor concentrations above 50 wt% blended with PyDI-5FPE. Thus, estimating PF of 80 $\mu W/mK^2$ for 60-80 wt% $SnCl_2$, T of 300 K, and κ of 0.2 W/mK, we project ZT of 0.12. It appears that in situ microwire/nanostructure growth of $SnCl_2$ enormously increases S, and possibly σ of the polymer. S increases significantly for PyDI-5FPE with increasing concentration of $SnCl_2$, saturating around -4500 μV/K above 50 wt% $SnCl_2$. σ increases only slightly for PyDI-5FPE hybrids with low concentrations of $SnCl_2$. σ increases sharply between 30 and 50 wt% and remains constant up to 90 wt% $SnCl_2$, leveling at about 0.05 S/cm. A strong increase in conductivity appears to be correlated with overlapping of the elongated Sn-containing crystals, as they reach sufficient size to create a percolated network above 40 wt% $SnCl_2$. Utilizing P(NDI2OD-T2) as the polymer host matrix showed a similar trend as PyDI-5FPE blended with $SnCl_2$, but lower PFs closer to 10 $\mu W/mK^2$ were obtained.

Though with a much lower σ, the PFs are on par with high performance p-type hybrid composites.

**P-type Composite Hybrids**

Our results on n-polymers with inorganic additives prompt similar experiments using hole-carrying polymers PQT12 and P3HT. The weak dopant $Co(acac)_3$ will form large crystals readily in p-type polymers such as PQT12 and P3HT. We measure dramatic increases in the composite conductivity (σ, from 0.00001 to 0.001 S/cm) and a simultaneous rise in the Seebeck coefficient (S, from ~100 to >1000 μV/K) of p-type polymers with the addition of weakly oxidizing metal acetylacetonate dopant complexes. The *in situ* growth of solid secondary phase particles within polymer matrices can be observed during film formation, and a charge transfer complex (or internal dipole) develops at the polymer-particle interface, resulting in a weakly-doped composite with altered density of states. We characterized the terms in the thermoelectric power factor, PF ($S^2\sigma$), and determined fundamental behavior regarding the enhancement of PF in these hybrid composite systems as a function of additive concentration (at room temperature in air). We obtain peak power factors around 10-50 μW/mK for composites with additive concentrations of around 50-60 wt%, which we can improve by more precisely guiding the growth and distribution of secondary particles, or upon further doping with a stronger oxidizer such as F4TCNQ.

Thick films of 1-5 μm were prepared mainly from chlorobenzene mixtures of the polymers and additives in 10mg/ml solutions (using final additive concentrations ranging from 0-100 wt%) by drop-casting on glass substrates with prepatterned gold contacts (see **Figure 38**). The gold electrodes are patterned with square wells using a commercial

fluoropolymer (Novec), which allows for thick films to be made more easily by drop-casting within due to their surface energies. The films were left overnight in air covered with a petri dish in order to evaporate the solvent slowly and obtain good packing of the film. The next day, samples were placed in a vacuum-oven held under nitrogen, and temperature was slowly ramped up to 120˚C. We left the samples at 120˚C under low vacuum for 1-2 hrs and then let them cool slowly.

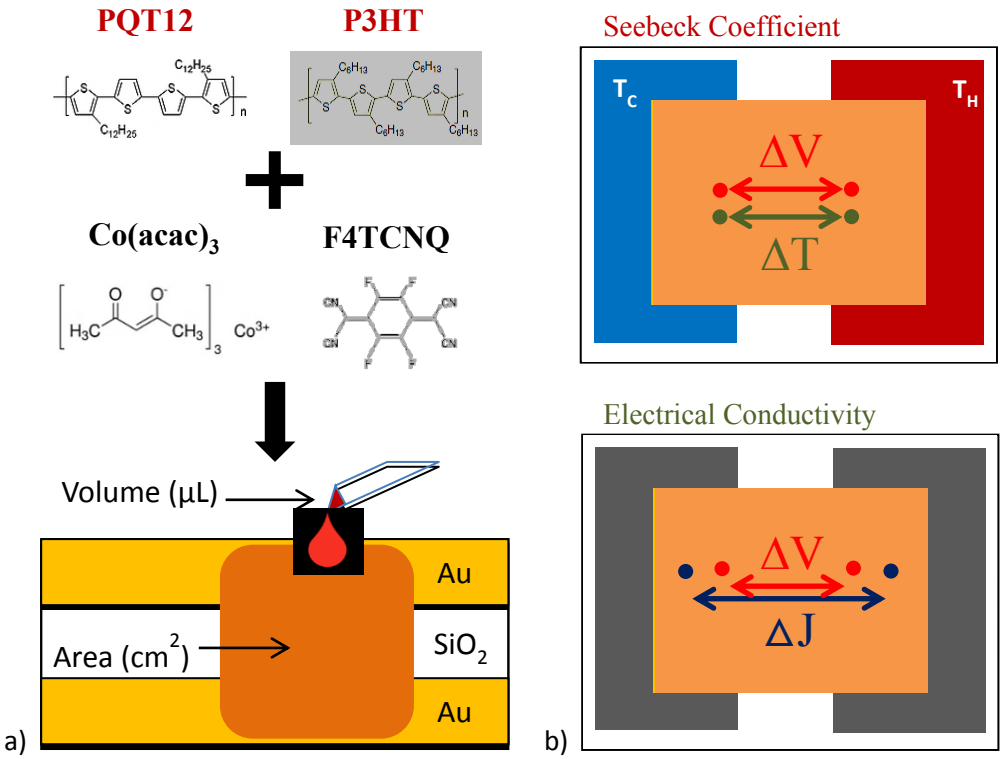


**Figure 38.** a) Chemical structures (top) and illustration for processing TE films on glass substrates with patterned gold electrodes (bottom), b) schematic for Seebeck measurement (top) and for four-probe resistance measurements (bottom).

We visually characterized the thin-film morphology using optical microscopy and measured the Seebeck coefficients and conductivities to compare behavior. **Figure 39a** shows the morphologies obtained over the range of concentrations. We used XRD to characterize the structure and crystallinity of our materials. **Figure 40** shows that pristine PQT12 has some crystallinity with shallow broad peaks. Pristine $Co(acac)_3$ produced by drop-casting on glass also shows small but sharper peaks, whereas the *in situ* grown particles have enhanced crystallinity and polymer peaks are still observed in the 60wt% $Co(acac)_3$ composite.




**Figure 39.** Optical microscope images of a) PQT12 blended with 10, 20, 40, 60, and 80 wt% cobalt(III) acetylacetonate, and of b) 60wt% $Co(acac)_3$ in PQT12 samples drop-cast using increasing amounts of solution volume per area when solution is diluted to 10mg/ml (top) or 5mg/ml (bottom). Scale bars are all 100 µm.

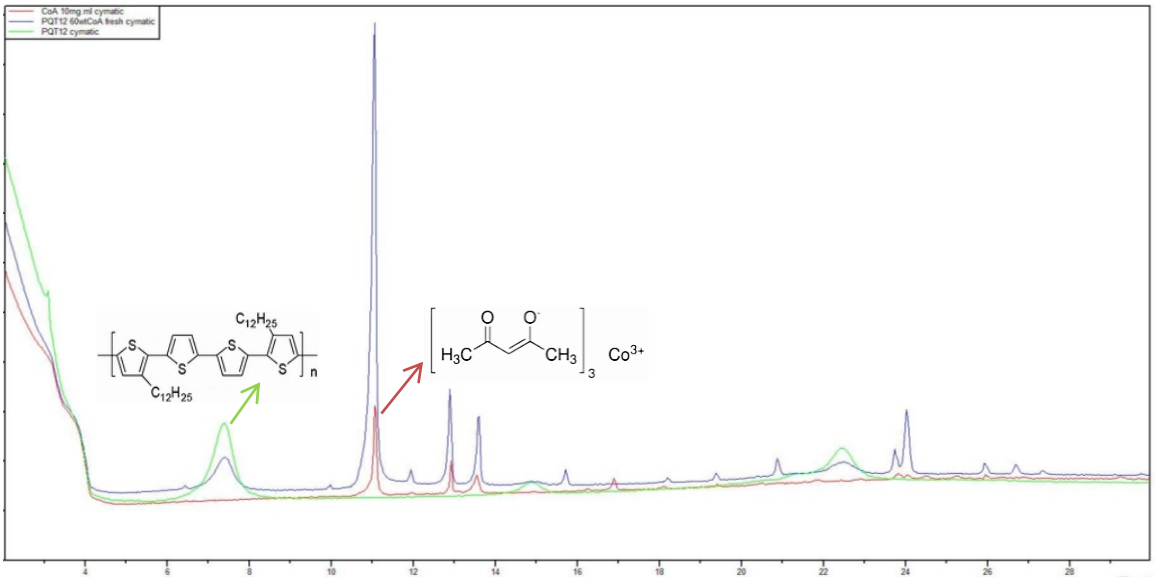


**Figure 40.** XRD for pristine PQT12 (green), pure Co(acac)3 (red), and 60wt% $Co(acac)_3$ in PQT12 (blue).

SEM was utilized to observe the particle morphology, but more importantly electron dispersive spectroscopy (EDS) was utilized in order to obtain spatial maps of the film's atomic composition. **Figure 41** shows that the particle is composed mainly of carbon and cobalt. The surrounding material is mostly carbon and sulfur, but some sulfur (attributed to the thiophenes in the polymer) clearly overlaps with the particle. EDS can probe up to 10 μm into the material, thus we cannot conclude from these images whether the polymer is coating the surface or being measured below the particle. It seems apparent from optical micrographs that the particles often break through the polymer air interface and indeed stick out up to a few μm from the polymers which are themselves a few μm thick. Profile images of composite surfaces were measured by laser optical microscopy, shown in **Figure 42**.

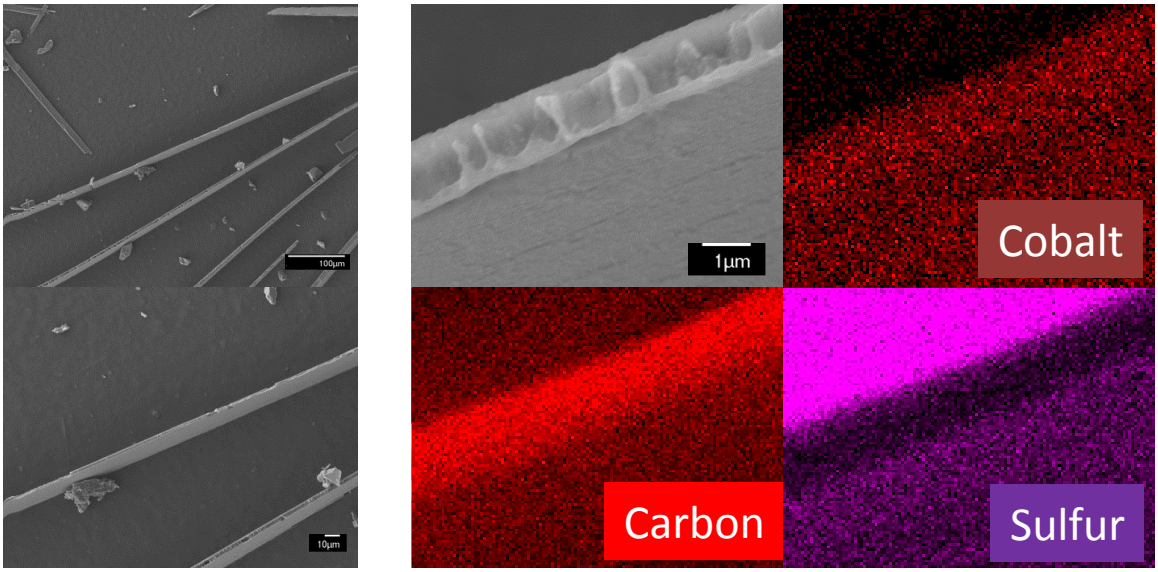


**Figure 41.** SEM images of $Co(acac)_3$ composite surface (left) and EDS compositional maps of close-up on edge of $Co(acac)_3$ particle in PQT12.

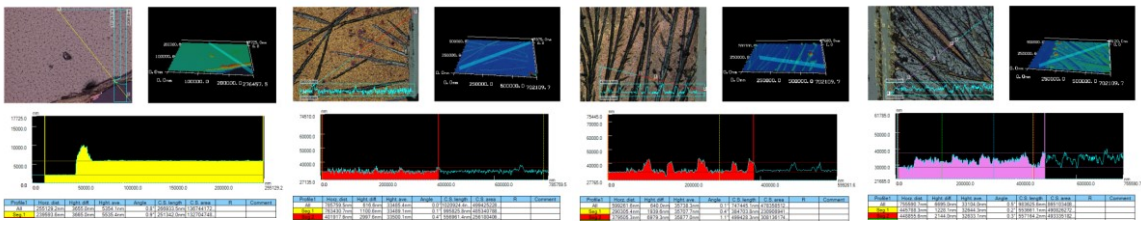

**Figure 42.** Profile images of composite surfaces were measured by laser optical microscopy for PQT12 loaded with 0wt%, 20wt%, 40wt%, and 60wt% $Co(acac)_3$ (from left to right).

**Figure 43** shows the parameters for power factor measured for PQT12 composites as a function of $Co(acac)_3$ concentration utilizing 10mg/ml chlorobenzene solutions and drop-casting 0.18 ml/cm2. To exclude contact resistance, a four-probe

method was employed to measure the electrical conductivity in air. After doping with 20wt% $Co(acac)_3$, the conductivity of PQT12 was increased up to $9.5 \times 10^{-4}$ S/cm, almost two orders of magnitude higher than those of pristine polymer films ($2.8 \times 10^{-5}$ S/cm). Seebeck was increased substantially by loading PQT12 with Co(acac)3, even for lower concentrations of 20wt% (from 114 to >2500 μV/K). Thick heterogeneous composites show practically saturated conductivity (~$4.4 \times 10^{-3}$ S/cm) and Seebeck values (~4000 μV/K) after 40wt% $Co(acac)_3$.

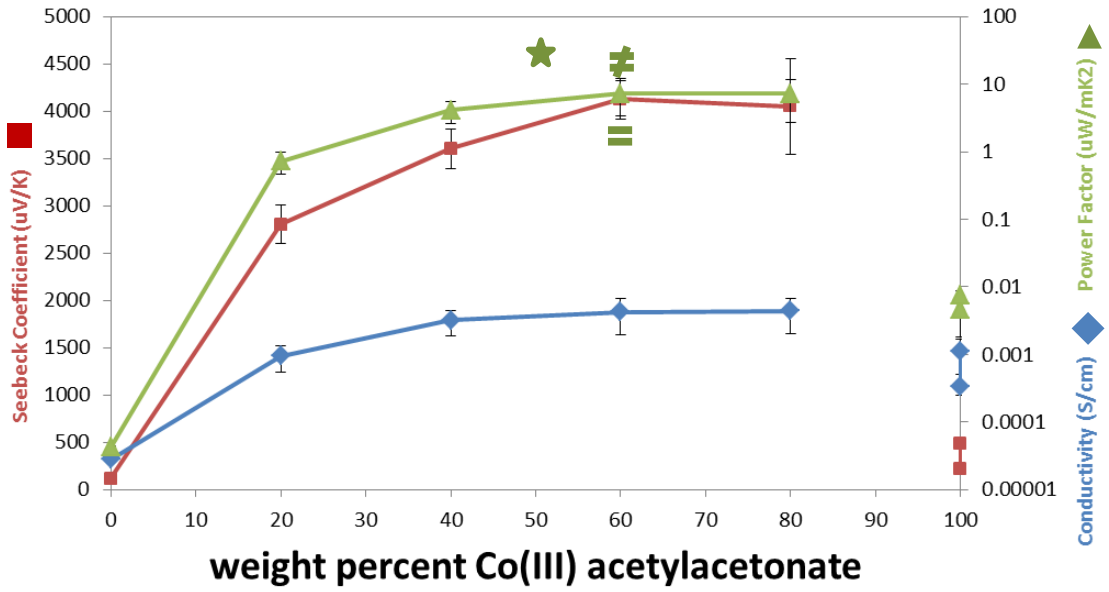


**Figure 43.** The results of S, σ, and PF plotted for PQT12 blended with $Co((acac)_3)$ as a function of dopant concentration for randomly oriented particles (solutions diluted to10 mg/ml and drop-cast using 0.18 ml/cm$^2$). Results of pure $Co(acac)_3$ are also shown (having similar results for thin-films prepared by drop-casting under vibration or by thermal evaporation). The star represents PF of 50wt% $Co(acac)_3$ samples with additional

10wt% F4TCNQ. The = and ≠ symbol represents 60wt% $Co(acac)_3$ samples with particles oriented either parallel or perpendicular to the gold electrodes, respectively.

After doping with 10 and 20% mass fraction of F4TCNQ, the conductivity of PQT12 were increased up to 0.299 S/cm in 10% mass fraction F4TCNQ samples and 0.349 S/cm for 20wt% samples. Seebeck was reduced by adding F4TCNQ, down to 35.4 μV/K for 20wt% samples. Significantly the PF of 50wt% Co $(acac)_3$ samples was raised to 47.4 $\mu W/mK^2$ with addition of 10wt% F4TCNQ, all in 40wt% PQT12.

We also ran similar experiments utilizing the standard conjugated polymer, P3HT, as another p-type thiophene-based matrix for comparison. We observe similar growth of secondary phases, as well as modest increase in S (~2500 μV/K), but having greater σ ($5.73 \times 10^{-3}$ S/cm). However, the PF for PQT12-60wt% Co(acac)3 (7.21 $\mu W/mK^2$) is similar or better in regards to TE performance for P3HT-60wt% $Co(acac)_3$ (3.44 $\mu W/mK^2$). For these reasons were more confident to continue our experiments using PQT12 and $Co(acac)_3$ as the standard system in an attempt to learn more about the secondary-phase growth as well as the observed electronic behavior.

SKPM scans across the uniaxial $Co(acac)_3$ particles in PQT12 reveal that the polymer surrounding the particle has a positive surface potential relative to the much more negative surface energy over the particle. **Figure 44** gives a representative image of both the height scan (topographical) and subsequent surface profile measurement. This observation is consistent with oxidation of the polymer by the additive and the resulting interfacial dipole, with the positive end clearly lying on the polymer side of the polymer-

particle interface. This is somewhat expected, but not obviously consistent with theory for energy band levels of isolated materials (examples shown in **Figure 45**).

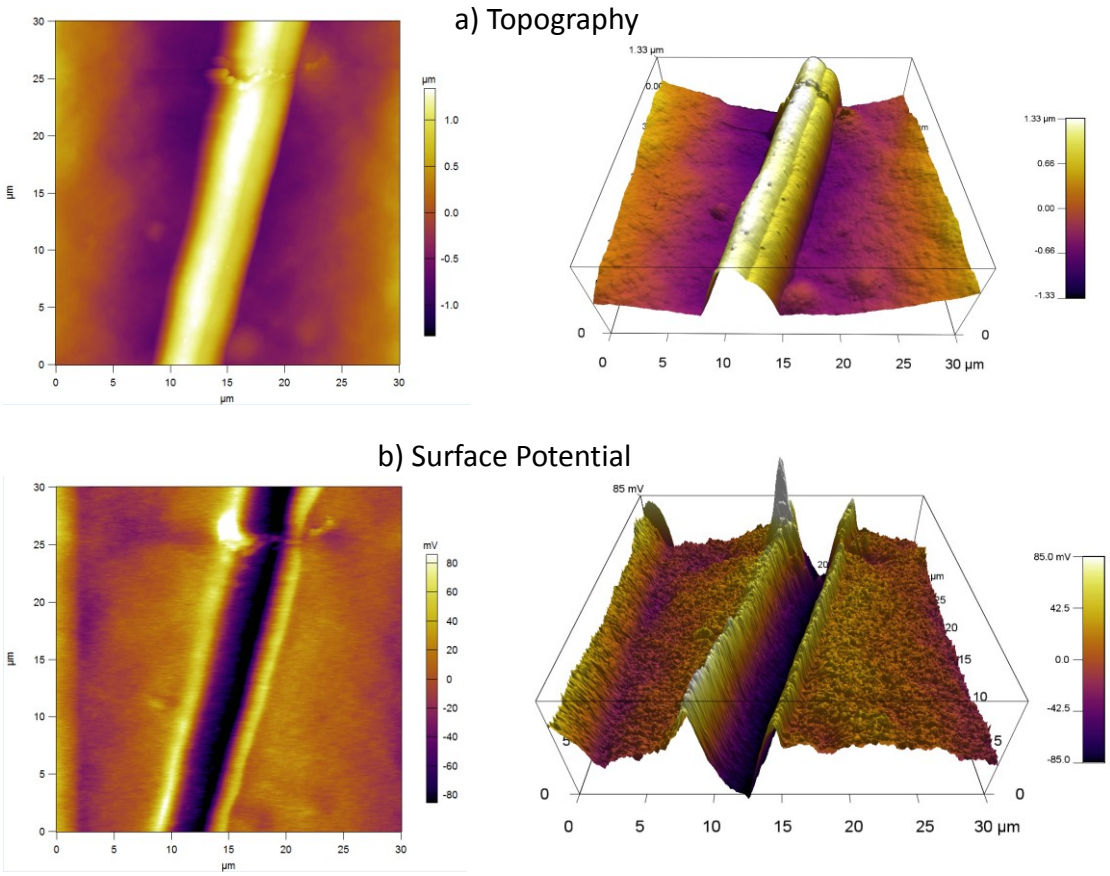


**Figure 44.** Height potential scan in 2D (top left) and 3D (top right), and the following surface potential scans also in 2D (bottom left) and 3D (bottom right).

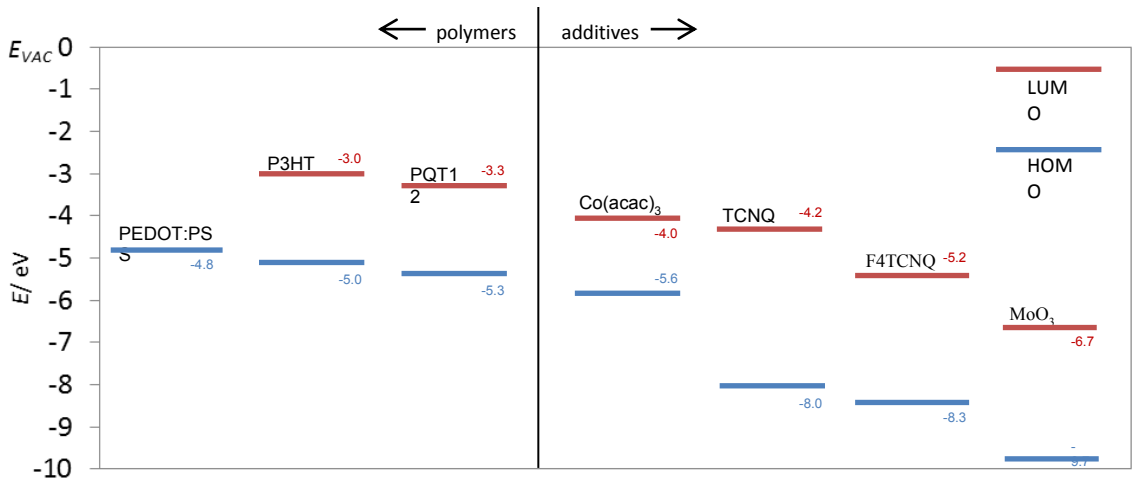


**Figure 45.** Energy levels of isolated intrinsic materials.

The *in situ* growth of solid secondary phase $Co(acac)_3$ particles within polymer matrices can be observed during film formation under optical microscope over the course of a few hours, and most phase-segregated microstructures are easily observable by eye after complete film solidification. Solvent evaporation kinetics appears to be a strong driver in the resulting morphology of drop-casted films. First we investigated possible effects of film thickness, or volume of drop-cast solution, by drop-casting incremental amounts of solution within 2D wells of the same surface area. We also investigated using more dilute solutions, such as 5 mg/ml. **Figure 39b** shows micrographs for 5 mg/ml solutions of 60wt% $Co(acac)_3$ composites as a function of amount/volume of solution drop-cast per area. The composite PFs are similar, 7.2 and 9.08 $\mu W/mK^2$, for 10 and 5 mg/ml solutions, respectively. The S and σ are more consistent/saturated for 10 mg/ml solutions over the range of thicknesses, or as the volume of solution drop-cast per area is increased from 0.05 to 0.2 $ml/cm^2$. This range of volumes drop-cast per area contains the minimum solution required to form a continuous film and the maximum amount of

solution the wells could hold before spilling over. By contrast, the 5 mg/ml solutions have Seebecks that increase with increasing volume of solution drop-cast per area by factor of more than 2, and increases by almost factor of 5. **Table 4** shows the TE parameters obtained for these devices.

**Table 4.** 60wt% Co(acac)3 in PQT12 – TE Parameters as a Function of Solution Concentration and Volume of Solution Drop-Cast per Substrate Area utilizing Chlorobenzene

| Solution Concentration | Volume of Solution per Area | Seebeck (μV/K) | Conductivity (S/cm) | PF (μW/mK$^2$) | std S | std conductivity | std PF | NoS |
|---|---|---|---|---|---|---|---|---|
| 10mg/ml | 0.05 ml/cm2 | 2750 | 0.00532 | 3.97 | 163 | 0.0019 | 1.22 | 4 |
| 10mg/ml | 0.18 ml/cm2 | 4130 | 0.00426 | 7.21 | 213 | 0.0020 | 3.85 | 6 |
| 5mg/ml | 0.05 ml/cm2 | 1740 | 0.00349 | 1.03 | 360 | 0.0013 | 0.336 | 4 |
| 5mg/ml | 0.18 ml/cm2 | 3370 | 0.00789 | 9.08 | 318 | 0.000599 | 2.33 | 4 |

Similarly, we investigated the effects of utilizing processing solvents with different volatility (THF, chlorobenzene, and dichlorobenzene). Particle morphologies depend somewhat on solvent volatility, but depend more on the amount and concentration of solution drop-cast per area, due to greater variation in processing rates and diffusion times. Films prepared by dichlorobenzene (greater boiling point) took longer to dry and there was clear evidence of zone-refinement during the polymer film formation, so that the final material to solidify is the most concentrated with $Co(acac)_3$. Therefore there was a fairly steep gradient in the concentration, which followed the

solidification wave front. The phase segregated particles had more branched or fan-like structure, as seen in **Figure 46**. Such samples performed very similarly but with slightly reduced S and σ, so slightly lower PF (5.13 μW/mK$^2$) compared to the samples casted from chlorobenzene.

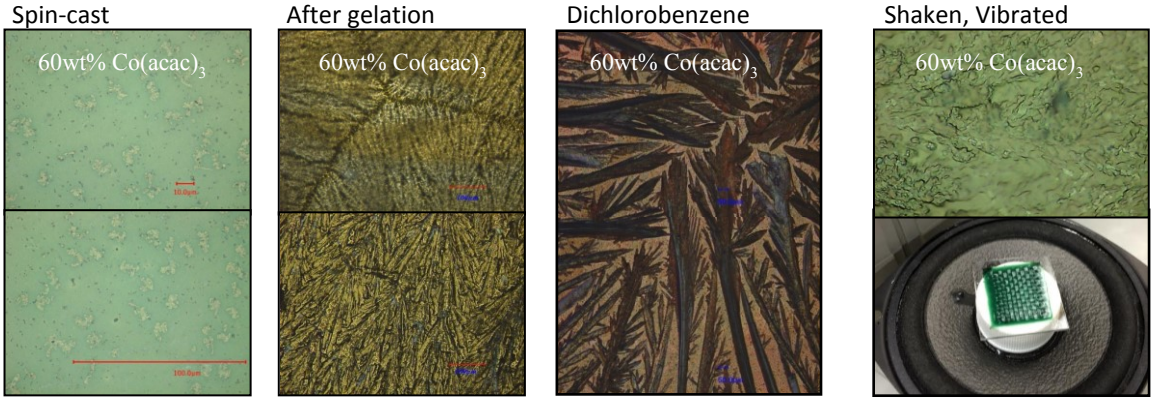


**Figure 46.** Optical micrographs of PQT12 composites containg 60wt% $Co(acac)_3$ processed via spin-casting, drop-casting of a solution aged more than one week, drop-cast utilizing dichlorobenzene, and drop-casting under vibration (from left to right). Scale bars are all 100 μm.

Films (on our scale) were more difficult to process by drop-casting using solvents with higher volatility such as chloroform or THF (less consistent film morphology and continuity, more sensitive to experimental conditions). However, higher volatility solvents may be preferable for rapid manufacturing and could lead to smaller particles if well-controlled because the solvent evaporates before particles precipitate or grow too big. A better way to achieve this may be by diluting the solution concentration from 10 to 5 mg/ml, or possibly to 1 mg/ml. These samples have slightly increased conductivity but

at a slight hit to the Seebeck. At this point, the assumption that smaller particles is preferred due to greater surface area to volume ratio is not directly observed in these systems, which may be evidenced by fabricating more homogeneous composites with greater dispersion of the additive molecule.

In order to fabricate more homogeneous PQT12-$Co(acac)_3$ composites we tried to process solutions by a relatively novel method. This involves using a speaker to vibrate the sample during drop-casting and solvent evaporation, which may help to keep the particles from precipitating and forming macro-particles. For a one centimeter square sample the substrate was vibrated using a sine wave with frequency of 160-180 Hz at sufficient volume to induce standing waves in the solution (schematic and 60wt% $Co(acac)_3$ particle morphology shown in **Figure 46**). The S for 60wt% samples drop-cast under vibration was reduced to around 1600 μV/K without the conductivity changing. Continues polycrystalline films of pristine $Co(acac)_3$ films could be made by this method using 100 mg/ml solution and drop-casting 0.2 ml/$cm^2$ while vibrating (**Figure 47b**). **Figure 47** shows various morphologies of pure $Co(acac)_3$ obtained by drop-casting under vibration or by thermally evaporating the material.

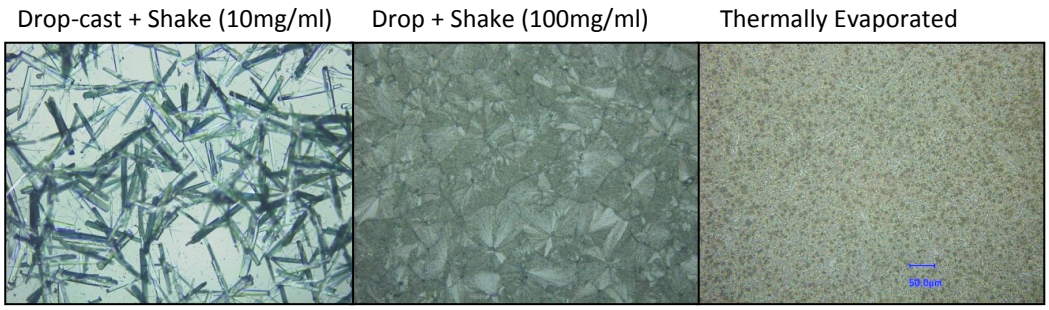


**Figure 47.** Optical micrographs showing morphologies of pure $Co(acac)_3$ obtained by drop-casting with vibration using dilute solution (left), b) drop-casting with vibration using more concentrated solution (middle), and c) thermally evaporating $Co(acac)_3$ (right). Scale bars are all 100 μm.

The growth direction of secondary phase particles within PQT12 from solution is determined by the evaporation of the solvent or the solidification wave front of the bulk film that both occur from the outside in towards the center (directly observed under microscope by taking pictures over time). For example, using square wells the crystallites grow radially inward. Knowing this we can control how crystals grow locally with respect to pre-deposited electrodes, and obtain crystals that orient all perpendicular or all parallel to the electrodes.

We further controlled the distribution and orientation of growing large uniaxial particles by exploiting geometric confinement in addition to guiding the direction of solvent evaporation with physical gradients. This method can be used to create a diversity of morphologies in a single sample prepared from one-pot solution having one mass fraction of additive (namely 60%). This method was most effective using elongated wells (rectangles) and by imposing a gradient along the long axis, suitable for high-throughput

screening to quickly find optimal composite compositions or to test ranges in the spatial distribution of second phases. The wells can then have an orientation with respect to pre-deposited gold electrodes. Without the gradient (or by using opposing gradients) we obtain homogenous morphology and concentration along the sample, but having radial orientation of crystals due to evaporation ending at the film center. **Figure 48a** and **Figure 48b** briefly illustrate the concepts behind using a sloped gravitational gradient or a temperature gradient, respectively. **Figure 48c** shows a representative sample utilizing both gradients, and the gold electrodes are parallel to the evaporation direction.

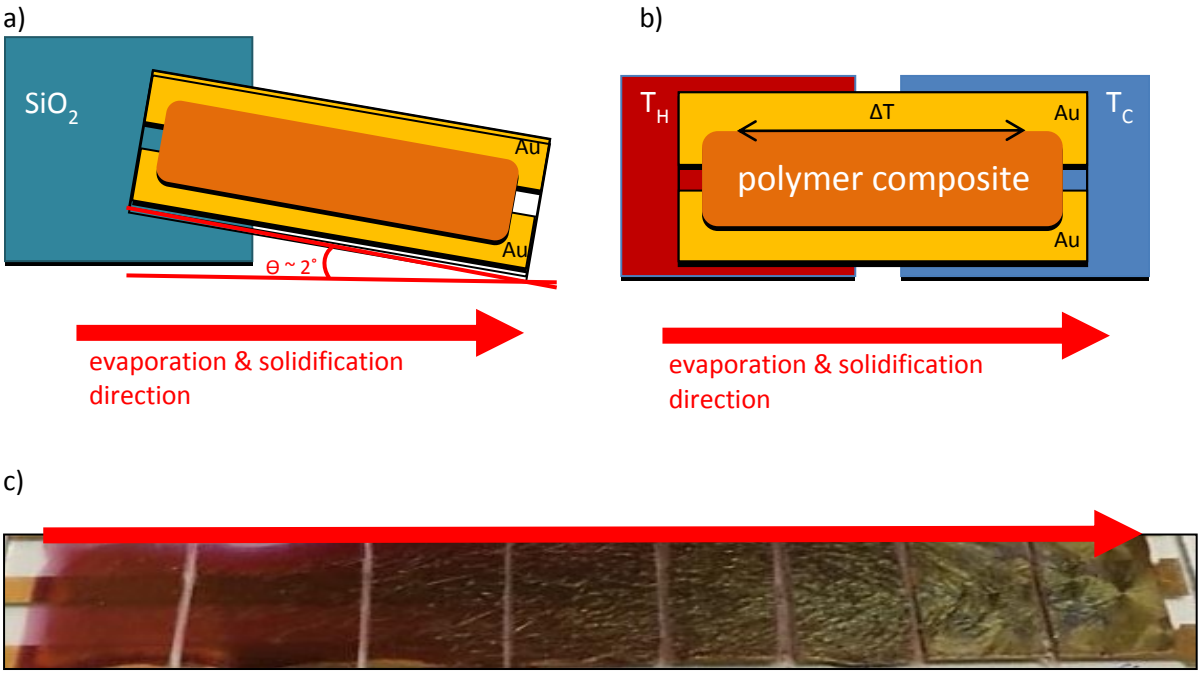


**Figure 48.** Illustrations for using an a) sloped gravitational gradient or b) a temperature gradient, and c) an image of a representative sample using both gradients constructively.

**Figure 49** shows micrographs taken along the length of a representative sloped (**49a)** and temperature gradient (**49b**) sample. Temperature gradients resulted in a greater range in distribution of particle concentrations across the sample, but particle orientations were mostly random. Samples that were sloped slightly (i.e. gravitational gradient) showed more uniform macroscopic order and differed less over the length of the sample, with crystals that grow predominately in the direction of solvent evaporation. The bulk films solidify first at either the hot side or the top of the slope, resulting in the lowest concentration of second phase component in that region due to zone refinement and smaller particle dimensions due to film thinning. A combination of the two gradients provides the ultimate range of both composition and morphology in single samples.

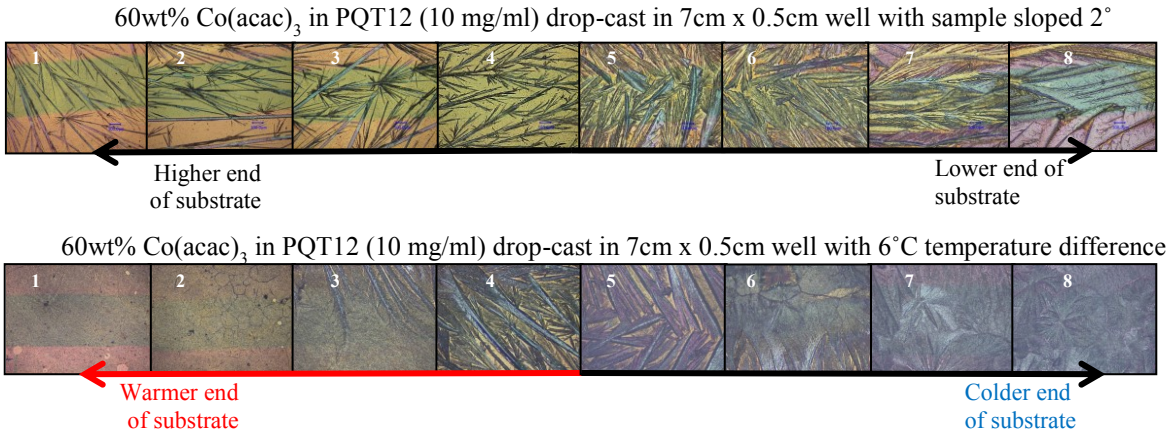


**Figure 49.** Optical micrographs taken along the length of a representative samples using sloped gradient (top row) and temperature gradient (bottom row).

The TE performance was enhanced in all cases for measurements taken along the segmented sample after processing as we measure from the high end to the low end on

the sloped samples, and from the hot end to cold end for the temperature gradient. The conductivity actually decreases slightly for the thermally graded sample from hot end to cold end, which is same trend for the sloped sample when the gold electrodes are parallel with the evaporation/solidification direction, so the resulting particles are also oriented parallel with the electrodes. In the case that the sloped sample has gold electrodes oriented perpendicular to the long axis, or evaporation direction, then the conductivity increases from high end to low end. In all cases, the S is observed to increase dramatically (from 500-1000 μV/K to 3000-4000 μV/K), and so must be dependent on thickness/morphology and/or evaporation rate. When there was no slope used, or gradients were used to oppose each other, then there was no distribution or significant change in properties along the samples. The greatest performance enhancement came from orienting uniaxial particles completely perpendicular to gold electrodes used to measure TE performance, also making them oriented parallel with the temperature gradient and direction of current (**Figure 50**). The PF can be seen in **Figure 43** for both particles oriented both parallel (=) and perpendicular (≠) with the gold electrodes, which was greatest for the perpendicular orientation (37.9 $\mu W/mK^2$). This is on par with the highest performing 50wt% $Co(acac)_3$ samples having no controlled orientation but doped with additional 10wt% F4TCNQ. The TE performances for the most pertinent examples discussed herein are compiled in **Table 5**.

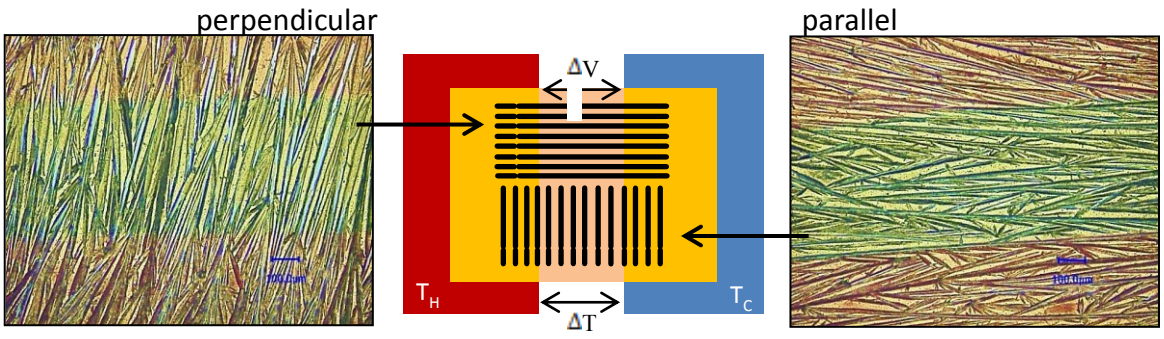


**Figure 50.** Optical micrographs for particles oriented both perpendicular (left) and parallel (right) with the gold electrodes, and schematic of their orientation during testing (middle).

**Table 5.** Comparing TE Parameters of PQT12 Composites – 10 mg/ml solutions, 0.18 ml/cm$^2$

| **Additive** | **Additive morphology** | **Seebeck (μV/K)** | **Conductivity (S/cm)** | **PF (μW/mK$^2$)** | **std S** | **std cond** | **std PF** | **NoS** |
|---|---|---|---|---|---|---|---|---|
| none | N/A | 114 | 0.000157 | 0.0002 | 20.2 | 0.0000325 | 0.0000443 | 7 |
| 60wt% $Co(acac)_3$ | radially oriented uniaxial particles | 4130 | 0.00426 | 7.21 | 213 | 0.002 | 3.85 | 6 |
| 60wt% $Co(acac)_3$ | radially oriented, drop-cast after gelation | 3530 | 0.00332 | 4.16 | 215 | 0.00109 | 1.47 | 6 |
| 60wt% $Co(acac)_3$, using dichlorobenzene | radially oriented uniaxial particles | 3900 | 0.00341 | 5.13 | 243 | 0.0018 | 2.68 | 6 |
| 60wt% $Co(acac)_3$, in P3HT | radially oriented uniaxial particles | 2540 | 0.00573 | 3.73 | 174 | 0.00148 | 1.21 | 6 |
| 60wt% $Co(acac)_3$ | uniaxial particles oriented 0 degrees to electrodes | 4470 | 0.00333 | 6.61 | 0.000213 | 0.000799 | 1.51 | 6 |
| 60wt% $Co(acac)_3$ | uniaxial particles oriented 90 degrees to electrodes | 3540 | 0.03 | 37.9 | 0.000152 | 0.00949 | 12 | 6 |
| 60wt% $Co(acac)_3$ | cymatic, partially dispersed particles | 1620 | 0.0042 | 1.18 | 179 | 0.00236 | 0.0763 | 6 |
| 60wt% $Co(acac)_3$ | spin-cast | 1400 | 0.015 | 3.43 | 109 | 0.00616 | 1.8 | 8 |
| 20wt% F4TCNQ | charge-transfer complex, mostly dispersed | 35.4 | 0.349 | 0.0468 | 1 | 0.0347 | 0.0397 | 4 |
| 10wt% F4TCNQ + 50wt% $Co(acac)_3$ | heterogenous composite, random orientation | 3340 | 0.038 | 47.4 | 290 | 0.00272 | 30 | 4 |

**References**


1. R. A. Schlitz, F. G. Brunetti, A. M. Glaudell, P. L. Miller, M. A. Brady, C. J. Takacs, C. J. Hawker, M. L. Chabinyc, *Adv. Mater.* **2014**, 26, 2825.

2. B. Russ, M. J. Robb, F. G. Brunetti, P. L. Miller, E. E. Perry, S. N. Patel, V. Ho, W. B. Chang, J. J. Urban, M. L. Chabinyc, C. J. Hawker, R. A. Segalman, *Adv. Mater.* **2014**, 26.

3. Y. Qi, S. K. Mohapatra, S. B. Kim, S. Barlow, S. R. Marder, *Appl. Phys. Lett.* **2012**, 100, 083305.

4. B. D. Naab, S. Zhang, K. Vandewal, A. Salleo, S. Barlow, S. R. Marder, and Z. Bao, *Adv. Mater.* **2014**, 26, 4268.

5. M. T. Khan, A. Kaur, S. K. Dhawan, S. Chand, *J. Appl. Phys.* **2011**, 110, 044509.

6. X. He, J. Ren, L. Wang, W. Pu, C. Jiang, C. Wan, *Ionics* **2006**, 12, 323.

7. A. Parveen, K. R. Anilkumar, S. D. Patil, A. S. Roy, *Ionics* **2013**, 19, 91.

8. S. Fayette, D.S. Smith, A. Smith, C. Martin, *J. Eur. Ceramic Soc.* **2000**, 20, 297.

9. L. Shi, Q. Hao, C. Yu, N. Mingo, X. Kong, Z.L. Wang, *Appl. Phys. Lett.* **2004**, 84, 2638.

10. V. Damodara Das, J. C. Mohanty, *J. Appl.Phys.* **1983**, 54, 977.

11. P.B. Kaul, V. Prakash, *J. Appl. Phys.***2014**, 115, 023520.

12. A. Mrotzek, D.-Y. Chung, T. Hogan, M.G. Kanatzidis, *J. Mater. Chem.* **2000**, 10, 1667.

13. L.D. Zhao, S.H. Lo, Y. Zhang, H. Sun, G. Tan, C. Uher, C. Wolverton, V. P. Dravid, M. G. Kanatzidis, *Nature* **2014**, 508, 373.

14. F. Chen, K.L. Stokes, G.S. Nolas, *J. Physics Chem. Solids* **2002**, 63, 827.

15. H. Yand, L.A. Jauregui, G. Zhang, Y.P. Chen, Y. Wu, *Nano Lett.* **2012**, 12, 540.

16 Q. Tan, J.-F. Li, *J. Electron. Mater.* 43, **2014**, 2435.

17. D. Parker, D.J. Singh, *J. Appl. Phys.* **2010**, 108, 083712.

18. M. Orihashi, Y. Noda, L.-D. Chen, T. Goto, T. Hirai, *J. Phys. Chem. Solids* **2000**, 61, 919.

19. C.M. Jaworski, V. Kulbachinskii, J.P. Heremans, *Phys. Rev. B* **2009**, 80, 233201.

20. R. M. Ireland, Y. Liu, X. Guo, Y.T. Cheng, S. Kola, W. Wang, T. Jones, R. Yang, M. Falk, H. E. Katz, *Adv. Sci.* **2015**, 2, 1500015.

21. J. Liu, J. Zhu, A. Schmidt, R.G. Yang, *Rev. Sci. Instrum*. **2013**, 84, 034902.

22. C. W. Nan, R. Birringer, D. R. Clarke, H. Gleiter, *J.Appl. Phys*. **1997**, 81, 6692.

23. J. Ordonez-Miranda, R. Yang, J.J. Alvarado-Gil, *J. Appl. Phys.* **2013**, 14, 064306.

24. L.E. Nielsen, *Industrial Eng. Chem. Fundamentals* **1974**,13, 17.

25. Y. Touloukian, E. Buyco, *Thermophysical properties of matter - the TPRC data series. Volume 5. Specific Heat - Nonmetallic Solids, Data Book*, **1970**.

26. R. A. Schlitz, F. G. Brunetti, A. M. Glaudell, P. L. Miller, M. A. Brady, C. J. Takacs, C. J. Hawker, M. L. Chabinyc, *Adv. Mater.* **2014**, 26, 2825.

**Electrostatic Gating by Corona Charging Electret Polymer**

Organic conducting polymers and their composites are under consideration for niche thermoelectric (TE) applications for room temperature cooling and power generation on the micro-scale where sufficient power is more critical than high efficiency. Their low processing cost and environmental impact combined with greater

mechanical flexibility compared to typical TE materials could allow sustainable large-scale module production for applications including localized cooling of electronic components and off-grid or battery-free power supply to wireless or mobile and medical devices, stimulating much current interest. Composites that could be designed with reduced thermal conductivity κ and usable electrical conductivity σ would lead to enhanced values of the figure of merit, $ZT = S^2\sigma T/\kappa$, where S is Seebeck coefficient and T is absolute temperature. $S^2\sigma$ is known as the power factor PF, and would be additionally increased if S can be augmented using mechanisms that do not unduly detract from σ. In this work, we demonstrate a new method for tuning S and σ applicable to flexible, standalone thermoelectric materials: the gating of TE devices electrostatically by embedding immobile charges via corona charging methods into dielectric layers overlaid onto on a polymer semiconductor prior to charging. Polymer-hosted static charge offers the combination of kinetic stability, all-solid-state configuration, and high absolute gating voltage even when the gate electrode is subsequently disconnected. S is modulated by nearly an order of magnitude. This method is applicable to situations where certain minimum values of S or σ would be required for an application.

TE properties of bulk materials have been modified in the past by using a gate electrode to induce a field-effect across a device, for both organic[1-10] and inorganic semiconductors.[11-22] A general schematic for such an experiment is shown in **Figure 51b**, except that traditionally a physical gate electrode like a metal would be deposited on top of the dielectric Novec polymer such that an electric field could be applied across the dielectric, and thus affect the transport of charges in the semiconductor. This tunability is important for specific applications where desired performance cannot be obtained by the

active material alone, or when minimum output voltages or conductivities are required, and has also resulted in important contributions to the basic understanding of the relationship between charge carrier density and the S-σ tradeoff. Batlogg measured the energy-dependent conductivity (σ) of rubrene single crystals using a transistor architecture (silicon gate, oxide and Cytop fluorinated polymer gate dielectric) and found it to be similar to that of conventional inorganic semiconductors.[1] Sirringhaus characterized a semiconducting thiophene polymer PBTTT similarly, using on-chip heating to create the temperature difference, and found gate voltage-independent and -dependent regimes for S.[2] The study was then extended to multiple organic semiconductors, both n and p, finding that gate-induced and dopant-induced charge carriers have similar effects on S. Gate modulation was also applicable to the ion-containing PEDOT-PSS using an electrochemical transistor, where again, S and σ were modulated in opposite directions via a gate electrode.[3] Gate-dependent S for pentacene decreasing at ambient and increasing at reduced temperature were stated to be a signature of hopping and band transport, respectively.[4] Photoinduced charge generation combined with temperature-dependent contact-interface-polarization have also been shown to modulate S of a polymer;[5] this may be the closest example of a permanent interfacial effect on this parameter. An example of gate effects on Seebeck with the gate still connected has been shown more recently, also illustrating that a dipolar surface can change Seebeck in a composite.[10] There are also numerous examples of gate-modulated S of inorganic and nanostructured materials.[11-22]

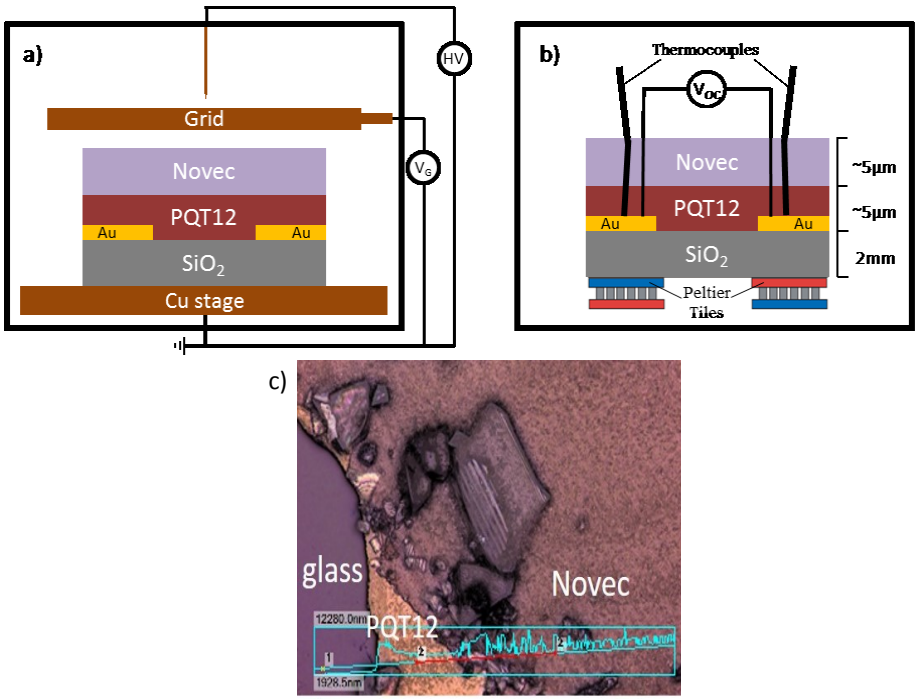


**Figure 51**. a) Corona charging utilizing high voltage power supply (HV) and a grid voltage ($V_G$) and b) measurement of Seebeck coefficient; c) micrograph and laser microscope height profile of glass, PQT12, and Novec layers.

However, the efficiency and benefits of integrating of a gate-tuned thermoelectric material would be significantly diminished if the gate electrode needed to be powered externally during operation. We have therefore strived to achieve the utility of gate tuning without active gate electrodes by employing statically charged dielectric polymers as nonvolatile gates. In this work, we take advantage of our already reported technique of applying static charge to polymers, including a polar fluorinated polymer,[23,24] or nonpolar dielectric polymers such as organosilsesquioxane resin or atactic polystyrene,[25-28] that was used to shift the threshold voltage in organic field-effect transistors, observing that embedding charges in polystyrene films produces an induced electric field affecting

charge and trap density at the dielectric-semiconductor interface, altering device performance systematically.

We focused mainly on the electret polymer "Novec 1700" (referred to as Novec, a trademark of 3M Corporation, from which the polymer is commercially available) as a charge storage polymer, and utilized poly(bisdodecylquaterthiophene) (PQT12) as the TE semiconductor material. These are sequentially drop-cast as thin films over two gold electrodes on glass. The material layers used for these experiments are shown schematically in **Figure 51** along with the configuration of the charging process (**Figure 51a**) and TE measurement (**Figure 51b**). The dielectric passivates the semiconductor while also having its top surface exposed for corona charging. A micrograph showing portions of the Novec and PQT12 peeled away from the substrate is presented in Figure 2c; height profiles as measured with a Kayence color laser microscope indicates that each polymer layer is about 4 μm thick. Static charge was applied to the upper polymer surface via a metal screen (a "grid") powered by a corona (plasma) emanating from a needle above the grid. The sample is mounted on a copper stage that is held at ground, as is a metal chamber that encloses the entire apparatus, which is never removed while the needle and grid are powered.

The surface voltage was measured using an electrostatic voltmeter (Isoprobe 279, Monroe Electronics). The electrostatic voltmeter is a surface direct current (DC) "Kelvin" voltmeter that measures surface potential in the range of ±3000 volts without physically contacting the measured surface.. We performed preliminary studies of conditions and materials that would allow the maximum static electric field to be stored in a polymer dielectric layer overlying the semiconductor. Although the above-mentioned Novec semi-

fluorinated polymer gave the best response, we also tested polystyrene, a thermally cross-linked polystyrene ("XLPS", with 10% vinylbenzocyclobutene comonomer), poly (4-chloromethyl styrene), and polyimide (Kapton, purchased from Goodfellow). Novec was supplied as a clear solution consisting mostly of fluorocarbon solvent with boiling point of 61 ˚C, but also contains 2 wt% fluoropolymer solids. Charging was carried out in the ambient atmosphere for specific time periods to determine the time evolution and maximum magnitude of deposited static voltage for each multilayer.

Our observation of polymer dielectric charging effects over time showed that charging occurs rapidly, requiring less than two minutes for maximum static voltage to be reached for a given grid potential, with most charging occurring in the first 1-30 seconds (**Figure 52**). From then on we took surface voltage measurements that resulted from imposing different grid voltages for 5 minutes. We could typically store hundreds of volts across 2-5 micron-thick drop-cast Novec films. Most of the stored charges in Novec are relatively stable at room temperature and in air. **Figure 53** shows the surface potential measured in Novec encapsulating a PQT12 device immediately after charging using 1000 V on the grid for 5 minutes, and how the surface potential decays over a matter of days. The surface potential voltage drops and saturates around a stable value that is the maximum static charge that can be stored persistently up to at least a few weeks. It might be expected that the surface potential can be maintained for longer in vacuum, but we did not notice a significant improvement by storing samples in vacuum. The stability is likely due to deep trapping of charges in the polymer by local dipolar groups or clusters, so that increased temperature, or wide temperature fluctuations, would be required to empty the traps and dissipate the charges. Charging with a grid voltage below the maximum

allowable stored charge (for a given polymer chemistry and film thickness) always resulted in a stable saturated surface potential value that does not decay with time. Decay of charges only occurs when too high a grid voltage is used, and decay occurs until saturation at some static value, so even in that case some charges can be accumulated which remain static. For all of our TE measurements we only used stable/saturated surface potentials.

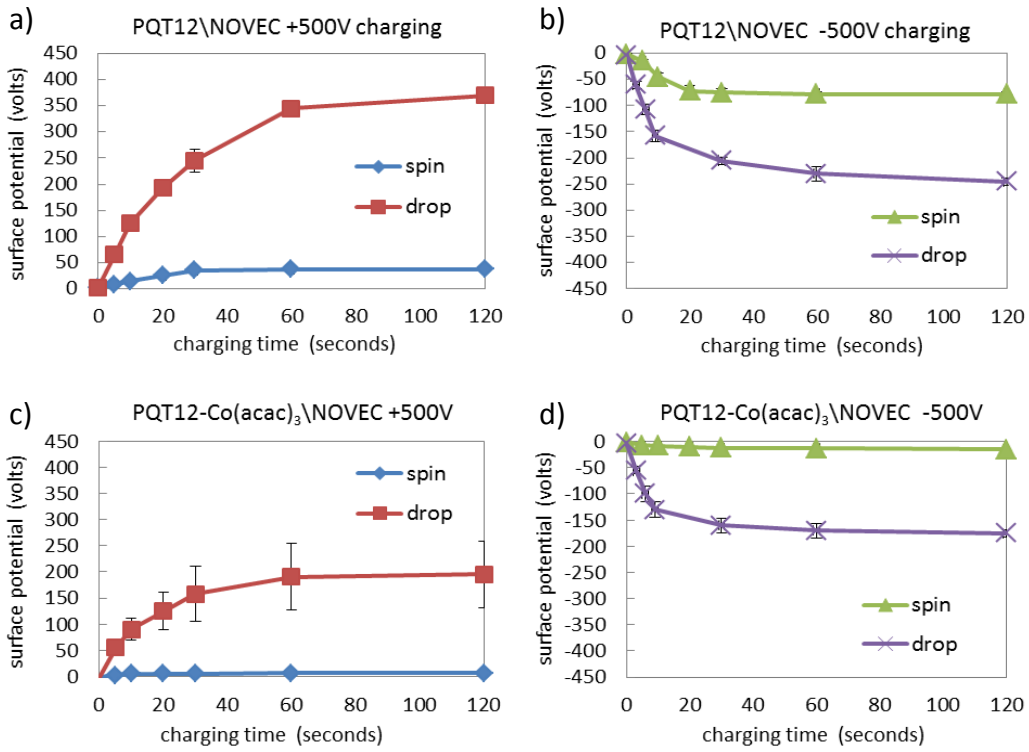


**Figure 52.** Evolution of surface potential (stored charge) in Novec as a function of charging time at single applied grid voltage of positive or negative 500 V. Spin refers to samples with Novec spin-cast on top, and drop refers to samples with Novec drop-cast on top.

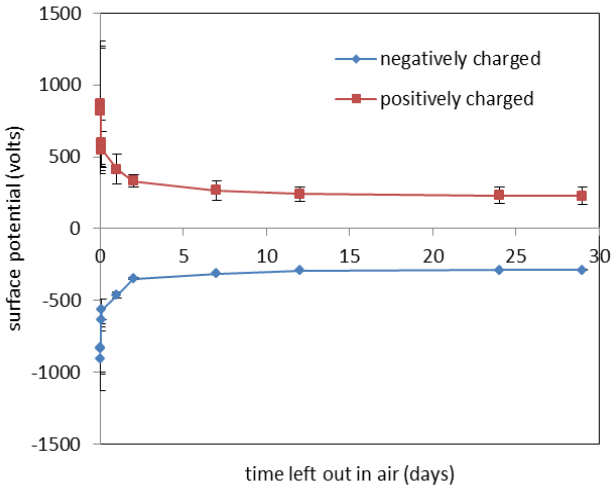


**Figure 53.** Evolution of surface potential (stored charge) in Novec film deposited over PQT12 as a function of time (days) in air (petri dish) at room temperature (about 20 ˚C). The samples were charged once using grid voltage of 1000 V applied for 5 minutes, and then all surface potential measurements were made over time, and each point is an average of two devices.

Before and after charging we measured the TE properties, S and σ, using the configuration shown schematically in **Figure 51b**. The σ value was measured by standardized four-point probe techniques. To measure S, we imposed a temperature gradient between the two gold electrodes by placing the sample over two Peltier tiles, with one hot-side up and one cold-side up, and monitored the voltage response to varying temperature differences. The Novec acts as a floating top gate because we can embed surface voltages into the film with a range of magnitudes from a few to hundreds of volts, which results in a permanently polarized device stack and affects performance in a systematic way.

**Figure 54** shows Seebeck coefficient (S), electrical conductivity, and power factor of the thiophene polymer PQT12 neat and in combination with a weak dopant cobalt(III) acetylacetonate, which forms macroscopic inclusions. This composite with uniquely grown organometallic domains was reported recently for its potential application as thermoelectric material.[29] The stronger molecular dopant F4TCNQ was also utilized in PQT12 (**Figure 55**). The data were taken with Novec corona-charged in the polarities shown, so the y-axes are plotted as a function of measured surface charge on the Novec after corona treatment. These samples were fabricated by drop-casting. Samples prepared by spin-casting the Novec layer resulted in similar trends although the maximum allowable stored charge was much more limited due to the reduced thickness of Novec. While the TE power factors change somewhat depending on the charging magnitude, the Seebeck coefficients and conductivities vary considerably, by factors of 3-10. The positive static charges pose a barrier to driving positive charges into the PQT12, while negative static charges support accumulation of holes in the semiconducting polymer. As expected, the Seebeck coefficients and conductivities show opposite dependences on stored static voltage.

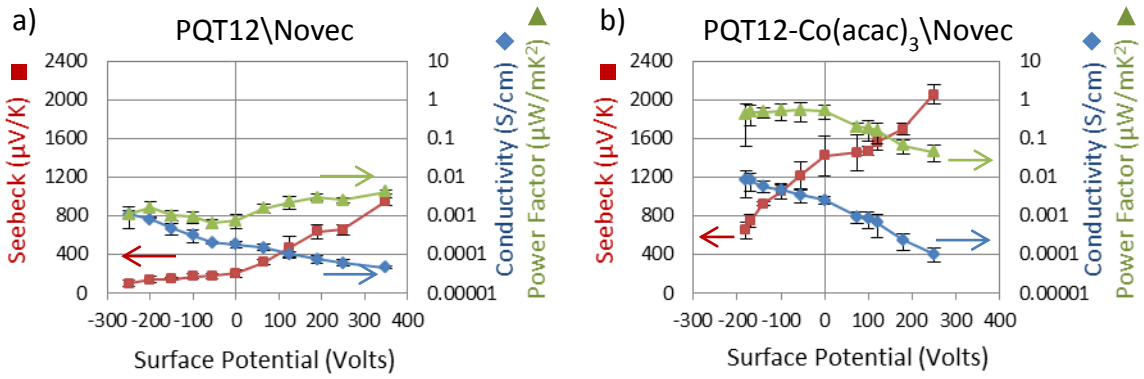


**Figure 54**. Seebeck coefficient (left y-axis, red squares), conductivity (right y-axis, blue diamonds), and power factor (right y-axis, green triangles) for composites comprising of a) PQT12 capped with Novec and b) PQT12-Co(acac)$_3$ capped with Novec, all as functions of the stored surface potential in Novec (x-axis).

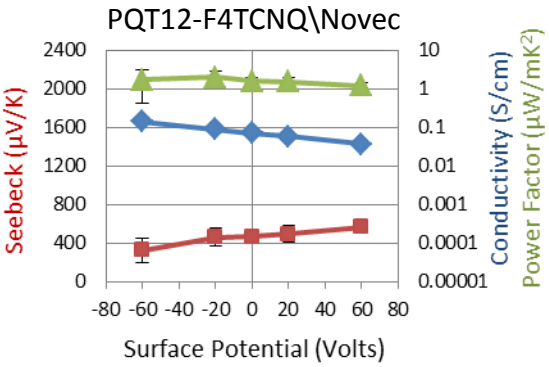


**Figure 55.** Seebck coefficient (left y-axis, red squares), conductivity (right y-axis, blue diamonds), and power factor (right y-axis, green triangles) for composites comprising of PQT12 having 10 wt% F4TCNQ and then capped with Novec, all as functions of the stored surface potential in Novec (x-axis).

The Novec is working as a charge-storing dielectric, where negative charge injected into the Novec is stabilizing holes induced in the PQT12. The polarity we observe is consistent with the formation of a dipole, with one pole in the dielectric and the other pole in the semiconducting composite. The polarization applies to the entire device stack, not the Novec alone. The compensation of charge in the Novec appears in the semiconducting hole-transport polymer, so the dipole is across the dielectric-semiconductor interface.

This would be opposite to the usual transistor bias stress mechanism where, for example, negative charge in the dielectric creates traps for holes in a p-channel semiconductor and increases threshold voltage into accumulation. This "charge trapping" mechanism of bias stress puts charges into the dielectric that cancel some of the gate voltage or extended electric field. More generally, the effect of either on-state or off-state bias stress (voltage applied for an extended time to a gate dielectric) can be to move transistor threshold voltages into either accumulation or depletion, depending on whether the main effect is to trap surface charges near the semiconductor interface or to polarize the dielectric itself with respect to the semiconductor. With transistors, the turn-on voltage is evaluated after charges can be re-equilibrated with an external circuit. By contrast, in our present thermoelectric characterization experiments, the charge distribution after the corona charging process stops is fixed under open circuit conditions, so compensating charges in the polymer semiconductor remain there.

The fact that some initial stored charge dissipates over minutes to 1-2 hours before stabilizing is a reflection that charges are stored in traps of varying depths. Also, some surface charges may be compensated, or neutralized, by chemical species in the air.

Assuming that the maximum grid voltage allowable without breakdown is applied for a given dielectric film thickness, the chemical properties and thermal stability of the polymer and the substrate or charging circuit configuration all govern the magnitude of the final stored charge. The magnitude and permanence of the static charges depends most on how strongly they are trapped by electropositive and/or electronegative local structures, and the density of those structures.

Typically, we only consider dielectric materials for surface charging or polarization, because a conductor would dissipate the charges being added or quickly balance the induced polarization. Even so, we also tried charging the semiconducting polymer directly, but as expected, the charges dissipate very easily from the semiconductor in air and at room temperature (over minutes or hours), saturating at fairly low voltages (few or tens of volts). Charges stored in the semiconductor are not stable and the charges can be observed to be dissipating during Kelvin probe monitoring in real time. The resulting final static charge left in those samples may actually be a few volts of stored charge in the glass substrate. This experiment supports our hypothesis that even though the glass substrate is formally in series with the polymer layers, the grid, and the ground plate, it is the top polymer surface being bombarded with charges of a specific polarity that appears to dominate the charging process, and it is even possible that the underlying semiconducting polymer becomes effectively grounded while an overlying dielectric is charged. The fact that different polymers show different charge storage capabilities also supports this hypothesis.

Because of our interest in flexible thermoelectric devices, we also considered the possibility that a dielectric polymer surface could be both charged and used as the

supporting substrate for a thermoelectric polymer. We deposited XLPS on a glass surface, corona charged it, and then deposited PQT12. We observed substantial effects due to the charging, providing evidence for modulating activity of static charge at the semiconductor-dielectric interface. The device structure, charging behavior, and thermoelectric response to charging are shown in **Figure 56**. Of course, it would still be possible to use one insulating polymer as a substrate material and apply a different dielectric polymer overlayer for corona charging. In a related experiment toward a different application, our group recently developed an organic field-effect transistor-based sensor made from printable materials using a polyethylene terephthalate (PET) substrate and PQT12 or DPP-CN as the active p-type or n-type semiconductor, respectively.[28] The transistor device was simplified by replacing the gate electrode and dielectric deposition steps with the introduction of static charges on the back surface of the PET substrate by corona charging to form a static gate, reducing the transistor architecture to a chemiresistor.

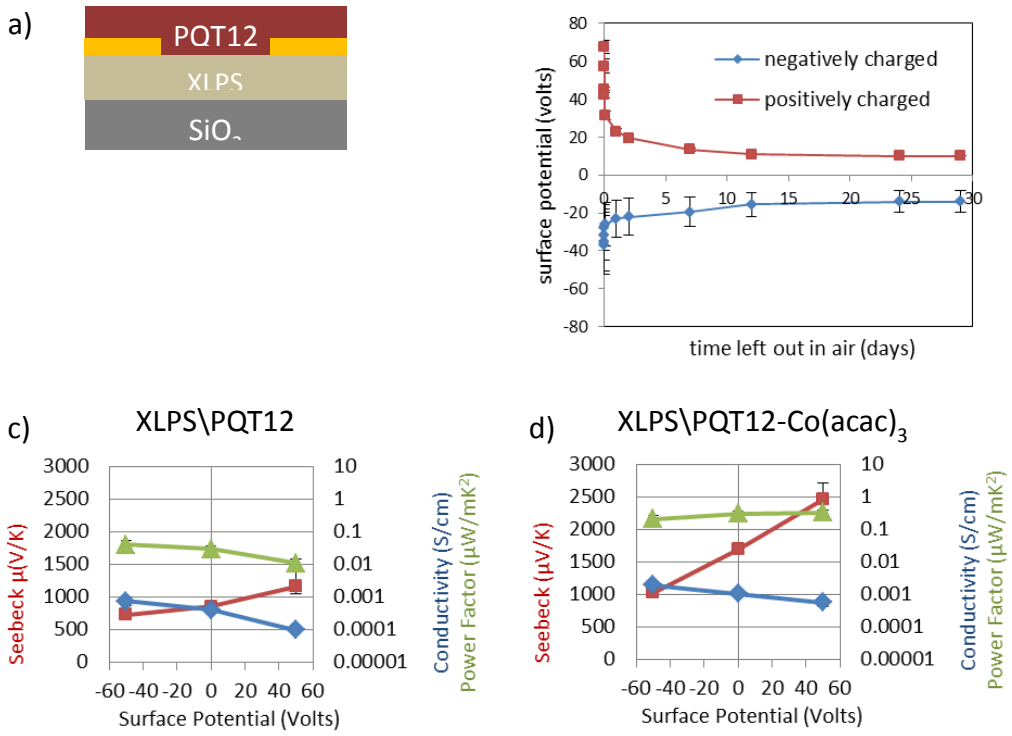


**Figure 56.** a) Schematic image of side view for device structure using cross-linked polystyrene (XLPS) and b) evolution of surface potential (stored charge) in XLPS film without PQT12 deposited on top, as a function of time (days) in air (petri dish) at room temperature (about 20 ˚C). The samples were charged once using grid voltage of 1000 V applied for 5 minutes, and then all surface potential measurements were made over time, and each point is an average of two devices. Plots are shown for Seebeck coefficient (left y-axis, red squares), conductivity (right y-axis, blue diamonds), and power factor (right y-axis, green triangles) for bilayers comprising of c) PQT12 over XLPS and d) PQT12-$Co(acac)_3$ over XLPS, all as functions of the stored surface potential in Novec (x-axis) as an average of four devices each. Each surface potential value used for each data point is what was measured immediately after charging and before drop-casting PQT12, which may help to further stabilize the static charge in air.

**References**


1. K. P Pernstich, B. Rossner, B. Batlogg, *Nature Mater.* **2008,** *7*, 4, 321-325.

2. D. Venkateshvaran, A. J. Kronemeijer, J. Moriarty, D. Emin, H. Sirringhaus, *Appl. Mater.* **2014,** *2*, 3.

3. O. Bubnova, M. Berggren, X. Crispin, *J. Amer. Chem. Soc.* **2012,** *134,* 40, 16456-16459.

4. W. C. Germs, K. Guo, R. A. J. Janssen, M. Kemerink, *Phys. Rev. Lett.* **2012,** 109 ,1.

5. D. H. Hu, Q. Liu, J. Tisdale, T. Lei, J. Pei, H. Wang, A. Urbas, B. Hu, *ACS Nano* **2015,** *9*, 5, 5208-5213.

6. V. Bharti, Y. Bar-Cohen, Z.Y. Cheng, Q. Zhang, J. Madden, *Mater. Res. Soc. Symp. Proc.* **2006,** 889, 241-255.

7. J. P. Small, K. M. Perez, P. Kim, *Phys. Rev. Lett.* **2003,** 91, 256801.

8. C. R. Wang, W. S. Lu, L. Hao, W. L. Lee, T. K. Lee, F. Lin, I. C. Cheng, J. Z. Chen, *Phys. Rev. Lett.* **2011,** *107*, 18.

9. F. Zhang, Y. Zang, D. Huang, C. Di, X. Gao, H. Sirringhaus, D. Zhu, *Adv. Funt. Mater.* **2015,** 1-9.

10. N. Lu, L. Li, W. Banerjee, M. Liu, *Org. Elect.* **2016**, 29, 27-32.

11. I. Bejenari, V. Kantser, A. A. Balandin, .*Phys. Rev. B* **2010,** *81*, 7.

12. B. M. Curtin, E. A. Codecido, S. Kramer, J. E. Bowers, *Nano Lett.* **2013,** *13*, 11, 5503-5508.

13. W. J. Liang, A. I. Hochbaum, M. Fardy, O. Rabin, M. J. Zhang, P. D. Yang, *Nano Lett.* **2009,** *9*, 4, 1689-1693.

14. N. D. Lu, L. Li, P. X. Sun, W. Banerjee, M. Liu, *J. Appl. Phys.* **2014,** *116,* 10.

15. N. Neophytou, H. Kosina, *Appl. Phys. Lett.* **2014,** *105,* 7.

16. N. Neophytou, H. Karamitaheri, H. Kosina, *J. Elect. Mater.* **2015,** *44*, 6, 1599-1605.

17. H. Ohta, *J. Mater. Sci.* **2013,** *48*, 7, 2797-2805.

18. H. Ohta, Y. Masuoka, R. Asahi, T. Kato, Y. Ikuhara, K. Nomura, H. Hosono, *Appl. Phys. Lett.* **2009,** *95*, 11.

19. S. Roddaro, D. Ercolani, M. A. Safeen, S. Suomalainen, F. Rossella, F. Giazotto, L. Sorba, F. Beltram, *Nano Lett.* **2013,** *13*, 8, 3638-3642.

20. A. Yoshikawa, K. Uchida, K. Koumoto, T. Kato, Y. Ikuhara, H. Ohta, *Appl. Phys. Express* **2009,** *2*, 12.

21. R.Takayanagi, T. Fujii, A. Asamitsu, *Appl. Phys. Express* **2015,** *8*, 5.

22. K. Yanagi, S. Kanda, Y. Oshima, Y. Kitamura, H. Kawai, T. Yamamoto, T. Takenobu, Y. Nakai, Y. Maniwa, *Nano Lett.* **2014,** *14,* 11, 6437-6442.

23. K. Reuter, H. Kempa, K.D. Deshmukh, H E. Katz, A.C. Hubler, *Org. Elect.* **2010,** 95–99.

24. K.D. Deshmukh, K. Reuter, H. Kempa, J. E. West, H. E.; Katz, *Appl. Phys. Lett.* **2009,** 95, 113307.

25. C. Huang, H. E. Katz, J. E. West, *J. Appl. Phys*. **2006,** 100.

26. C. Huang, J. E. West, H. E.; Katz, *Adv. Funct. Mater.* **2007,** *17*, 142–153.

27. M. Scharnberg, V. Zaporojtchenko, R. Adelung, F. Faupel, C. Pannemann, T. Diekmann, U. Hilleringmann, *Appl. Phys. Lett.* **2007,** 90, 013501.

28. K. Besar, S. Yang, X. Guo, W. Huang, A. M. Rule, P. N. Breysse, I. J. Kymissis, H. E. Katz, E. He, *Org. Elect.* **2014**, 15, 3221-3230.

29. R. M. Ireland, Y. Liu, X. Guo, Y.T. Cheng, S. Kola, W. Wang, T. Jones, R. Yang, M. Falk, H. E. Katz, *Adv. Sci.* **2015**, 2, 1500015.

# Chapter 5

# Conclusions

## Summary & Future Work

We have fabricated multilayer top-contact FETs utilizing Te in conjunction with OSCs, focusing on thiophene- and phenyl-based molecules, and self-assembling monolayers, observing morphological, mobility, and switching effects of the various interfaces. We demonstrated bilayer and trilayer heterojunction transistors utilizing vertically stacked thin films of tellurium and small OSC molecules. All of the samples can be further combined with conventional gating experiments using an electret polymer to extend or modify the electric field bias throughout the devices. The chief advantage of this new, combined material system is the ability to investigate fundamental scientific concepts while also developing unique high performance devices. Time-resolved current-voltage measurements help model charge distribution and explain possible current or frequency limiting phenomena. Best of all, tellurium and OSCs are easily deposited as nanometer thick films using simple low-energy processing, such as thermal evaporation under moderate vacuum conditions leading to reliable polycrystalline films. Solution methods could also be feasible.

We find that OSC-Te heterojunctions have promising potential for high hole mobility, current-limiting, frequency-filtering, and thermoelectric applications. Taking all the observations together, various surfaces can lead to Te films with either excellent percolation and high hole mobility or poorly connected nanowires with little hole mobility under similar growth conditions. Conceivably, multi-device circuitry could

be fabricated using just a single Te deposition on a patterned organic substrate, using the great region-to-region differences in Te morphology and mobility to tune semiconductor function.

Moreover, OSC layers could serve as an ideal capping layer for realizing topological insulator behavior in bismuth selenide because they not only reduce the carrier density but also protect samples from degrading reaction with the atmosphere. Such layers are potentially very configurable as they can be partially removed by acetone without decreasing the mobility in order to provide contact areas for ferromagnetic[1] or superconducting[2] leads for future spintronics and quantum computing applications. Patterning of these bulk-insulating topological insulators may allow the realization of spin plasmons and enable a next generation of low-dissipation plasmonic devices.[3] These samples can also be further combined with conventional gating experiments to tune the chemical potential further past the Dirac point by depositing charged dielectric layers directly on top the charge extracting OSC layers. Furthermore, self-assembling molecules, having a strong dipole moment and probably thiol functional groups, could be used to create an additional internal bias layer that favors charge extraction at across the heterojunction interface.

Our use of a novel unipolar n-type polymer and inorganic additives has led to the first demonstration of $ZT > 0.1$ in electron-carrying polymer composites that contain neither highly toxic nor rare elements. *In situ* fabrication of inorganic particles within the polymer matrix is advantageous because of simpler preparation and improved interfacial interactions,[4] and potentially enhanced morphological structure.[5] Leveraging recent advances in n-polymer doping, we anticipate equivalent power factors from both

composite polarities to be achievable in the near future. The results presented for electrostatic gating of thermoelectric PQT12 and polymer-composites constitutes the first demonstration of gate voltage modulation of thermoelectric parameters where the gate electrode itself is not connected to or operated with the thermoelectric device. The electrostatic charging method for creating nonvolatile gates over thermoelectric materials could facilitate simple accommodation of both p- and n-type legs, having optimized matching ZT values, in order to make a complete and maximally efficient power-generating device.

The platform described above offers numerous opportunities to increase ZT further. S and σ can increase simultaneously in our composites because of the inorganic compound introducing some new filled states to the polymer besides having some conductivity itself. Simple additions of n-doping elements such as sulfur and aluminum to $SnCl_2$ should increase σ. This should not result in accompanying increase in κ because we would remain in the phonon thermal conductivity-dominated regime. Although microcomposites are generally less homogeneous compared to nanocomposites, they may have greater conductivity because larger inclusions may have greater carrier mobilities due to longer mean-free path distances. Nanostructuring increases surface area to volume ratio greatly and reduces phononic thermal conductivity, but at cost of greater series contact resistances,[6] Smaller nano-scale dopants can also have high tendency to diffuse in organic systems, leading to detrimental instability.[7] Growth of precise nanostructures will increase S and σ while decreasing κ further if it allows maximum interface phonon scattering while maximizing doping and transport pathways. The control of particle growth (i.e. growth rates, crystal structure and orientation, and particle alignment)

leading to optimized power factors and reduced phononic thermal conductivity would be essential for further increases in composite ZT.

**References**


1. C. H. Li, O. M. J. van't Erve, J. T. Robinson, Y. Liu, L. Li, B. T. Jonker, *Nature Nanotechnology* **2015**, 9, 218-224.

7. M. Veldhorst, M. Snelder, M. Hoek, T. Gang, V. K. Guduru, X. L. Wang, U. Zeitler, *Nature Mater.* **2012**, 11, 417-421.

3. Y. Okada, V. Madhavan, *Nature Nanotechnology* **2013**, 8, 541.

4. M. T. Khan, A. Kaur, S. K. Dhawan, S. Chand, *J. Appl. Phys.* **2011**, 110, 044509.

5. N. E. Coates, S. K. Yee, B. McCulloch, K. C. See, A. Majumdar, R. A. Segalman, J. J. Urban, Adv. Mater. **2013**, 25, 1629.

6.` B. Zhang, J. Sun, H. E. Katz, F. Fang, R .L. Opila, *ACS Appl. Mater. Interf.* **2010**, 2, 3170.

7. M. L. Tietze, F. Wolzl, T. Menke, A. Fischer, M Riede, K. Leo, B. Lussem, *Physica Status Solidi A* **2013**, 210, 2188.

## Bibliography – Robert Matthew Ireland

In Dr. Howard Katz's organic electronic materials research laboratory at Johns Hopkins, Robert focused mainly on micro- and nano-structured hybrid semiconductors. These devices are crucial to the development of mass produced, low power displays and energy conversion platforms. Robert's research has been in three major areas. First, he contributed to research on dipolar monolayers inserted between field-effect transistor gate dielectrics and organic semiconductors, which could be applicable as pixel switches in transparent displays. He showed that the work functions of the dielectrics change markedly as a result of the attached monolayers, shifting the voltages at which the transistors switch on, and in some cases even changing the majority carrier in the semiconductors.

Second, he explored interfaces between chalcogenide semiconductors and organic semiconductors, demonstrating that the charge densities in the chalcogenides can be modulated by electric fields arising from interface dipoles between the two materials. This allowed the widening of the voltage interval in which the high-carrier-mobility elemental tellurium semiconductor could show a field effect in transistor architectures. He used a laser patterning technique in collaboration with a corporate research group to verify that these effects were not the result of parasitic currents around the devices. Furthermore, Robert performed frequency-dependence experiments on the transistors, showing that the apparent mobilities measured in the devices vary according to the equilibration time allowed for the charge channels, an effect that is generally neglected in the study of alternative semiconductors. The results also stimulated a new project involving modulation of carrier concentration in topological insulator interfaces that was

recently funded by NSF.

Most recently, Robert has become one of the leading drivers of hybrid thermoelectric materials research in the world. He discovered that combinations of electron-carrying polymers based on polyimides with simple, common-element inorganic inclusions show the highest power factors ever recorded for solution-deposited, flexible thermoelectric films. Once again, he devised ingenious growth methods for the inorganic inclusions and measured the dynamic electronic properties and interfacial voltages characteristic of the material interfaces. For these efforts Robert was awarded the 2015 Materials Research Society Graduate Student Award.

These discoveries were made with little supervision from his advisor, and involved Robert making his own connections with student collaborators and professors outside of the department, even outside the university, learning the necessary techniques, and managing experiment schedules around the availability of starting materials provided by other research groups and instrumentation that is in heavy demand. Robert also has considerable accomplishments in teaching and mentoring activities. He was one of the most enthusiastic participants in a fifth grade science after-school outreach activity in a Baltimore City public school. In addition, He spent three summers mentoring local High School students, and guided two undergraduate students through student design projects. Robert was one of four advanced graduates selected for the Hopkins Engineering Applications & Research Tutorials pilot program, where he independently designed and taught an undergraduate course for one-credit based around his research area. A selected comment from the course evaluations includes: “Be prepared to fall in love with materials science after you take this class.”

# Curriculum Vitae – Robert Matthew Ireland

Born June 27, 1988 in

Lawrence, MA

**PROFESSIONAL PREPARATION**

Ph.D. in Materials Science and Engineering, Johns Hopkins University (May 2016)

B.S. in Materials Science and Engineering, University of California, Davis (June 2011)

B.S. in Mechanical Engineering, University of California, Davis (June 2011)

**APPOINTMENTS**

2016-2017 Washington Innovation Fellow, Clean Energy Institute, University of Washington, Seattle

2011-2016 Graduate Research Assistant, Organic Electronics Lab, JHU, Dr. Howard Katz

2009-2011 Research Assistant, Nano-Engineering Smart Structures Technology Lab, UCD, Dr. Ken Loh

2009-2011 Processing Engineer, Center for Nano-MicroManufacturing, UCD, Dr. Frank Yaghmaie

2009-2011 Research Assistant, Advanced Composite Research Lab, UCD, Dr. Valeria La Saponara

Summer‘09 Research Experience for Undergraduates through DOE, Iowa State Univ., Dr. Zhiqun Lin

2008-2009 Lab Assistant, Land Air and Water Resources, UCD, Dr. James Richards

2007-2008 Research Assistant, Materials Processing/Characterization Lab, UCD, Dr. Joanna R. Groza

**TEACHING**

2014-2015 Alumnus, Preparing Future Faculty Teaching Academy, JHU

May 2015 Alumnus, Summer Teaching Institute, Preparing Future Faculty program, JHU

Fall 2014 Faculty, *Materials for Energy*, undergrad course, HEART program, JHU, Dr. Scheinerman

Fall 2014 Alumnus, *Implementing Small-Group Learning in STEM*, CIRTL Network online course

Spring 2014 Teaching Assistant, *Materials Science Lab II*, JHU, Dr. Wilson

Fall 2013 Teaching Assistant, *Introduction to Materials Chemistry*, JHU, Dr. McQuiggen

Spring 2013 Teaching Assistant, *Introduction to Ceramics*, JHU, Dr. McQuiggen

**OUTREACH**

Summer ‘15 High School Student Mentor, Toinetta Jones, JHU, Dr. Katz

Summer ‘15 High School Student Mentor, Derek Xiao, JHU, Dr. Katz

2014-2015 Undergraduate Student Mentor, Abraham Tan, Senior Design, JHU, Dr. Wilson & Dr. Katz

2014-2015 Elementary School Mentor, Arlington Elementary, NSF SABES program, Dr. Falk

Summer ‘13 High School Student Mentor, Toinetta Jones, NSF WISE program, JHU, Dr. Katz

2013-2014 Elementary School Mentor, John Ruhrah Elementary, NSF SABES program, Dr. Falk

2012-2013 Undergraduate Student Mentor, Stephen Lee, Senior Design, JHU, Dr. Wilson & Dr. Katz

Summer ‘11 High School Student Mentor, Carol Wu, NSF WISE program, JHU, Dr. Katz

**SERVICE COMMITTEES &AFFILIATIONS**

2012- 2016 Reviewer, Journal of Mechanics Engineering and Automation, Editor Xenia Chen

2013- 2016 Technical Editor, Enago-Freelancer, Crimson Interactive Pvt. Ltd.

2011- 2015 Part-time Consultant, Global Prescouter Scholars, Justin Duke

2012- 2014 Safety Chair, Graduate Representative Organization at JHU

2008-2011 Student Representative, Undergraduate Research Conf. Committee, UC D., Tammy Hoyer

**AWARDS & DISTINCTIONS**

Feb. 2016 Fellowship, *Innovation Fellow* at Clean Energy Institute, University of Washington, Seattle

Nov. 2015 Finalist, *Graduate Student Award (silver)*, Materials Research Society Conference

Sep. 2014 Seed Grant, *Propagating Clean Air Plants*, Earth Guardians “Protect Our Future” Campaign

Aug. 2014 Grand Prize in Innovation, *ReLeaf Organization*, UIC Institute on Sustainability and Energy

March 2011 Academic Scholarship, Johns Hopkins University Whiting School of Engineering

Feb. 2011 Leadership Grant, liaison of STEM research opportunities, UC Davis Cross-Cultural Center

Oct. 2010 President’s Undergraduate Fellowship, *Upcycling Plastic Bags*, UC Davis Research Center

Aug. 2009 Alumnus, Entrepreneurship Academy, UC Davis Graduate School of Business

April 2009 Community Choice Award, University of California at Davis Recycled Art Fair

**JOURNAL PUBLICATIONS**

1. X. Zhao, D. Madan, J. Zhou, **R. M. Ireland**, O. Alley, A. Bragg, and H. E. Katz , "Main-chain Electron-deficient and Bromide-dopable Ring-Linked Napthalenetetracarcboxylic Diimide Polymers as unipolar Electron-carrying Transistor and Thermoelectric Semiconductors," (submitted 2016).

2. **R. M. Ireland**, H. E. Katz , "Concentration and Orientation Optimization of Polymer Thermoelectric Composites Containing *In Situ* Growth of Weakly Doping Secondary Phase Particles," (submitted 2016).

3. **R. M. Ireland**, H. E. Katz , "Electrostatic-Gating of Thermoelectric Polymer Composites using Corona Charged Storage Layers," (submitted 2016).

4. **R. M. Ireland**, L. Wu, N. P. Armitage, H. E. Katz , "Tuning and Stabilizing Topological Insulator $Bi_2Se_3$ in Intrinsic Regime By Electrostatic-Gating using Corona Charged Storage Layers," (submitted 2016).

5. L. Wu, **R. M. Ireland**, M. Salehi, B. Cheng, S. Oh, H. E. Katz, N. P. Armitage, "Tuning and Stabilizing Topological Insulator $Bi_2Se_3$ in Intrinsic Regime By Charge Transfer Doping," (submitted 2016).

6. **R. M. Ireland**, Yu Liu, Xin Guo, Yu-Ting Cheng, Srinivas Kola, Wei Wang, Ronggui Yang, Michael L. Falk, Toinetta Jones, and Howard E. Katz, "ZT > 0.1 Electron-Carrying Polymer Thermoelectric Composites with *In-situ* $SnCl_2$ Microstructure Growth," *Advanced Science*, 2015.

7. **R. M. Ireland**, Y. Liu, J. Spalenka, S. Jaiswal, K. Fukumitsu, S. Oishi, H. Saito, M. Ryosuke, P. Evans, and H. E. Katz, "Device Isolation in Hybrid Field-effect Transistors by Semiconductor Micropatterning using Picosecond Lasers," *Physical Review Applied*, 2, 044006, 2014.

8. S. Kola, K. Joo, **R. M. Ireland**, M.L. Yeh, K. Smith, W. Guo, H. E. Katz, "Pyromellitic Diimide – Ethynylene Based Homopolymer Film as an N-Channel Organic Field-Effect Transistor Semiconductor," *ACS Macro Letters*, 2, 664-669, 2013.

9. J. F. Martínez Hardigree, T. J. Dawidczyk, **R. M. Ireland**, G. L. Johns, B.J. Jung, M. Nyman, R. Osterbacka, N. Marković, and H. E. Katz, "Reducing Leakage Currents in Organic Field-effect Transistors Using Molecular Dipole Monolayers," *ACS Applied Materials and Interfaces*, 5, 7025-7032, 2013.

10. J.Sinha & **R. M. Ireland** (co-first author), S. Lee, and H. E. Katz, "Synergistic Thermoelectric Power Factor Increase in Films Incorporating Tellurium and Thiophene-Based Semiconductors," *MRS Communications*, 3, 97-100, 2013.

11. **R. M. Ireland**, T. J. Dawidczyk, P. Cottingham, T. McQueen, G. Johns, N. Markovic, L. Zhang, P. Gopalan, and H. E. Katz, "Effects of Pulsing and Interfacial Potentials on Tellurium-Organic Heterostructured Films," *ACS Applied Materials and Interfaces*, 5, 1604-1611, 2012.

12. **R. M. Ireland**, L. Zhang, P. Gopalan, and Howard E. Katz, "Tellurium Thin Films in Hybrid Organic Electronics: Morphology and Mobility," *Advanced Materials*, 25, 4358-4364, 2012.

13. **R. M. Ireland**, L. Arronche, V. La Saponara, "Electrochemical Investigation of Galvanic Corrosion between Aluminum 7075 and Glass Fiber/Epoxy Composites Modified with Carbon Nanotubes," *Composites Part B*, 43, 183-194, 2011.

14. D. Ryu, **R. M. Ireland**, M. Karimzada, A. Gusman, F. Yaghmaie, K. J. Loh, "*In-Situ* Reduction of Gold Nanoparticles in PDMS Matrices and Applications for Large Strain Sensing," *Smart Structures and Systems*, 8, 471-486, 2011.

**CONFERENCE PUBLICATIONS**

1. **R. M. Ireland**, L. Arronche, V. La Saponara, "Electrochemical investigation of galvanic corrosion between aluminum 7075 and multiscale glass fiber/epoxy composites," Proceedings of the XII Pan American Congress of Applied Mechanics, Port of Spain, Trinidad, 2012.

2. **R. M. Ireland**, D. Ryu, M. Karimzada, K. J. Loh, A. Gusman, and F. Yaghmaie, "Multifunctional Strain and Chemical Sensing using Gold Nanoparticle-based Polymer Composites," Proceedings of the International Conference on Smart Structures and Systems, Seoul, South Korea, 2011.

**CONFERNECE PRESENTATIONS – ORAL**

1. **R. M. Ireland** and H. E. Katz, "Demonstration of weak solid doping concept for simultaneous conductivity and seebeck coefficient increase in p-type polymer composites," *Materials Research Society Spring Meeting*, Boston, November 2015.

2. **R. M. Ireland** and H. E. Katz, "Thermoelectric behavior of n-channel conducting polymers," *Materials Research Society Spring Meeting*, San Francisco, April 2014.

3. **R. M. Ireland**, Y. Liu, J. Spalenka, S. Jaiswal, K. Fukumitsu, S. Oishi, H. Saito, M. Ryosuke, P. Evans, and H. E. Katz, "Micro-processing of hybrid field-effect transistor arrays using picosecond lasers," *American Physical Society Spring Meeting*, Denver, March 2014.

4. **R. M. Ireland**, Thomas J. Dawidczyk, Patrick Cottingham, Tyrel McQueen, Gary Johns, Nina Markovic, Lushuai Zhang, Padma Gopalan, and Howard E. Katz, "Tellurium thin-films in hybrid organic electronics, *American Physical Society Spring Meeting*," Baltimore, March 2013.

5. **R. M. Ireland** and V. La Saponara, "Galvanic corrosion between aluminum 7075 and glass fiber/epoxy modified with carbon nanotubes," *National Conference of Undergraduate Research*, Ithaca College, May 2011.

6. **R. M. Ireland**, D. Ryu, M. Karimzada, A. Gusman, F. Yaghmaie, and K. J. Loh, "Synthesis of organometallic polymer composites for optical sensing," *21st Annual Undergraduate Research Conference*, UC Davis, April 2010.

7. **R. M. Ireland** and J. R. Groza, "Dynamic recrystallization of alpha iron solid solutions," *19th Annual Undergraduate Research Conference*, UC Davis, April 2008.

**CONFERNECE PRESENTATIONS – POSTER**

1. **R. M. Ireland** and H. E. Katz, "High-Throughput Strategy for Concentration and Orientation Optimization of Polymer Thermoelectric Composites Containing In Situ Growth of Secondary Phase Particles," *Materials Research Society Spring Meeting*, Boston, scheduled November 2015.

2. **R. M. Ireland** and V. La Saponara, "Non-destructive health monitoring via multiscale fiber-reinforced composites," *22nd Annual Undergraduate Research Conference*, UC Davis, April 2011.

3. **R. M. Ireland** and Z. Lin, "Dye-sensitized solar cell thin films utilizing $TiO_2$ nanotube arrays," *Department of Energy SULI program*, Ames Research Laboratory, July 2009.

**BOOK CHAPTER**

1. **R. M. Ireland**, and H. E. Katz (2015). "Thermoelectric Polymer-Inorganic Composites." In H. E. Katz & T. O. Poehler (Eds.), *Innovative Thermoelectric Materials* (Ch. 6). World Scientific.